A clear view on Parkinson's disease : 7T MRI investigation of the basal ganglia and development of patient-specific deep brain stimulation

Document status and date:
Published: 17/11/2016

Document Version:
Publisher's PDF, also known as Version of Record (includes final page, issue and volume numbers)

Please check the document version of this publication:

• A submitted manuscript is the version of the article upon submission and before peer-review. There can be important differences between the submitted version and the official published version of record. People interested in the research are advised to contact the author for the final version of the publication, or visit the DOI to the publisher's website.
• The final author version and the galley proof are versions of the publication after peer review.
• The final published version features the final layout of the paper including the volume, issue and page numbers.

Link to publication

A clear view on Parkinson's disease

7T MRI investigation of the
basal ganglia and development of
patient-specific deep brain stimulation

Birgit R. Plantinga

A clear view on Parkinson's disease

7T MRI investigation of the basal ganglia and
development of patient-specific deep brain stimulation

A clear view on Parkinson's disease

7T MRI investigation of the basal ganglia and
development of patient-specific deep brain stimulation

PROEFSCHRIFT

ter verkrijging van de graad van doctor aan de
Technische Universiteit Eindhoven, op gezag van de
rector magnificus prof.dr.ir. F.P.T. Baaijens,
voor een commissie aangewezen door het College
voor Promoties, in het openbaar te verdedigen op
donderdag 17 november 2016 om 14:00 uur

door

Birgit Renske Plantinga

geboren te Eindhoven

Dit proefschrift is goedgekeurd door de promotoren en de samenstelling van de promotiecommissie is als volgt:

voorzitter: prof.dr. P.A.J. Hilbers
1^e promotor: prof.dr.ir. B.M. ter Haar Romenij
2^e promotor: prof.dr. Y. Temel (Universiteit Maastricht)
leden: prof.dr. J.P.W. Pluim
                 prof.dr.ir. M. Breeuwer
                 prof.dr. N. Harel (University of Minnesota)
                 prof.dr. V.E.R.M. Visser-Vandewalle (University of Cologne)
                 dr. K. Uludağ (Universiteit Maastricht)

Contents

Summary

A clear view on Parkinson's disease
7T MRI investigation of the basal ganglia and
development of patient-specific deep brain stimulation

Parkinson's disease (PD) is a neurodegenerative disease resulting in motor symptoms such as bradykinesia, tremor, and rigidity. The pathophysiological basis for these symptoms lies in the basal ganglia, a group of gray matter nuclei deep in the brain that consists of the subthalamic nucleus, substantia nigra, globus pallidus, and striatum. Although PD disrupts the whole network of the basal ganglia, the degeneration of dopamine producing cells in the substantia nigra pars compacta is one of its most characteristic features. In addition to treatment with dopaminergic medication, deep brain stimulation is a widely applied treatment option. This involves the permanent electrical stimulation of the subthalamic nuclei through stereotactically placed electrodes. One of the challenges in doing so is to specifically stimulate the motor part of the subthalamic nucleus. This is thought to optimize the clinical outcome and reduce side-effects. However, the currently used 1.5 T or 3 T preoperative clinical MRI scans are not sufficient to show the motor part of the subthalamic nucleus.

Ultra-high field MRI (7 T and higher), on the other hand, is able to image the brain with higher resolution, signal-to-noise ratio, contrast-to-noise ratio, and/or a shorter scan time, compared to the clinically available 1.5 T or 3 T MR scanners. Our review of in vivo and post mortem 7 T basal ganglia studies showed that especially sequences that are sensitive to magnetic susceptibility, such as T2* and susceptibility-weighted sequences, can image the iron-rich basal ganglia with high detail at ultra-high field. Despite the limited availability of 7 T MR scanners (61 worldwide in 2014), their improved identification, delineation, and quantitative measurements of the nuclei allow for investigating both the healthy as well as the pathologically affected basal ganglia at high resolution and in humans at a new level.

The research described in this thesis focuses on the basal ganglia, their role in PD, and especially on the subthalamic nucleus. Quantitative MRI was used to demonstrate that the absolute T1 values of the caudate nucleus, subthalamic nucleus, and substantia nigra, and the T2* value of the substantia nigra, were decreased in PD patients compared to healthy control subjects. Additionally the caudate nucleus, substantia nigra, and internal globus pallidus displayed an altered mean diffusivity. This indicates altered iron and macromolecular concentrations and altered microstructure in these nuclei. Being able to assess these changes in vivo may allow for monitoring the disease progression of each patient and optimizing the individual treatment accordingly, through medication or surgery. Additionally it may improve our understanding of the underlying disease pathology by relating the variable symptoms to specific pathological changes as measured with quantitative 7 T MRI.

In addition, diffusion-weighted MRI was employed to reconstruct the connections of the subthalamic nucleus with the motor, associative, and limbic cortices in 17 PD patients, through a fruitful collaboration with the Center for Magnetic Resonance Research (CMRR) of the University of Minnesota. This allowed for the subdivision of the subthalamic nucleus into a posterolateral motor zone, an overlapping central associative zone, and an anteromedial limbic zone. These patient-specific maps may potentially facilitate for deep brain stimulation surgeries to be performed more accurately and tailored to each individual's anatomy.

Finally, the detailed connections of the human basal ganglia have been mapped using ultra-high resolution 7 T post mortem tractography, enabled through long scan times (42 hours). In addition to the currently established connections of the basal ganglia network, this also allowed for constructing currently unknown connections. This indicated among other things a more prominent role for the substantia nigra pars compacta within the network of the basal ganglia, which challenges the current concepts.

In conclusion, the described studies provide new insights into the basal ganglia and their role in PD. They show that 7 T imaging and analysis may aid in a more accurate planning of deep brain stimulation surgeries and improve the treatment of PD.

Samenvatting

De ziekte van Parkinson is een neurodegeneratieve ziekte die gepaard gaat met motorische symptomen zoals bradykinesie, tremor en stijfheid. De pathofysiologische basis voor deze symptomen bevindt zich in de de basale ganglia, een groep grijze stof kernen diep in het brein die bestaat uit de nucleus subthalamicus, substantia nigra, globus pallidus en het striatum. Hoewel de ziekte van Parkinson het hele netwerk van de basale ganglia verstoort, is de degeneratie van dopamineproducerende cellen in de substantia nigra pars compacta het meest karakteristiek. Naast de behandeling door middel van dopaminerge medicatie, is diepe hersenstimulatie een veel toegepaste behandelingsoptie. Hierbij wordt de nucleus subthalamicus permanent elektrisch gestimuleerd door stereotactisch geplaatste elektrodes. Een van de uitdagingen hierbij is om specifiek het motorische deel van de nucleus subthalamicus te stimuleren. De verwachting is dat de uitkomst van de operatie hierdoor optimaal wordt en bijwerkingen worden beperkt. Echter, de huidige 1.5 T en 3 T preoperatieve klinische MRI-scans schieten tekort bij het visualiseren van het motorische deel van de nucleus subthalamicus.

Ultra-hoog veld MRI (7 T en hoger) daarentegen, biedt de mogelijkheid om het brein ten opzichte van de klinisch beschikbare 1.5 T of 3 T MRI-scanners met een hogere resolutie, signaal-ruisverhouding, contrast-ruisverhouding en/of een kortere scantijd af te beelden. Onze review van in vivo en post mortem 7 T basale ganglia studies liet zien dat met name sequenties die gevoelig zijn voor magnetische susceptibiliteit, zoals T2*- en susceptibiliteitgewogen sequenties, de ijzerrijke basale ganglia in detail kunnen visualiseren op ultra-hoog veld. Ondanks de beperkte beschikbaarheid van 7 T MRI scanners (61 wereldwijd in 2014) maken de verbeterde identificatie, omlijning en quantitatieve metingen van de kernen het mogelijk om zowel de gezonde als de pathologisch aangetaste basale ganglia op hoge resolutie en in mensen op een nieuw niveau te onderzoeken.

Het onderzoek beschreven in dit proefschrift richt zich op de basale ganglia, de rol hiervan in de ziekte van Parkinson en in het bijzonder op de nucleus subthalamicus. Met behulp van quantitatieve MRI is aangetoond dat de

absolute T1-waarden van de nucleus caudatus, nucleus subthalamicus en substantia nigra en de T2*-waarde van de substantia nigra, van parkinsonpatiënten lager zijn dan van gezonde controles. Daarnaast was ook de mean diffusivity van de nucleus caudates, substantia nigra en globus pallidus internus veranderd. Dit duidt ook op veranderde ijzer- en macromolecuulconcentraties en een veranderde microstructuur in deze kernen. Het in vivo kunnen meten van deze veranderingen kan het monitoren van de ziektevoortgang van elke patiënt en het optimaliseren van de individuele behandeling, zowel door medicatie als door operaties, mogelijk bevorderen. Bovendien kan het ons begrip van de onderliggende pathologie verbeteren, door het koppelen van de gevarieerde symptomen aan de specifieke pathologische veranderingen zoals gemeten met 7 T quantitatieve MRI.

Daarnaast zijn, via een vruchtbare samenwerking met het Center for Magnetic Resonance Research (CMRR) van de University of Minnesota, de verbindingen van de nucleus subthalamicus met de motorische, associatieve en limbische cortices in 17 parkinsonpatiënten in kaart gebracht met behulp van diffusiegewogen MRI. Hieruit konden individuele onderverdelingen van de nucleus subthalamicus worden gegenereerd, met een posterolaterale motorische zone, een overlappende, centrale associatieve zone en een anteromediale limbische zone. Met deze patiëntspecifieke maps kunnen diepe hersenstimulatieoperaties in potentie nauwkeuriger en toegespits op ieder individu's anatomie worden uitgevoerd.

Ten slotte zijn de verbindingen van de menselijke basale ganglia in detail in kaart gebracht met behulp van ultra-hoog resolutie post mortem 7 T tractografie met een lange scantijd (42 uur). Hiermee konden naast de algemeen vastgestelde verbindingen van het basale ganglia netwerk ook onbekende verbindingen worden gereconstrueerd. Dit wees onder andere op een prominentere rol van de substantia nigra pars compacta binnen het netwerk van de basale ganglia, waardoor de huidige concepten worden uitgedaagd.

In conclusie geven de beschreven studies nieuwe inzichten in de basale ganglia en hun rol in de ziekte van Parkinson. Ze laten zien dat 7 T beeldvorming en analyse kunnen helpen om de behandeling van de ziekte van Parkinson door middel van diepe hersenstimulatie nauwkeuriger uit te voeren.

CHAPTER 1

GENERAL INTRODUCTION

1.1   Preface

Despite many efforts and years of extensive research, the brain is probably the last organ of the human body that still remains largely mysterious. Its capability of storing memories, steering emotions, learning tasks, and forming thoughts, to name a few, is still barely understood.

Nevertheless, over the last decades many efforts have been put into trying to unravel this organ. Individual brain cells can be cultured and observed in vitro and histological assessments of brain slices can be performed ex vivo, often combined with invasive in vivo experiments. Additionally, technological advances have produced a large range of non-invasive investigational methods especially suitable for studies in humans. Powerful computers facilitate increasingly accurate models of the brain[143]. Additionally, transcranial magnetic stimulation allows for the temporary modulation of brain activity in specified areas[125]. Furthermore, new therapies are emerging that guide patients based on direct feedback of their brain's activity[201]. Finally, mathematical and imaging techniques allow for large and small-scale mapping of the brain's complex connections[211].

The latter two of these are enabled by major advances made in the field of medical imaging. This progress has also had a great influence on the diagnosis, monitoring, treatment, and research of many diseases. Especially magnetic resonance imaging (MRI), is suitable for non-invasive imaging of different tissue types. Furthermore, its ability to generate different kinds of contrasts makes it especially suitable for imaging different brain structures such as the basal ganglia and gray and white matter. Additionally, advanced MRI techniques also allow for visualizing brain activity and reconstructing white matter pathways.

In this work, both the clinical need for investigating the brain as well as the latest advances in the field of MRI are brought together. Specifically, ultra-high magnetic field MRI (7 T) is used to investigate the human basal ganglia and Parkinson's disease.

1.2   Aim

The aim of my research was to investigate the potential of ultra-high field MRI for understanding the detailed structure and function of the human brain, and more specifically the basal ganglia. This group of nuclei is important for motion and emotion, and relevant for many diseases including Parkinson's disease. They are involved in the pathology of the disease and are a target for deep brain stimulation, one of the treatment options for Parkinson's disease.

The research described in this thesis focuses on visualization of the basal ganglia in Parkinson's disease patients and healthy subjects, reconstruction of the basal ganglia's connections, and potential improvements to deep brain stimulation surgery. It aims to answer the question: How can ultra-high field MRI contribute to improved understanding of the basal ganglia and their role in Parkinson's disease?

1.3   Outline of this thesis

The outline of this thesis is as follows. First, the basal ganglia, Parkinson's disease, deep brain stimulation, and MRI will be introduced (Chapter 2 and Chapter 3). This will be followed by an overview of the possibilities for visualizing the targets for deep brain stimulation with the aid of ultra-high field MRI (Chapter 4). This also allows for detailed quantitative mapping of the relaxation times and diffusion parameters. This is presented in a study into the pathological changes in the basal ganglia of Parkinson's disease patients that revealed altered T1, T2* and diffusion parameters (Chapter 5). One of these basal ganglia nuclei is the subthalamic nucleus. Its motor territory is a target for deep brain stimulation for Parkinson's disease. The identification of these motor and non-motor territories of the subthalamic nucleus of Parkinson's disease patients was investigated in a clinical study using ultra-high field MRI tractography (Chapter 6). Additionally, using the possibility of long scan times, the detailed connections of the subthalamic nucleus, substantia nigra, and globus pallidus were also investigated using post mortem high resolution tractography, resulting in both commonly established as well as novel connections (Chapter 7). Finally, the overall findings are combined and discussed in the last chapter (Chapter 8).

CHAPTER 2

CLINICAL BACKGROUND

2.1 Parkinson's disease

Parkinson's disease (PD) is a neurodegenerative disorder with progressively worsening symptoms, of which the motor symptoms are the most characteristic. It was named after the British apothecary James Parkinson, who described the disease, then known as shaking palsy, in 1817[176]. The exact display of symptoms, including rest tremor, slowness of movement (bradykinesia), muscular rigidity, postural imbalance, and gait impairment can be different from patient to patient. They can also involve non-motor features such as cognitive, psychiatric, olfactory, and sleep problems, which may well precede the motor symptoms[104].

The disease is typically diagnosed in patients of 50 years or older, although the actual onset may occur well before the symptoms appear[33]. The clinical diagnosis, based on the disease symptoms, is not always straightforward to make, as symptoms overlap with those of other diseases such as essential tremor, multiple system atrophy, and progressive supranuclear palsy[182]. Recent guidelines for the diagnosis of PD consider a range of inclusion criteria that point towards PD and exclusion signs that indicate other parkinsonian conditions[182]. Core criteria are bradykinesia combined with rest tremor, rigidity, or both (definition of parkinsonism). The presence of additional symptoms, such as good levodopa (drug) response and olfactory loss, or absence of other symptoms may guide a more accurate diagnosis. Several scales exist to quantify and monitor the severity of the disease in individual patients. One of them is the Unified Parkinson's Disease Rating Scale (UPDRS), which consist of six parts, addressing varying aspects including psychological, activities of daily life, and motor evaluations[79].

2.2 Basal ganglia

Although it is yet largely unclear why patients develop PD, the etiology is well described. PD is a disease of the basal ganglia, a group of gray matter structures situated deeply in the brain (see Figure 2.1).

They are symmetrical across hemispheres and consist of the:

- Putamen and caudate nucleus; together called striatum
- Internal and external globus pallidus
- Substantia nigra, consisting of a pars compacta and pars reticulata
- Subthalamic nucleus
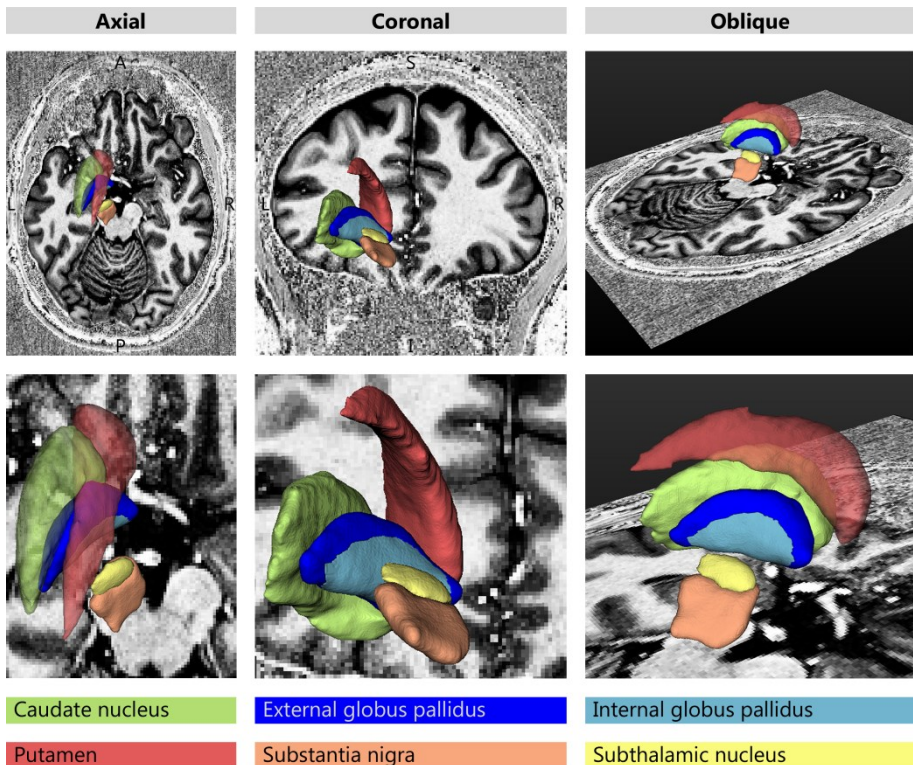
Figure 2.1: Basal ganglia of the left hemisphere.
The visualized structures were manually segmented on a T1-weighted 7 T MR image and visualized with vIST/e (http://bmia.bmt.tue.nl/software/viste/).

In the classical model[6,159], the cortex sends information to the basal ganglia, where it is processed and sent back to the cortex via the thalamus (see Figure 2.2). By doing so, the basal ganglia can modulate signals involved in different functions, such as cognitive, limbic, and motor processes[151,204].

Three pathways have been described within the basal ganglia (Figure 2.2).

The *direct pathway* acts as a positive feedback loop. In this pathway the cortex sends excitatory signals to the putamen, which indirectly inhibits the internal globus pallidus (GPi) and substantia nigra pars reticulata (SNr) complex. These two structures then disinhibit the thalamus, thereby effectively reinforcing the signals directed back to the cortex.

The *indirect pathway*, on the other hand, functions as a negative feedback loop. In this circuit, the signals from the putamen are redirected to inhibit the external globus pallidus (GPe). These signals then disinhibit the subthalamic nucleus (STN) and the GPi/SNr, which then leads to inhibition of the thalamus and its projections to the cortex.

Finally in the *hyperdirect pathway*, the putamen is bypassed and the signals from the cortex are directly projected onto the STN to excite the GPi and SNr[159], thereby again inhibiting the thalamus and cortex.
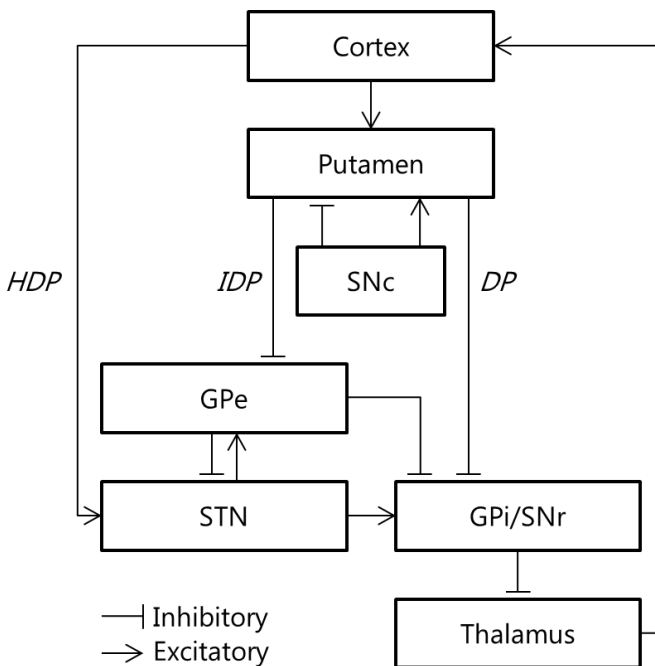
Figure 2.2: The direct (DP), indirect (IDP) and hyperdirect (HDP) pathways of the basal ganglia. GPe = External globus pallidus. GPi = Internal globus pallidus. SNc = Substantia nigra pars compacta. SNr = Substantia nigra pars reticulata. STN = Subthalamic nucleus.

Generally understood, the direct pathway activates only the desired programs while the hyperdirect and indirect pathways suppress unwanted competing programs[57,159]. Through this interplay of pathways, a voluntary movement can for example be executed while other movements are suppressed.

2.3 Pathology of Parkinson's disease

Parkinson's disease is characterized by the degeneration of dopamine producing neurons in the substantia nigra pars compacta and the loss of dopamine in the striatum. As a neurotransmitter, dopamine transfers signals from one neuron to the other. Although the classical explanation does not fully account for all basic clinical findings in PD patients, it does explain the typical hypokinetic features of PD. According to this model, PD causes increased activity along the inhibitory striatopallidal indirect pathway, which results in a decreased neuronal discharge in the GPe, which again results in a disinhibition of the STN, GPi, and SNr, effectively leading to an increase in the inhibition of the thalamus[57,222]. The resultant reduced cortical activation in its turn is suspected to cause the slowing of movement in patients. Another observation is the recording of rhythmic bursting signals in the STNs of monkeys with PD[28]. However, its link with the symptoms of PD is not completely understood.

2.4 Deep brain stimulation

Patients with PD are usually treated with drugs that replete the loss of dopamine in the brain or stimulate dopamine receptors. These drugs treat the symptoms well in the early stages of the disease, but response becomes poorer as the disease progresses. Additionally, drug induced side-effects, such as nausea and oedema at the short-term use, and dyskinesia and motor fluctuations after long-term use, may occur[104].

Alternatively, deep brain stimulation (DBS) is a well established treatment for PD. It was first performed in three patients in 1993[24,130], and has since grown to become a widely performed therapy. The procedure involves the bilateral surgical implantation of a permanent electrode into the STN. This electrode is then connected via a wire under the skin to a subcutaneous

stimulator and battery that sends high frequency (typically around 130 Hz[24]) electrical pulses with a typical voltage of 2.0-3.5 V[24] to the desired contact at the end of the lead deep in the brain. The implanted leads often have four or five contacts that can be switched on or off to manipulate the volume and location of the stimulated area after surgery.

2.4.1   Targeting the subthalamic nucleus

The aim of the DBS surgery is to place the electrode in the motor part of the STN. The targeting process consists of three methods to do so:

1.   Preoperative imaging and planning

The subthalamic nucleus can be distinguished as a dark structure on T2 and T2*-weighted MRI scans[36,112]. Prior to surgery, patients undergo a 1.5 T or 3 T MRI scan on which the neurosurgeon marks its target directly within the STN. Additionally, the patient undergoes an X-ray computed tomography (CT) scan with a stereotactic frame attached to his head. This image is then merged with the MR image in order to translate the target location to real life stereotactic coordinates used during surgery. However, imaging the STN with 1.5 T or 3 T MRI scanners can be limited and may result in unsatisfactory imaging contrast or signal-to-noise ratios. Alternatively neurosurgeons may choose indirect targeting methods, based on the distance from the midcommissural point or on atlases overlayed on the MR image. However, these methods are undesired in itself, because they ignore the known variability between patients in size and location of the STN[14,186].

2.   Intraoperative micro-electrode recording

During the surgery, which is often performed under local anesthesia, a small burr hole in the skull provides access for implantation of the lead. Before the chronic electrode is implanted, electrophysiological recordings of the neuronal activity with micro-electrodes are performed to establish the preferred depth of the active contact. The STN expresses typical firing patterns such as asymmetrical high frequency spikes, bursting activity, and responses to passive movements, which differ from its inferiorly neighboring SNr that expresses more regular activity and is usually unresponsive[24]. Several parallel tracks may be tested to also explore the space in directions perpendicular to the lead.

3. Intraoperative patient testing

In addition to the micro-electrode recording, the clinical response to stimulation with the micro-electrodes is also tested during surgery. This is usually performed on the electrode trajectory with the longest STN activity[119]. Decrease of symptoms, such as rigidity of the wrist, hypokinesia, and tremor, and absence of side-effects are assessed by a neurologist, while the depth of the stimulating electrode is increased step-by-step.

2.4.2 The DBS procedure

The DBS surgery itself requires intensive patient screening, planning, and postoperative care.

As a first step, potential candidates for DBS are hospitalized for a few days for a team of anesthesiologists, ergotherapists, neuropsychologists, neurosurgeons, psychiatrists, physiotherapists, and specialized nurses to evaluate whether the patient is eligible for DBS[119]. Eligible patients usually have medication refractory response fluctuations, dyskinesias, or tremor[168].

Prior to the surgery, the patient will again be hospitalized. After a gradual reduction of antiparkinsonian medication in the week before, the medication is stopped on the evening before surgery and the hair is shaved and washed with povidone-iodine shampoo[119]. On the morning of the surgery, the stereotactic frame is placed under local anesthesia and the stereotactic CT scan is performed to fuse with the previous MR images and the estimated target. The surgery itself lasts a few hours and is performed by a team of psychologists, specialized nurses, neurosurgeons, neurologists, neurophysiologists, and anesthesiologists. A small burr hole is made, through which the micro-electrodes are descended to perform the micro-electrode recording and intraoperative patient testing. Finally, when the final electrode location is decided on, the micro-electrode is replaced by the permanent lead.

The day after the surgery, an MRI scan is performed to verify the electrode position and evaluate hemorrhages. The internal pulse generator can be implanted in the abdominal region or infraclavicularly, either immediately after surgery or a few days later. In the days following surgery, the patient is evaluated to assess the degree of therapeutic effects and side-effects, to

perform wound care and remove sutures, and to program the stimulation settings, such as choice of active contacts, polarity of the stimulation, and voltage. Fine-tuning of these settings and reduction of the medication is performed during outpatient visits in the weeks and months after surgery and every year routinely.

2.4.3   Outcome of DBS surgery

On average, DBS of the STN improves the activities of daily living (UPDRS II) with 50 % and motor scores (UPDRS III) with 52 %, when compared to an off-medication baseline[118]. Furthermore it allows for a reduction in the levodopa equivalent dose of the taken medication of 56 %[118]. This combination of decreased levodopa intake and DBS was demonstrated to improve symptoms significantly better than medication alone[61]. When compared to an on-medication baseline, the activities of daily living such as speech, dressing, and walking (UPDRS II) decreased with 16 % and the motor symptoms (UPDRS III) decreased with 23 %[61]. However, it should be noted that there is a great variability of the outcomes between patients[118].

Despite these good results and growing experience, the mechanism of action of DBS is still not completely understood. Its effect is similar to the ablation of the stimulated structure[25], with the significant advantage of DBS being reversible if the effect is undesired. This lead to the theory that DBS inhibits the STN through a range of hypothesized mechanisms including a) replacement of the pathological bursting signal of the STN by a periodic information free signal[84,148], b) stimulation of pre-synaptic inhibitory terminals[88], and c) continuous inactivation of voltage dependent ion channels (depolarization block)[88,133]. However, other studies show that the activity of the output structures of the STN is actually increased by DBS[90,95], indicating that the actual mechanism of action constitutes of a more complex interplay of the observed effects.

Despite its beneficial therapeutic effects, DBS has also been associated with complications and side-effects. Complications include hemorrhages, of which intracranial hemorrhages are most severe, infections, often at the site of the implanted battery, and malfunctioning of the device, such as lead breakage and premature battery consumption[24]. Reported rates on complications vary greatly between sites with intracranial hemorrhages occurring in 1 to 4 % of cases[24,54,118,207] and infections rates varying from 1 %

to 15 %[54,118,166,203]. Stimulation induced adverse effects include speech problems, such as dysarthria and hypophonia, visual flashes, cognitive changes, depression, and (hypo)mania[24,205]. These side-effects are often related to a suboptimal location of the active contact and can usually be managed by adjusting the stimulation parameters, sometimes at the expense of the therapeutic effect. Since the basal ganglia are not only involved in motor processes, but also in associative and limbic circuits, this demonstrates the importance of accurate electrode placement and consequently reliable planning of the surgery.

CHAPTER 3

TECHNICAL BACKGROUND

3.1   General mechanism of MRI

Magnetic resonance imaging (MRI) is a non-invasive technique for imaging the inside of the human body. In contrast to for example X-ray computed tomography (CT), it does not use potentially harmful X-rays, but it makes use of the nuclear magnetic resonance properties of atoms, most often the hydrogen (H) atom.

An MRI scanner (Figure 3.1) constantly maintains a net magnetic field, called the B0 field, along the direction of the bore, even when the scanner is not being used. For clinical scanners the strength of this magnetic field is usually 1.5 T or 3 T. When a person lies in the MRI scanner, this magnetic field will cause a net equilibrium magnetization of the tissue along the direction of the bore. If radio frequency pulses (the B1 field) are then applied, the magnitude and direction of this net magnetization can be altered. The characteristics of how this net magnetization then returns to equilibrium are measured with MRI.

Figure 3.1: Ultra-high field (7 T) MRI scanner (Magnetom 7T, Siemens, Erlangen, Germany).

3.2   MRI contrast

These characteristics are described by the relaxation times, T1, T2, and T2* of the tissue. These time constants depend on the magnetic spin interaction properties of nuclei, which are influenced, among other things, by the molecular composition and organization of the tissue and the strength of B0. Sometimes, the relaxation rates R1, R2, and R2* are used, defined as 1/T1, 1/T2, and 1/T2* respectively. MRI uses the dependencies of these relaxation times on tissue properties to generate contrast within an image.

Whether and how well a certain brain structure is visible on an MR image also depends on the chosen acquisition protocol, such as spin echo (SE) and gradient echo (GE) sequences. The different sequences are described by the combination of the properties of the gradient, radio-frequency pulses, and timing parameters. Properties that are often varied are the echo time (TE), repetition time (TR), and flip angle. This can result in T1, T2, or T2*-weighted images in which the contrast is mainly caused by differences in T1, T2, or T2* values of the tissue. The variability in sequences therefore facilitates optimization of the protocol for each structure of interest individually. An overview of the important concepts of MR imaging is shown in Table 3.1.

Table 3.1: Important concepts in MR imaging.

Variable	Definition	Specific for	Relevance
T1	Spin-lattice relaxation time		
T2	Spin-spin relaxation time		
T2*	T2* relaxation time	Tissue	Influences MR signal in tissue
R1	1/T1		
R2	1/T2		
R2*	1/T2*		
TE	Echo time		
TR	Repetition time	Sequence	Determines the generated contrast
Flip angle	Flip angle		
χ	Magnetic susceptibility	Tissue	Gives extra contrast to certain substances
SNR	Signal-to-noise ratio	Image	Quantifies the quality of the image
CNR	Contrast-to-noise ratio		

3.3   Quantitative imaging

Using the right scan protocols and post processing techniques, so-called T1, T2, or T2* maps can be generated, that display the quantitative T1, T2, or T2* values of each voxel in an image respectively. Similarly, R1, R2, or R2* maps can be produced (Figure 3.2).
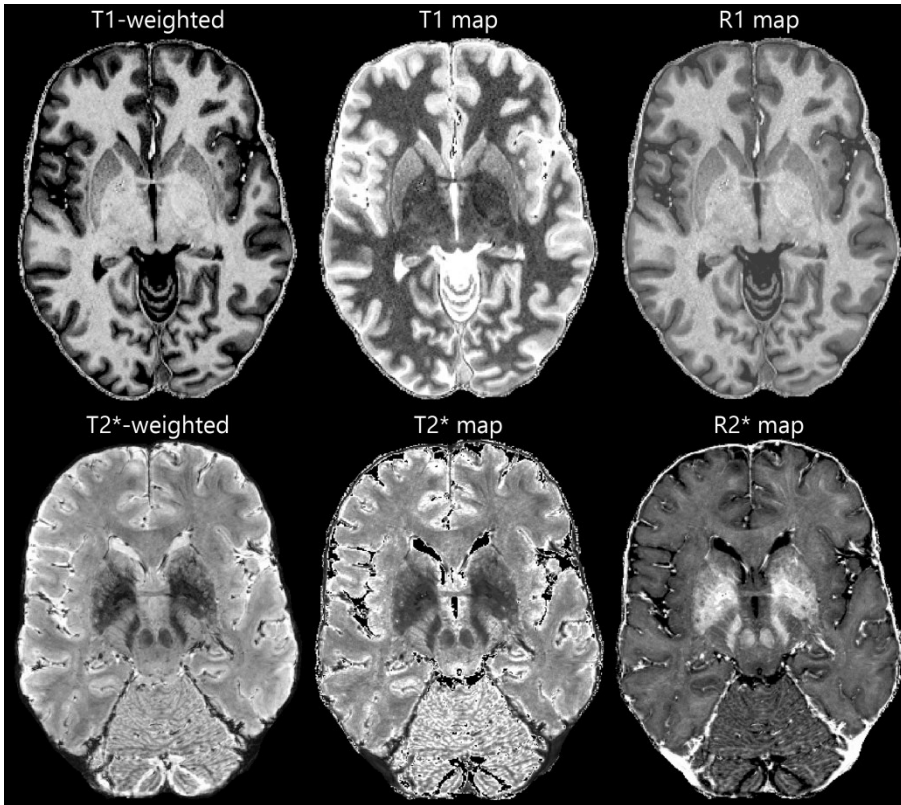
Figure 3.2: Examples of T1 and T2-weighted images, with their corresponding T1, R1, T2*, and R2* maps.*

3.4   Magnetic susceptibility

In addition to the tissue's T1, T2, and T2*-weighted images, susceptibility-weighted images can also be acquired[85]. These images are based on the principle that MR images are generally complex-valued, i.e. effectively two images are always acquired: a commonly used magnitude image that often

directly displays the anatomical structures and a phase image that is usually disregarded. The phase image however is sensitive to the so-called magnetic susceptibility (χ). This property of tissues and substances alters the local magnetic field values. Paramagnetic materials have a positive χ and strengthen the magnetic field, and diamagnetic materials have a negative χ and weaken the magnetic field. Tissues with a susceptibility that differs from their surrounding structures, such as tissues with myelin and iron-containing substances, cause local deviations in the magnetic field inside and outside of the structures. This leads to local phase differences, which can then be extracted from the original phase images. In susceptibility-weighted imaging, these phase images are combined with the magnitude images, which can result in additional contrast, which particularly enhances the brain's (micro)vessels and the small deep brain structures. Additionally the actual susceptibility values can be displayed in so-called quantitative susceptibility maps.

3.5 Functional MRI

In addition to structural imaging, functional MRI (fMRI) can provide information on localized brain activity[38]. By measuring alterations in the oxygenation of the brain's capillaries, fMRI can be used to investigate which brain areas are involved in certain tasks (task based fMRI), or which brain areas have the same activation pattern in rest (resting state fMRI). The latter can also be used to compute the functional connectivity between two or more areas.

3.6 Diffusion-weighted imaging

In addition to structural and functional MRI, diffusion-weighted imaging, which is directionally sensitive to water diffusion, provides valuable images to reconstruct the brain's neuronal fiber connections. It allows for measuring diffusion-related properties of the tissue and facilitates reconstruction of the brain's structural connections.

3.6.1   Diffusion

Diffusion, also called Brownian motion, is the random motion of, in this case water molecules, that is always present in brain tissue. When it is not obstructed by boundaries, such as in a glass of water, the amount of diffusion is equal in every direction and the diffusion pattern will be spherical. This is called isotropic diffusion. When the molecules are obstructed by, for example, axonal tracks, the water mobility will be decreased in the direction orthogonal to the cell boundaries and the diffusion pattern will be more ellipsoidal along the directions of the axons. In this case the diffusion is called anisotropic[123]. More complex diffusion patterns occur when the obstructions become more complex such as is the case for crossing, splitting, or kissing fibers. Diffusion-weighted imaging tries to deduce these diffusion patterns in order to derive the local fiber orientations.

3.6.2   Acquisition

The diffusion-weighted acquisition protocol is sensitized to water diffusion in a specific direction. The amount of water diffusion in this direction can be derived from two factors: a) the chosen scan parameters, represented by the b-value and b) the signal loss between the diffusion-weighted scan and a scan without diffusion weighting (called the b0-image). The more often this diffusion-weighted protocol is repeated with different directions, the more accurate the sampling of the diffusion pattern in each voxel becomes. Typical values for the scan settings are around 700-1000 s/mm^2 for the b-value, 30-40 imaging directions and a scan time of 5-10 minutes[211]. However, other parameter choices are well possible since they are usually optimized for the research question and practical limitations, such as available hardware and scan time.

3.6.3   Diffusion models

Practical constraints such as scan time limit the number of directions that can be measured with diffusion MRI. Mathematical models have been developed that can describe the diffusion pattern in a voxel on the basis of only a limited number of measured diffusion directions.

The simplest and most common of these is the diffusion tensor model. This model requires only six diffusion directions to be sampled (plus at least one b0-image without diffusion weighting). Often however, the number of measured directions is greater than six, to reduce the effect of noise. The diffusion tensor is a mathematical concept, consisting of six unique elements, that can describe an ellipsoid. Thus, diffusion tensor imaging (DTI) describes the diffusion pattern with an ellipsoid. This tensor has a few interesting mathematical properties. Its three eigenvectors (**v**) describe the directions of the three main orthogonal axes of the ellipsoid and the according eigenvalues (λ) describe the magnitude of these eigenvectors (Figure 3.3). The eigenvectors and eigenvalues ranked from the highest to the lowest eigenvalue are called v_1, v_2, and v_3 and λ_1, λ_2, and λ_3, respectively.
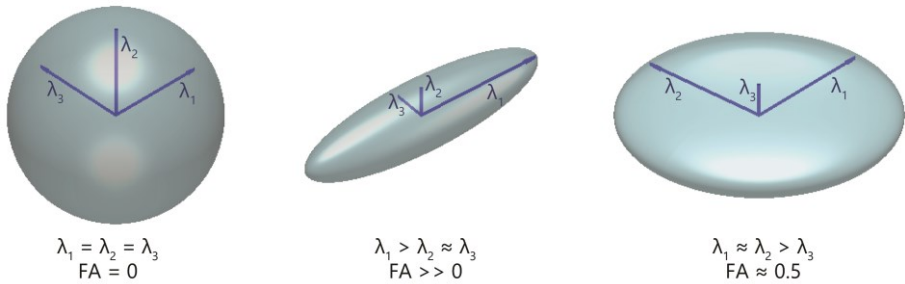
Figure 3.3: Examples of diffusion tensors with their eigenvalues (λ_1, λ_2, and λ_3) and fractional anisotropy (FA).

This allows for the definition of a few interesting image parameters. The mean diffusivity (MD), defined as:

$$MD = (\lambda_1 + \lambda_2 + \lambda_3) / 3 \qquad\qquad 3.1$$

describes the average diffusion in the three orthogonal directions defined by the eigenvalues (Figure 3.4). A high mean diffusivity, for example, indicates that the water molecules experience few obstructions, such as is the case in ventricles. However, this measure cannot infer anything about the local anisotropy of the diffusion pattern. This can be described with the fractional anisotropy (FA) (Figure 3.4), defined as:

$$FA = \sqrt{(\lambda_1\text{-}\lambda_2)^2 + (\lambda_1\text{-}\lambda_3)^2 + (\lambda_2\text{-}\lambda_3)^2} / \left(\sqrt{2(\lambda_1^2 + \lambda_2^2 + \lambda_3^2)} \right) \qquad\qquad 3.2$$

The fractional anisotropy can roughly distinguish three scenarios (see Figure 3.3):

- low anisotropy (FA is close to 0) if all three eigenvalues are similar, representing a spherical diffusion pattern. This occurs, for example, in ventricles, where water molecules have few boundaries in all directions.

- high anisotropy (FA is close to 1) if one eigenvalue is high and the other two are low, representing an elongated ellipsoid. This can, for example, be expected in unidirectional white matter paths, where the diffusion pattern follows the direction of the white matter fibers.

- intermediate anisotropy if two eigenvalues are high and one is low. This may represent diffusion in two directions, such as in the case of two crossing fiber bundles.
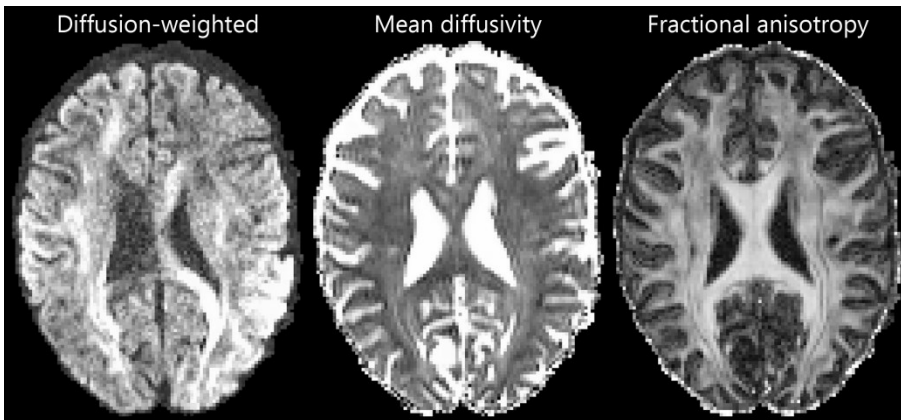
Figure 3.4: Examples of a diffusion-weighted image, which is directionally sensitized to water diffusion, and its corresponding mean diffusivity (MD) and fractional anisotropy (FA) maps.

Note that this diffusion tensor model can only describe diffusion in one orientation and does therefore not deal well with crossing or kissing fibers[208]. To solve this, alternative multi-orientation methods have been proposed. Two examples of this are the ball and stick model as implemented in FSL[22,102] and constrained spherical deconvolution (CSD)[209] as implemented in the MRtrix software package[208]. In the ball and stick model, the measured signal is predicted to be the weighted sum of the signal from an isotropic

background component (ball) and a number of anisotropic tensors (sticks). Here, each tensor represents a fiber bundle with a distinct orientation. The number of orientations in a voxel is estimated from the data in each voxel individually, so as to only estimate the number of fiber orientations that are supported by the data. The CSD method estimates in each voxel a fiber orientation density function (fiber ODF)[210] (Figure 3.5). This function expresses the fraction of fibers that are oriented along a certain orientation as a function of this orientation expressed in *spherical* coordinates. The fiber ODF is estimated from the *deconvolution* of the measured signal in each voxel and the measured signal from a single orientation fiber bundle. It is *constrained* in the sense that negative lobes, that may result from noise, are penalized. As this method can infer multiple fiber orientations, it benefits from diffusion-weighted MRI data with a high-angular resolution, which is reflected by a high number of sampled diffusion directions (approximately 45 or more). Additional benefits of this method are that it does not need any a priori information about the expected number of fiber populations within a voxel and it does not depend on an assumed model of diffusion.
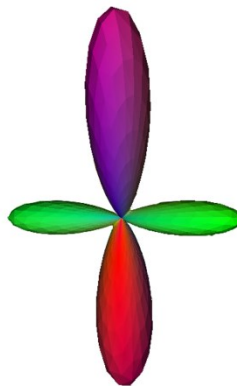
Figure 3.5: Example of a fiber orientation density function.

3.6.4   Tractography

Once the local fiber orientation in each voxel is estimated, it can be used to reconstruct the fiber paths in the brain. By following the local estimated fiber orientation, tracks can be propagated through this 3D space[18]. A 2D schematic example of this process, called fiber tracking or tractography, is shown in Figure 3.6. Given a starting point (seed) within a voxel in the brain,

a small step is made along the estimated direction of the local fiber orientation to end up at a new location in the brain. Starting from the new location, this process is repeated iteratively until some stop criterion is met, such as a sudden change in direction, low FA, or reaching the border of the brain.
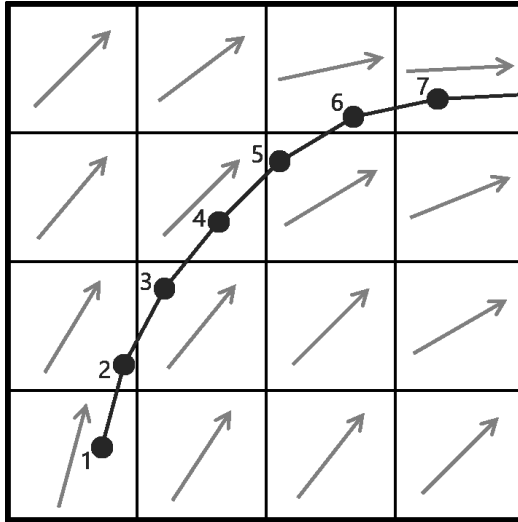
Figure 3.6: Schematic example of tractography. Given a starting point (1), a small step is made along the estimated local fiber direction (arrow), to end in point 2. This process is iteratively repeated (point 2 – 7) until a stop criterion is met.

The result of the fiber tracking algorithm depends on the choice of parameter settings. These can include the step size, the stop criterion, the maximum allowed curvature, and the interpolation method used to derive the local fiber orientation estimation at the exact coordinate within the voxel[23,208].

Tractography can be roughly subdivided into two methods: deterministic tractography and probabilistic tractography. In deterministic tractography given a certain starting point and a set of parameter values, the resulting fiber track will always be the same. This is because this method will only follow the 'best' direction in each point. For a diffusion tensor model, this is the principle eigenvector, and for CSD this is the direction of the peak in the fiber ODF closest to the current tracking direction[208]. Probabilistic tractography on the other hand follows in each point a direction that is randomly sampled from a probability density function of orientations. By

doing so, the algorithm becomes more robust to noise and other uncertainties in the probability density function[208]. This means that it will not only generate the best fitting fiber tracks, but also additional tracks that can be explained by the data. So, if multiple tracks were to be generated from the same seed point, they would still follow a different path. The distribution of fiber tracks that results from tracking many pathways from one seed region using probabilistic tractography is accordingly considered a probability distribution.

In the 3D space, the reconstructed fiber tracks are often color coded for direction: left-right orientations are red, anterior-posterior orientations are green, and inferior-superior orientations are blue. An example of the reconstructed fiber tracks of the corpus callosum, a major connection between the left and right hemispheres, using probabilistic spherical deconvolution based tractography is shown in Figure 3.7.
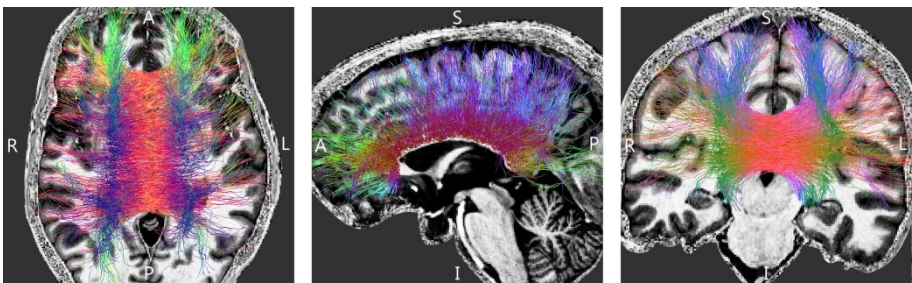
Figure 3.7: Axial, sagittal, and coronal views of the corpus callosum as reconstructed with probabilistic tractography. The orientations of the fibers are represented by the different colors (left-right = red, anterior-posterior = green, and inferior-superior = blue).

3.7 Field strength

In specialized neuroimaging centers, the possibilities of scanning at ultra-high field (7 T and higher) are increasingly being explored[67]. At ultra-high field, alterations of physical properties can influence measurements both positively and negatively. Several issues make ultra-high field scanning more sensitive to inhomogeneous signal-to-noise ratios (SNR) and contrast-to-noise ratios (CNR), geometric distortions, and movement artifacts. These include field strength dependent changes in relaxation times T1, T2, and T2*;

increased B0 and B1 magnetic field inhomogeneities; and increased risks of tissue heating[67]. This limits the use of T1-weighted, T2-weighted, and proton density-weighted turbo spin echo (TSE)[94] scan protocols that are commonly used in clinics. However, the alterations in relaxation times and the increased sensitivity to magnetic susceptibility have stimulated the focus of ultra-high field imaging to shift to susceptibility and T2*-dependent gradient echo[86] sequences. Furthermore, the SNR increases close to linearly with field strength, which offers the option to scan with higher spatial resolution[215] and/or CNR in a shorter time[67]. This makes ultra-high field MRI especially beneficial for detailed imaging of structures with altered magnetic susceptibility, such as the basal ganglia, myelin and blood. Finally, side-effects might occur during movement through the strong gradients. The majority of the subjects have been reported to feel sensations when moving into or out of the bore, which was rated as unpleasant vertigo in 5-20% of the subjects[78,206] and a small number of subjects (approximately 3%) experienced a medium or strong metallic taste[206].

CHAPTER 4

ULTRA-HIGH FIELD MRI OF THE BASAL GANGLIA

4.1 Abstract

Deep brain stimulation is a treatment for Parkinson's disease and other related disorders, involving the surgical placement of electrodes in the deeply situated basal ganglia or thalamic structures. Good clinical outcome requires accurate targeting. However, due to limited visibility of the target structures on routine clinical MR images, direct targeting of structures can be challenging. Non-clinical MR scanners with ultra-high magnetic field (7 T or higher) have the potential to improve the quality of these images. This technology report provides an overview of the current possibilities of visualizing deep brain stimulation targets and their related structures with the aid of ultra-high field MRI. Reviewed studies showed improved resolution, contrast, and signal-to-noise ratios at ultra-high field. Sequences sensitive to magnetic susceptibility such as T2* and susceptibility-weighted imaging and their maps in general showed the best visualization of target structures, including a separation between the subthalamic nucleus and the substantia nigra, the lamina pallidi medialis and lamina pallidi incompleta within the globus pallidus and substructures of the thalamus, including the ventral intermediate nucleus (Vim). This shows that the visibility, identification, and even subdivision of the small deep brain stimulation targets benefit from increased field strength. Although ultra-high field MR imaging is associated with increased risk of geometrical distortions, it has been shown that these distortions can be avoided or corrected to the extent where the effects are limited. The availability of ultra-high field MR scanners for humans seems to provide opportunities for a more accurate targeting for deep brain stimulation in patients with Parkinson's disease and related disorders.

4

4.2 Introduction

The basal ganglia are a group of nuclei deep in the brain, which play an important role in specific motor, limbic, and associative processes[204]. Anatomically, they consist of the caudate nucleus-putamen (also referred to as striatum), external and internal globus pallidus (GPe and GPi, respectively), substantia nigra (SN), and the subthalamic nucleus (STN). Structural or functional impairments of basal ganglia structures can lead to neurological and psychiatric disorders, e.g., Parkinson's disease (PD)[163], dystonia[222], Tourette's syndrome[153], and obsessive-compulsive disorder[138]. Although most of the patients with basal ganglia diseases can be managed by drug and/or behavioral therapy, an increasing number of patients are referred to specialized teams for deep brain stimulation (DBS)[3,59,124,129]. The main reasons for DBS referral include the proven benefit of DBS over best medical treatment[61,196] or insufficient response to non-surgical therapies. DBS is a minimally invasive surgical procedure and involves the implantation of stimulating electrodes with millimeter precision into a specific brain target. The brain regions targeted most often are located in the basal ganglia, and include the ventral parts of the striatum[59,141], the posteroventral part of the GPi[3,49,124], the ventral parts of the pallidum[3], the STN[72], and surrounding structures such as the ventrolateral and anterior parts of the thalamus[71].

Currently, there are three methods to locate the target for DBS:

- Using intraoperative neurophysiological mapping tools.

- Using stereotactic coordinates derived from post-mortem or MRI based atlases (indirect targeting).

- Via direct visualization on individual magnetic resonance (MR) images (direct targeting).

Combinations of these methods are generally used. Direct targeting has the advantage over indirect targeting in that it accounts for differences in individual anatomy, which is especially critical when small structures such as those in DBS are targeted. However, at standard clinical magnetic field strengths (1.5 T and 3 T) direct visualization often lacks contrast for very high precision DBS targeting. The increasing availability of ultra-high magnetic field (7 T or higher) MRI scanners promises direct, accurate visualization of target regions with a very high specificity. Although the

number keeps growing, at present an estimate of 61 human ultra-high field MRI scanners has been installed or will be installed in the near future (see Table 4.1). A better understanding of the structural and functional components of the basal ganglia and related structures at ultra-high resolution approaching the microscopic level, is not only expected to increase the accuracy of DBS, shorten surgery, and potentially improve the clinical outcomes[225,230], but also to enhance our understanding of brain function and disease states. In this technology report, we present the current options for detailed visualization of deep brain structures using multiple MRI contrasts at ultra-high magnetic field, based on a literature review.

English-language studies were searched on PubMed using combinations of title and abstract key words related to basal ganglia, thalamus, and ultra-high field MRI. Publications were selected by screening of titles and abstracts. Additional studies were found through the references cited in the selected articles.

In this technology report, anatomical structures are denoted in English, unless their Latin names are commonly used. We review the current literature on in vivo and ex vivo (i.e., post mortem) ultra-high field imaging of the basal ganglia and related structures.

4

Table 4.1: Overview of ultra-high magnetic field (7 T or higher) human MRI scanners that have been installed or will be installed in the future according to the institutions' websites. Because not all scanners are operational yet, the last column refers to publications in which the mentioned scanner is used.

No	Country	City	Institution	Man.	F	P
1	Australia	Melbourne	Melbourne Brain Centre	Siemens	7	
2	Australia	Brisbane	University of Queensland	Siemens	7	
3	Austria	Vienna	Medical University of Vienna	Siemens	7	[218]
4	Brazil	Sao Paulo	University of Sao Paulo	Siemens	7	
5	Canada	London	Western University	Siemens	7	[81]
6	Canada	Toronto	Toronto Western Hospital	Siemens	7	
7	China	Beijing	Chinese Academy of Sciences	Siemens	7	[93]
8	Denmark	Copenhagen	Hvidovre Hospital	Philips	7	
9	France	Marseille	Center for Magnetic Resonance in Biology and Medicine	Siemens	7	
10	France	Saclay	Neurospin	Siemens	7	[31]
11	France	Saclay	Neurospin	Custom built	11.7	[216]
12	Germany	Berlin	Berlin Ultrahigh Field Facility	Siemens	7	[218]
13	Germany	Bonn	German Center for Neurodegenerative Diseases	Siemens	7	[218]
14	Germany	Essen	University of Duisburg-Essen	Siemens	7	[218]
15	Germany	Heidelberg	German Cancer Research Center	Siemens	7	[218]
16	Germany	Jülich	Research Centre Jülich	Siemens	9.4	[13]
17	Germany	Leipzig	Max Planck Institute for Human Cognitive and Brain Sciences	Siemens	7	[55]
18	Germany	Magdeburg	Leibniz Institute for Neurobiology	Siemens	7	[218]
19	Germany	Tübingen	Max Planck Institute for Biological Cybernetics	Siemens	9.4	[37]
20	Italy	Pisa	Imago7 Foundation	GE	7	[47]
21	Japan	Niigata	University of Niigata	GE	7	[103]
22	Japan	Morioka	Iwate Medical University	GE	7	[192]
23	Japan	Suita City	Center for Information and Neural Networks		7	
24	Netherlands	Leiden	Leiden University Medical Center	Philips	7	[68]
25	Netherlands	Utrecht	University Medical Center Utrecht	Philips	7	[51]
26	Netherlands	Amsterdam	Spinoza Centre for Neuroimaging	Philips	7	
27	Netherlands	Maastricht	Maastricht University	Siemens	7	[99]
28	Netherlands	Maastricht	Maastricht University	Siemens	9.4	[44]
29	Republic of Korea	Icheon	Gachon University of Medicine and Science	Siemens	7	[42]

30	Sweden	Lund	Lund University	Philips	7	
31	Switzerland	Lausanne	Centre d'Imagerie BioMédicale	Siemens	7	[115]
32	Switzerland	Zürich	Swiss Federal Institute of Technology and University of Zurich	Philips	7	[227]
33	UK	Nottingham	University of Nottingham	Philips	7	[132]
34	UK	Oxford	University of Oxford	Siemens	7	[29]
35	USA	Auburn	Auburn University	Siemens	7	[58]
36	USA	Baltimore	Kennedy Krieger Institute	Philips	7	[98]
37	USA	Bethesda	National Institute of Health	Siemens	7	[75]
38	USA	Bethesda	National Institutes of Health	Siemens	11.7	
39	USA	Boston	Massachusetts General Hospital	Siemens	7	[15]
40	USA	Chapel Hill	University of North Carolina	Siemens	7	
41	USA	Chicago	University of Illinois	Custom built	9.4	[134]
42	USA	Cleveland	Cleveland Clinic	Siemens	7	
43	USA	Columbus	Ohio State University	Bruker	8	[32, 188]
44	USA	Columbus	Ohio State University	Philips	7	
45	USA	Minneapolis	University of Minnesota	Siemens	7	[2]
46	USA	Minneapolis	University of Minnesota	Siemens	7	
47	USA	Minneapolis	University of Minnesota	Siemens	10.5	
48	USA	Minneapolis	University of Minnesota	Varian	9.4	[53]
49	USA	Nashville	Vanderbilt University	Philips	7	[69]
50	USA	New Haven	Yale University	Varian	7	[172]
51	USA	New York	New York University School of Medicine	Siemens	7	[171]
52	USA	New York	Icahn School of Medicine at Mount Sinai	Siemens	7	
53	USA	Philadelphia	University of Pennsylvania	Siemens	7	[30]
54	USA	Pittsburgh	University of Pittsburgh	Siemens	7	[154]
55	USA	Portland	Oregon Health & Science University	Siemens	7	
56	USA	San Francisco	San Francisco Veterans Affairs Medical Center	Siemens	7	
57	USA	San Francisco	University of California	GE	7	[150]
58	USA	Dallas	University of Texas Southwestern Medical Center	Philips	7	[185]
59	USA	Iowa City	University of Iowa	GE	7	
60	USA	Milwaukee	Medical College of Wisconsin	GE	7	
61	USA	Stanford	Stanford University	GE	7	[109]

Man. = manufacturer. F = Field strength in Tesla. No = number. P = publication.

4.3   MRI of DBS targets at clinical field strengths of 1.5 T and 3 T

Direct visualization and targeting of DBS structures based on 1.5 T or 3 T MR images obtained in clinical practice can be challenging. Several studies compared different scanning sequences for the visibility of the STN[112,131], GPi[131,161], GPe[161], and zona incerta (ZI)[111] and showed that T2*[111,112,161] and quantitative susceptibility maps[131] outperformed T1 and T2-weighted images. Furthermore, 3 T functional and structural connectivity maps have been measured in healthy volunteers to visualize the functional subdivision of the STN, although higher spatial resolution is expected to reveal a more detailed anatomy[35]. Also, a literature review concluded that there is no consensus whether 1.5 T and 3 T MRI are reliable and accurate enough to be employed for direct targeting of the STN, due to serious shortcomings in the contrast between the STN and surrounding structures[36]. Visualization of the small substructures in the thalamus at lower field strengths is even less straightforward, primarily due to lack of contrast. One study identified four large thalamic nuclei groups on 3 T MPRAGE (magnetization-prepared rapid acquisition of gradient echo) images[27] and another study identified the centromedian nucleus directly on 3 T proton density-weighted MR images[105]. The thalamus was also segmented at 1.5 T and 3 T using diffusion-weighted imaging (DWI)[142,183,213,223] or a combination of ten different sequences[232].

Although several sequences have been investigated for the visualization of basal ganglia structures at clinical field strengths, DBS structures such as the motor part of the STN, and certain regions within the thalamus, such as the ventrolateral nuclei, need to be displayed more distinctively in order to rely on these images solely for targeting.

4.4   Ultra-high field imaging of the deep brain structures

Several studies identified deep brain (sub)structures at ultra-high field using different MRI contrasts. These studies, reviewed below, show the high potential of ultra-high field MRI to accurately identify and delineate thalamic, parathalamic and subthalamic nuclei. Table 4.2 shows detailed scanning parameters of the described studies, referred to by line numbers.

42

Table 4.2: Overview of acquisition parameters used in the described studies. A more detailed table is available in Plantinga et al., 2014[179].

Line number	Study	Subjects	Field strength (T)	Sequence	2D or 3D	Contrast	Orientation	Matrix size	Nr slices	Resolution (mm² or mm³)	Slice thickness (mm)	TR (ms)	TE (ms)	TI (ms)	Flip angle (deg)	Time (min:sec)
1	[32]	1 C	8	GE	2D	T2*w	Ax oblique	1024 x 1024	-	0.195	2	750	17		45	13
2	[162]	5 C	8	GE	-	-	Sag	512 x 512	-	0.390	2	1000	7		-	-
3	[1]	20 C	8	GE	-	magnitude, phase, SWI	-	512 x 512	-	3.9 x 3.9	5	500-600	7		±20	-
4	[42]	C	7.0	GE	2D	T2*w	Ax, sag, cor	-	15	0.25	2	750	17.8		30/45	12:30
5	[2]	6 C	7	MPRAGE	3D	T1w	-	256 x 192 x 176		1 x 1 x 1		2560	4.29	1500	6	3:30
6	[2]	6 C	7	TSE	2D	T2w	-	512 x 512	30	0.375 x 0.375 x 2.0		7150	68		-	7
7	[2]	6 C	7	GE	3D	SWI	-	512 x 512 x 72		0.375 x 0.375 x 1.0		28	20		10	7
8	[2]	6 C	7	GE	3D	SWI	-	384 x 240 x 88		0.67 x 0.67 x 0.67		28	20		-	15
9	[69]	10 C	7	GRASE	2D	T2w+T2*w	Ax oblique	320 x 256	14	0.4 x 0.4	2	5000	22		79	11:12
10	[69]	10 C	7	GE	3D	T2*w	Ax oblique	320 x 256 x 14		0.4 x 0.4 x 2		25	18		15	5:26
11	[193]	8 C	7	M-GE	3D	T2*w, T2* map, χ-map	Cor	-	56	0.5 x 0.5 x 0.6		40	11.22, 21.41, 31.59		-	14:20
12	[56]	9 C	7	S-GE	3D	χ-map	Ax	576 x 414 x 256		0.4 x 0.4 x 0.4		17	10.5		8	16:57
13	[56]	9 C	7	M-GE	3D	R2* maps	-	320 x 210 x 128		0.8 x 0.8 x 0.8		34	5, 12.8, 20.6, 28.4		8	8:39
14	[128]	4 C	7	EPI	2D	Diffusion	-	128 x 128	66	1.5 x 1.5	1.5	5000	50		90	12
15	[40]	4 C	7.0	EPI	-	TDI	-	128 x 128	45	1.8 x 1.8	1.8	6000	83		-	-

Line number	Study	Subjects	Field strength (T)	Sequence	2D or 3D	Contrast	Orientation	Matrix size	Nr slices	Resolution (mm² or mm³)	Slice thickness (mm)	TR (ms)	TE (ms)	TI (ms)	Flip angle (deg)	Time (min:sec)
16	[187]	1 pm	9.4	SD	-	T2w	Ax	256 x 256	-	0.100 x 0.100	1	-	16, 22, 40		-	-
17	[187]	1 pm	9.4	SD	-	T2w	Cor	352 x 256	-	0.100 x 0.100	1	-	16, 22, 40		-	-
18	[187]	1 pm	9.4	SD	-	T2w	Sag	352 x 256	-	0.100 x 0.100	1	-	16, 22, 40		-	-
19	[199]	3 pm	7.0	MPRAGE	3D	T1w	-	256 x 256 x 112		0.150 x 0.150 x 0.600		4000	3.5	1100	-	119:0
20	[146]	1 pm	9.4	SE	-	T2w	Ax	1024 x 1024	-	0.044 x 0.044	0.5-1	2000–2200	15-22		-	4320:0
21	[146]	8 pm	9.4	SE	-	T2w	Ax (n=8), Cor (n=1), Sag (n=1)	512 x 512	-	0.088 x 0.088	0.5-1	2000–2200	15-22		-	up to 600
22	[73]	9 pm	21.1	FLASH GE	3D	-	-	-	-	0.050 x 0.050 x 0.050		50	4		-	258:0
23	[220]	5 C 1 ph	7	GE FLASH	3D	χ-map	Ax	286 x 286 x 143		0.7 x 0.7 x 0.7		23	15		12	3:30
24	[110,113]	9 C	7.0	GE	-	T1w	Sag	448 x 448	-	0.513 x 0.513	0.649	6.6	2.38		12	6:38
25	[110,113]	9 C	7.0	TSE	-	T2w	Ax	624 x 768	-	0.286 x 0.286	2	13,140	57		-	4:37
26	[110,113]	9 C	7.0	FLASH	2D	T2*w	Ax	704 x 704	-	0.25 x 0.25	2	504	17		30	5:55
27	[110,113]	9 C	7.0	FLASH	2D	T2*w	Cor	704 x 704	-	0.25 x 0.25	2	504	17		30	5:55
28	[110,113]	9 C	7.0	FLASH	2D	T2*w	Sag	704 x 704	-	0.25 x 0.25	2	504	17		30	6:49
29	[110,113]	9 C	7.0	SWI	-	SWI	Cor	288 x 384	-	0.52 x 0.52	0.5	13.3	21		5	13:21
30	[55]	6 C	7	GRASE	2D	T2w	Cor	384 x 384	35	0.53 x 0.53	0.6	10,000	35		-	7:22

Line number	Study	Subjects	Field strength (T)	Sequence	2D or 3D	Contrast	Orientation	Matrix size	Nr slices	Resolution (mm² or mm³)	Slice thickness (mm)	TR (ms)	TE (ms)	TI (ms)	Flip angle (deg)	Time (min:sec)
31	55	6 C	7	MP2RAGE	-	R1 map	Cor	320 x 260 x 240		0.6 x 0.6 x 0.6		5000	3.7	900, 2750	-	17:40
32	55	6 C	7	GE	3D	R2* map, χ-map	Cor	448 x 364 x 104		0.43 x 0.43 x 0.43		43	11, 21, 31		12.5	17:48
33	229	9 C	1.5	GE	2D	T2*w	Ax	256 x 192	16	0.94 x 0.94	2	1000	7.3, 23.9, 40.5, 57.0		60	26
34	229	9 C	3	GE	2D	T2*w	Ax	256 x 192	16	0.94 x 0.94	2	1000	7.5, 21.7, 35.9, 50.0		60	13
35	229	9 C	7	GE	2D	T2*w	Ax	256 x 192	16	0.94 x 0.94	1	1000	9.6, 16.4, 23.2, 30.0		60	13
36	43	11 C 1 P	1.5	GE	2D	T2*w	-	384 x 384	-	0.5 x 0.5	2	750	30		30	4:50
37	43	11 C 1 P	3	GE	2D	T2*w	-	384 x 384	-	0.5 x 0.5	2	625	30		30	4:02
38	43	11 C 1 P	7	GE	2D	T2*w	-	704 x 704	-	0.25 x 0.25	2	500	17.8		30	5:54
39	111,112	9 C	3	MPRAGE	-	T1w	Sag	430 x 512	-	0.49 x 0.49	1	1900	2.26	1900	9	3:58
40	111,112	9 C	3	FLAIR	-	T2w	Ax	265 x 200	-	0.43 x 0.43	4	9000	95	2500	-	5:34
41	111,112	9 C	3	SPACE	-	T2w	Ax	290 x 384	-	0.6 x 0.6	0.6	3200	353		-	3:58
42	111,112	9 C	3	FLASH	2D	T2*w	Ax	384 x 384	-	0.5 x 0.5	2	625	25		30	4:00
43	111,112	9 C	3	FLASH	2D	T2*w	Cor	384 x 384	-	0.5 x 0.5	2.5	625	25		30	4:00
44	111,112	9 C	3	FLASH	2D	T2*w	Sag	384 x 384	-	0.5 x 0.5	2.5	625	25		30	4:24

Line number	Study	Subjects	Field strength (T)	Sequence	2D or 3D	Contrast	Orientation	Matrix size	Nr slices	Resolution (mm² or mm³)	Slice thickness (mm)	TR (ms)	TE (ms)	TI (ms)	Flip angle (deg)	Time (min:sec)
45	[111,112]	9 C	3	FLASH-HB	2D	T2*w	Ax	384 x 384	-	0.49 x 0.49	2	625	30		20	4:00
46	[111,112]	9 C	3	SWI	-	SWI	Ax	221 x 320	-	0.75 x 0.75	1.2	28	20		15	5:04
47	-	1 C	7.0	GE	3D	T2*w	Ax	312 x 384 x 112		0.5 x 0.5 x 0.5		33	23.27		10	12:23
48	-	1 C	7.0	M-GE	3D	R2* map	Ax	312 x 384 x 112		0.5 x 0.5 x 0.5		33	3.56, 10.13, 16.7, 23.27		10	12:23

Ax = Axial. C = Controls. Cor = Coronal. EPI = Echo planar imaging. FLAIR = Fluid attenuation inversion recovery. FLASH = Fast low angle shot. FLASH-HB = FLASH with high bandwidth. GE = Gradient echo. GRASE = Gradient and h. M-GE = Multi-echo GE. MPRAGE = Magnetization prepared rapid gradient echo. MP2RAGE = Magnetization prepared 2 rapid acquisition gradient echoes. pm = post mortem. P = Parkinson's disease patient. ph = phantom. Sag = Sagittal. SD = Spin density. SE = Spin echo. S-GE = Single-echo GE. SPACE = Sampling perfection with application of optimized contrasts using different flip angle evolutions. SWI = Susceptibility-weighted imaging. T1w = T1-weighted. T2w = T2-weighted. T2*w = T2*-weighted. TDI = Track density imaging. TI = Inversion time. TR = Repetition time. TSE = Turbo spin echo. χ-map = Susceptibility map.

4.4.1 Visualization of deep brain structures at ultra-high field in vivo

Since the installation of the first ultra-high field MRI scanner, several studies investigated the visualization of deep brain structures at ultra-high field in vivo (Table 4.3).

Table 4.3: Overview of the basal ganglia and related (sub)structures that have been identified using different in vivo protocols at ultra-high field MRI. The last column refers to the line of Table 4.2 that gives more details about the scan protocols used.

Study	Image type	Findings	Line
Bourekas, 1999[32]	T2*w	GP, SN and RN appear hypointense	1
Novak, 2001[162]		GP, SN and RN appear hypointense	2
Abduljalil, 2003[1]	GE Magnitude	SN and RN appear hypointense	3
	GE Phase	Substructures within SN and RN	3
Cho, 2008[42]	GE	SN and RN in coronal plane hypointense	4
Cho, 2010[43]	Coronal GE	Discrimination of STN and SN	38
Abosch, 2010[2]	SWI	Clear delineation of STN Boundary between STN and SN Lamina pallidi medialis and lamina pallidi incompleta Vim, anterior and medial boundaries of pulvinar, boundary of the nucleus ventralis caudalis	7-8
Eapen, 2011[69]	T2w and T2*w	Subregions within RN	9
	T2*w	Subregions within RN and SN	10
Schäfer, 2012[193]	χ-map	Boundary between STN and SN	11
Deistung, 2013[56]	χ-map	Subnuclei within the SN Discrimination of the STN from the SN and surrounding gray and white matter Lamina pallidi medialis and lamina pallidi incompleta Medullary lamina in RN Vim, pulvinar, lateral and medial geniculate nucleus, dorsomedial nucleus and dorsal nuclei group	12
	R2* map	Substructures in RN	13
Lenglet, 2012[128]	Tractography	Projection based subdivisions of the SN, STN, GP and thalamus	14
Calamante, 2012[40]	TDI	Signal intensity differences within thalamus	15

*GE = Gradient echo. GP = Globus pallidus. RN = Red nucleus. SN = Substantia nigra. STN = Subthalamic nucleus. SWI = Susceptibility-weighted imaging. T2w = T2-weighted. T2*w = T2*-weighted. TDI = Track density imaging. Vim = Ventral intermediate nucleus. χ-map = Susceptibility map.*

In 1999, the basal ganglia were visualized at ultra-high field (8 T) using a two-dimensional (2D) multi-slice gradient echo (GE) sequence, where high resolution (195 x 195 μm in-plane) T2*-weighted axial images of one volunteer were obtained in 13 minutes (Table 4.2-1)[32]. On these images the globus pallidus (GP), SN, and red nucleus (RN) appeared as hypointense regions. These findings were later confirmed in sagittally recorded slices with similar acquisition parameters (Table 4.2-2)[162]. In 2003, the same group showed that on GE phase images (Table 4.2-3), within the SN, the SN pars dorsalis and SN pars lateralis had a higher signal intensity than the matrix of the SN, and within the RN, the medullary lamella showed a higher signal intensity than the RN pars oralis[1]. A few years later, again the SN and RN appeared hypointense on 7 T axial, sagittal, and coronal GE images (Table 4.2-4)[42] and in 2010, 7 T coronal GE images (Table 4.2-38) were obtained on which the STN and SN could be well distinguished[43].

A more detailed description of the visualization of the basal ganglia at 7 T with three different scanning sequences, exploiting T1-weighted, T2-weighted and susceptibility-weighted imaging, was published in 2010 (Table 4.2-5:8)[2]. Using susceptibility-weighted imaging (SWI), a clear delineation of the STN and the boundary dividing it from the SN were visualized in both axial and coronal planes (Figure 4.1 A). Also, SWI allowed visualization of varying levels of contrast within the RN and two of the laminae within the GP (lamina pallidi medialis and incompleta), thus also distinguishing between the GPi and the GPe. Within the thalamus, it showed intensity variations corresponding to the locations of the ventral intermediate nucleus (Vim), the anterior and medial boundaries of the pulvinar, and the boundary of the nucleus ventralis caudalis as identified with the Schaltenbrand and Wahren atlas[195].

In 2011, Eapen et al. imaged several deep brain structures with two different sequences at 7 T: T2 and T2*-weighted gradient and spin echo (GRASE) and T2*-weighted GE (Table 4.2-9:10)[69]. Both GRASE and GE scans showed a clear distinction between the densely and the poorly vascularized regions of the RN, but only the GE scan also showed signal intensity differences within the SN, possibly representing the SN pars compacta and SN pars reticulata. In two later studies, susceptibility maps were investigated. Using a multi-echo GE sequence (Table 4.2-11), a boundary between the STN and the SN was shown[193]. The use of susceptibility maps generated from three
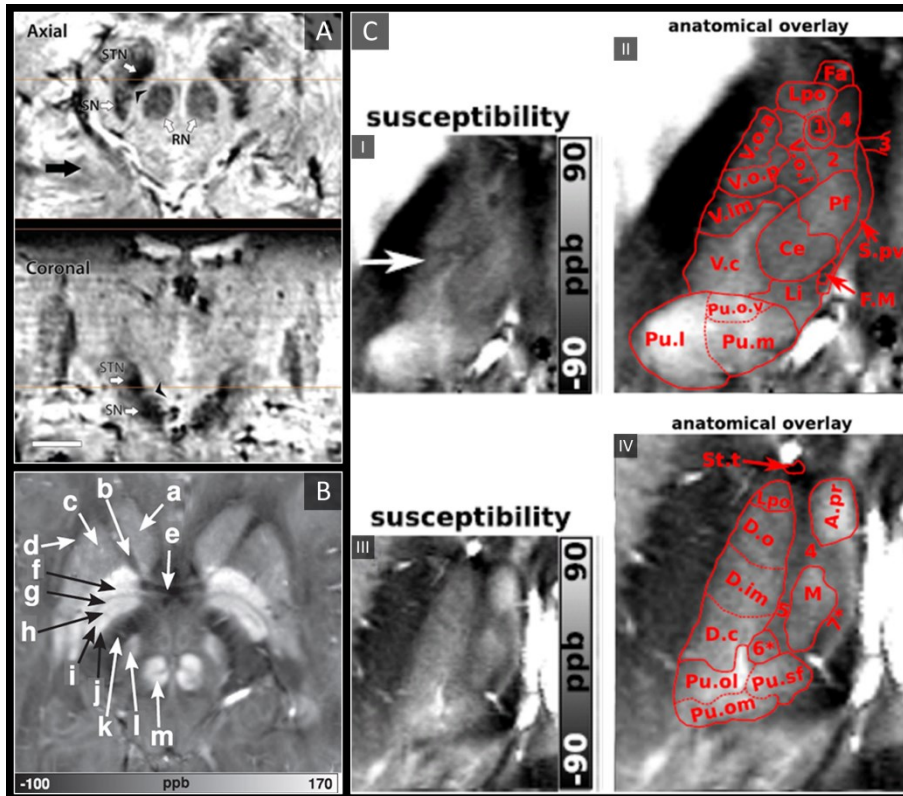
4

Figure 4.1: Examples of structures identified at ultra-high field. A) Ultra-high field (7 T) susceptibility-weighted axial and coronal images show a clearly delineated subthalamic nucleus (STN), a boundary between the STN and substantia nigra, and heterogeneous signal intensity in the red nucleus. Adopted with permission from Abosch et al.[2]. B) Axial 7 T susceptibility map. Adopted with permission from Deistung et al.[56]. a = head of the caudate nucleus. b = anterior limb of the internal capsule. c = putamen. d = external capsule. e = anterior commissure. f = external globus pallidus. g = lamina pallidi medialis. h = pallidum mediale externum. i = lamina pallidi incompleta. j = pallidum mediale internum. k = posterior limb of internal capsule. l = subthalamic nucleus. m = red nucleus. C) Ultra-high field (7 T) susceptibility maps of inferior (I and II) and superior (III and IV) sections of the thalamus. Figures II and IV show overlays of substructures of the thalamus according to the Schaltenbrand and Wahren atlas[195] on the images shown in Figures I and III respectively. The pulvinar (Pu.l) can be distinguished from Figures I and II and the dorsomedial nucleus (M) and dorsal nuclei group (D.o and D.im) can be seen in Figures III and IV. Adopted with permission from Deistung et al.[56].

single-echo GE phase data sets with different head positions (Table 4.2-12) also facilitated detailed visualization of structures[56]. It provided discrimination between the subnuclei within the SN, and allowed for accurate discrimination of the STN from the SN and surrounding gray matter and white matter. Furthermore, within the GP, these maps showed the lamina pallidi medialis and lamina pallidi incompleta (Figure 4.1 B). The RN displayed substructures in the susceptibility maps, facilitating identification of the medullary lamella, and the RN pars oralis and RN pars dorsomedialis showed a significantly increased susceptibility, compared to the RN pars caudalis. Finally, within the thalamus clear intensity variations were observed on these susceptibility maps corresponding to the Vim, pulvinar, lateral and medial geniculate nucleus, dorsomedial nucleus, and dorsal nuclei group as identified with the Schaltenbrand and Wahren atlas[195] (Figure 4.1 C).

In two other studies by Kerl et al., investigating the STN and ZI with different sequences at 7 T[110,113], a distinction could be seen between the STN and the SN and ZI, and a clear boundary was visible dividing the rostral ZI from the internal capsule, STN, and the pallidofugal fibers on T2*-weighted images and the latter also on coronal susceptibility-weighted (SW) images.

Finally, two studies employed DWI properties to identify substructures within the DBS related structures. In one study, DWI (Table 4.2-14) was used to estimate the pathways between seven regions of interest: caudate nucleus, putamen, GPe, GPi, SN, STN, and thalamus[128]. Seven pathways could be successfully identified: the nigrostriatal, nigropallidal, nigrothalamic, subthalamopallidal, pallidothalamic, striatopallidal, and thalamostriatal pathway. These projections were also used to create subparcellations of the SN, possibly corresponding to the SN pars reticulata and SN pars compacta; subdivisions of the STN into a dorsolateral and ventromedial part; subdivisions of the GPe into medial, lateral and rostro-ventral parts; subdivisions of the GPi into laterocaudal, rostral, and mid portions; and many subdivisions within the thalamus. In another study, 7 T DWI (Table 4.2-15) was used to construct track-density images of the thalamus[40]. These showed high resolution (200 µm isotropic) substructures within the thalamus with clear intensity differences, not only related to track-density, but also to the directionality of the fibers.

4.4.2 Visualization of deep brain structures at ultra-high field ex vivo

When scanning ex vivo, even higher resolution and higher signal-to-noise ratios (SNR) can be obtained due to the possibility of longer scan times and less movement artifacts. Although fixed tissue may suffer from altered tissue properties, such as decreases in T1 and T2[212] and a decreased diffusion coefficient[48], which is especially challenging for DWI, it also has great advantages over in vivo MRI. Several studies employed ex vivo imaging for investigating the deep brain structures at ultra-high field (Table 4.4).

Table 4.4: Overview of the basal ganglia and related (sub)structures that have been identified using different ex vivo protocols at ultra-high field MRI. The last column again refers to the line of Table 4.2 that gives more details about the scan protocols used.

Study	Image type	Findings	Line
Rijkers, 2007[187]	T2w	Visualization of the pulvinar, the lateral and medial geniculate bodies, cerebral peduncle, habenulointerpeduncular tract, periaquadactal gray, the medial lemniscus, the spinothalamic tract, the mammillothalamic tract, and the superior colliculus.	16:18
Soria, 2011[199]	T1w	Visibility of SN and RN	19
Massey, 2012[146]	T2w	Hypointense band between SN and STN High detailed visibility of STN and surrounding Intensity differences between anteromedial and posterolateral part of STN	21
	T2w	Fibers of the subthalamic fasciculus	20
Foroutan, 2013[73]	FLASH GE	High-detail images of SN, RN, putamen, and a clear separation of the GP into its external and internal part.	22

FLASH = Fast low angle shot. GE = Gradient echo. GP = Globus pallidus. RN = Red nucleus. SN = Substantia nigra. STN = Subthalamic nucleus. T1w = T1-weighted. T2w = T2-weighted.

In 2007, the STN and its surroundings were explored at 9.4 T with a T2-weighted sequence (Table 4.2-16:18) in a post mortem brain sample[187]. Acquiring a high in-plane resolution of 100 x 100 µm, not only the most prominent structures of the basal ganglia were visualized, but also the pulvinar, the lateral and medial geniculate bodies, cerebral peduncle, habenulointerpeduncular tract (fasciculus retroflexus), periaquaductal gray, the medial lemniscus, the spinothalamic tract, the mammillothalamic tract, and the superior colliculus.

Three post mortem brain stems have also been imaged at 7 T for 119 minutes, acquiring 150 x 150 μm images. On these T1-weighted images (Table 4.2-19), the RN and SN, which displayed heterogeneous signal intensity, could be visualized[199]. Even higher in-plane resolutions of 44 x 44 μm and 88 x 88 μm (Table 4.2-20:21) were achieved in a different study after scanning post mortem brain samples for 72 and 10 hours respectively[146]. The obtained T2-weighted images facilitated visualization of the STN, SN, RN, ZI, and thalamus but also allowed a highly detailed identification of many smaller structures surrounding the STN. Furthermore, a hypointense signal band was seen between the SN and STN facilitating easy separation of the two structures. Also the anteromedial part of the STN was relatively hypointense compared to the posterolateral portion, which might be related to the subdivision of the STN into a limbic, associative, and sensorimotor part. On the 44 x 44 μm resolution images even the fibers of the subthalamic fasciculus were visualized accurately.

Finally, one study that focused on differences in T2 and T2* values and iron content between post mortem brains of progressive supranuclear palsy patients and controls, showed high resolution (50 μm isotropic) fast low-angle shot (FLASH) GE images (Table 4.2-22), displaying with much detail the SN, RN, putamen, and the GP with a clear separation into the GPe and GPi[73].

These studies show that ultra-high field MRI can aid substantially in the identification of small (sub)structures including the separation between the STN and SN and the laminae within the GP both ex vivo and in vivo.

4.4.3   *Comparison between sequences for ultra-high field imaging*

In addition to the qualitative description of the visibility of deep brain structures with ultra-high field MRI, comparisons between different sequences and image reconstruction methods have been made (see Table 4.5).

In a previously mentioned study from 2003, magnitude, phase-weighted magnitude (SWI), and phase images of a GE dataset (Table 4.2-3), were compared for their capability to visualize (sub)structures[1]. On magnitude images the SN and RN showed up hypointense and on phase images, substructures within the SN could be distinguished as well. The combined

magnitude and phase images added little extra to the magnitude and phase images separately.

Table 4.5: Overview of comparative studies at ultra-high field. The third column refers to the line of Table 4.2 that gives more details about the scan protocols used. Sequences that give significantly better results than T2-weighted images are denoted with a double dagger (‡).

Study	Sequences	Line	Measure	Findings
Abduljalil, 2003[1]	GE magnitude	3	Qualitative	Phase images show additional structures to magnitude images
	GE SWI	3		
	GE phase	3		Magnitude + Phase ≥ SWI
Wharton, 2010[220]	MO χ-map	23	Artifacts and Δχ	Least noise related artifact and most accurate Δχ in MO
	RSO χ-map	23		
	TSO χ-map	23		MO≈RSO≈TSO
Abosch, 2010[2]	T1w	5	Qualitative	SWI > T2w > T1w
	T2w	6		
	SWI	7:8		
Eapen, 2011[69]	T2w + T2*w	9	CNR of RN/VTA	T2w +T2*w > T2*w
	T2*w	10		
Schäfer, 2012[193]	T2*w	11	CNR	χ-map > T2*w > T2* map
	T2* maps	11		
	χ-map	11		
Kerl 7T STN, 2012[113] Kerl 7T rZI, 2013[110]	T1w	24	SNR STN	T2*w‡> T1w‡ > SWI-MIP‡>SWI cor‡ > T2w
	T2w	25	CNR STN	T2*w‡> SWI-MIP‡>T2 > SWI > T1w
	T2*w	26:28	SNR rZI	T2*w‡>SWI-MIP‡>T1‡>SWI>T2w
	SWI	29	CNR rZI	T2*w‡> SWI-MIP‡>T2>SWI>T1w
	SWI-MIP	29		
Deistung, 2013[56]	GE magnitude	12	Qualitative	χ-map showed most detail
	GE phase	12		
	χ-map	12		
	R2* map	13		
Deistung, 2013[55]	T2w	30	CNR SN	χ-map > R2* map > T2w > R1 map
	R1 map	31	CNR RN	χ-map > R2* map > T2w > R1 map
	R2* map	32		
	χ-map	32		

CNR = Contrast-to-noise ratio. cor = coronal. GE = Gradient echo. MIP = Minimum intensity projection. MO = Multi-orientation. RN = Red nucleus. RSO = Regularized single-orientation. rZI = rostral part of zona incerta. SNR = Signal-to-noise ratio. STN = Subthalamic nucleus. SWI = Susceptibility-weighted imaging. T1w = T1-weighted. T2w = T2-weighted. T2*w = T2*-weighted. TSO = Threshold based single orientation. VTA = Ventral tegmental area. χ-map = Susceptibility map.

Later, in 2010, the mean susceptibility difference ($\Delta\chi$) between compartments in an agar phantom, and between white matter and deep brain structures of healthy subjects were compared among three different susceptibility mapping methods applied to GE FLASH images acquired at 7 T (Table 4.2-23)[220]. The mapping methods consisted of a) a multi-orientation method using images acquired with differing head positions, b) a regularized single-orientation method, and c) a threshold-based single-orientation method. Although all three methods showed large $\Delta\chi$ in the GP, SN, RN, internal capsule, putamen, and caudate nucleus, the multi-orientation method resulted in the least noise-related artifacts and good estimation of $\Delta\chi$ values in the phantom.

In another 2010 study, T1-weighted, T2-weighted, and SW imaging (Table 4.2-5:8) were compared[2]. Most structures were identified in the SW images (see Table 4.3), followed by the T2-weighted images (Figure 4.2). The T1-weighted images showed no obvious structures. Eapen et al. also quantitatively compared their T2+T2*- and T2*-weighted images (Table 4.2-9:10)[69]. No difference between both sequences could be found in the contrast-to-noise ratio (CNR) between the SN and ventral tegmental area and between the SN and RN, but in the T2+T2*-weighted images, the CNR between RN and ventral tegmental area was significantly better than in the T2*-weighted images.

In 2012, again differently reconstructed images derived from a multi-echo GE sequence (Table 4.2-11) were compared, consisting of T2*-weighted magnitude images, T2* maps, and susceptibility maps[193]. In most subjects, the CNR between the SN and STN was highest in the susceptibility maps, suggesting that these are most suitable for differentiating the STN from the SN. The SNR of the STN and the rostral part of the ZI and the CNR between these structures and white matter, imaged with different sequences, were investigated in two studies that compared T1-weighted GE, T2-weighted turbo spin echo (TSE), T2*-weighted FLASH and SW images (Table 4.2-24:29)[110,113]. Furthermore, minimum intensity projections (MIPs) of the SW images were computed. After adjusting the SNR and CNR for differences in voxel size, they were highest on the T2*-weighted images for both structures. Furthermore, the SNRs of both structures on the T2*-weighted, T1-weighted, SWI-MIP (and for the STN also on the coronal SW images) were significantly higher than those of the T2-weighted images. The CNRs
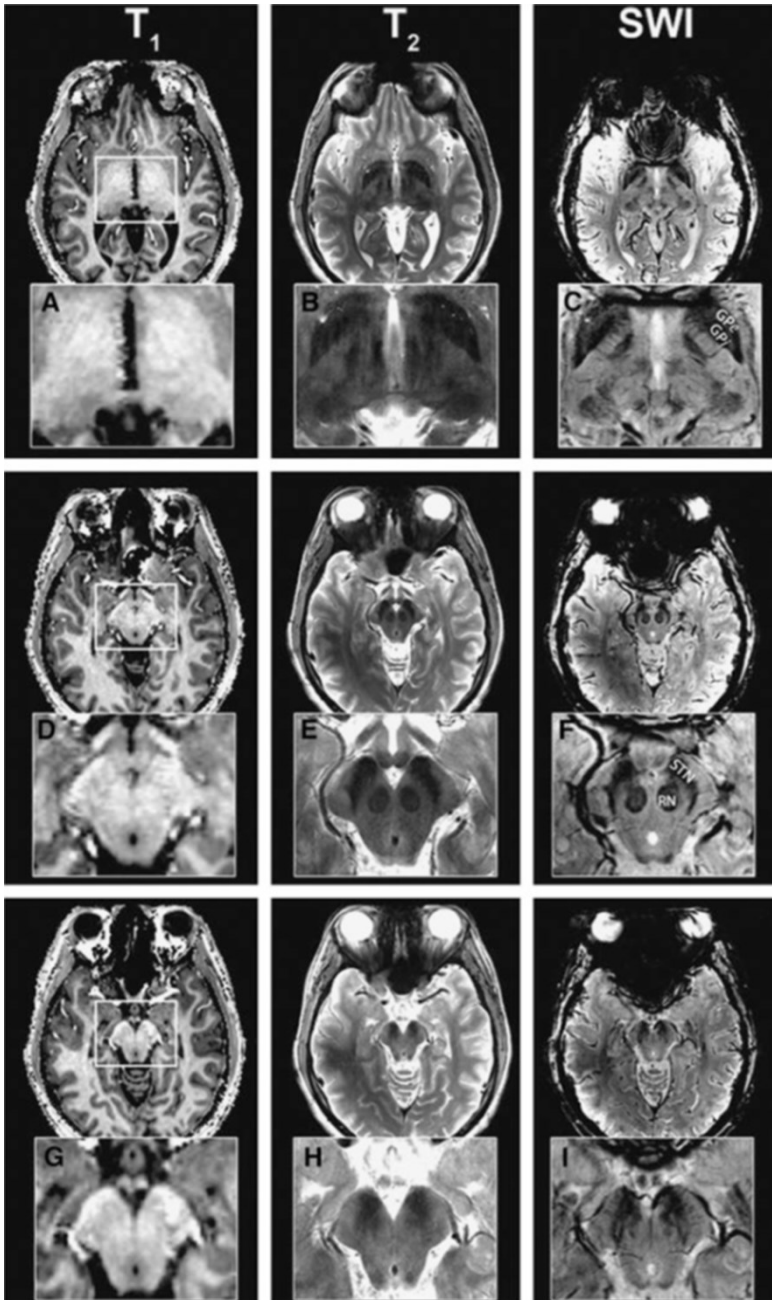
Figure 4.2: Ultra-high field (7 T) T1-weighted (A, D, G), T2-weighted (B, E, H) and susceptibility-weighted (C, F, I) images at different levels. The susceptibility-weighted images show the highest detail followed by the T2-weighted images. Adopted with permission from Abosch et al.[2].

of both structures on the T2*-weighted and for the rostral ZI also on the SWI-MIP images were also significantly higher than on the T2-weighted images. Also, a 2013 study compared image reconstruction techniques at 7 T consisting of a) magnitude, b) frequency and c) susceptibility maps derived from GE scans (Table 4.2-12), and d) R_2* maps derived from multi-echo GE scans (Table 4.2-13)[56]. Qualitative analysis by a neuroanatomist revealed that susceptibility maps in general facilitated the most detailed visualization of structures. Finally, in a recent study by the same group, the CNR between several brain stem structures and their surroundings were compared between sequences (Table 4.2-30:32)[55]. For the RN and the SN, the CNR of the R2* map and the susceptibility map outperformed those of the R1 map and the T2-weighted image.

Although comparison between studies is difficult due to the differences in scanning conditions, the majority of these studies show that sequences that are sensitive to magnetic susceptibility such as SWI and T2*-related images are most suitable for targeting basal ganglia structures and their subdivisions in DBS at ultra-high field.

4.4.4   *Comparison between field strengths*

In addition to comparisons between different sequences, some studies compared similar sequences between different field strengths (see Table 4.6).

In a 2008 study, the difference between a 7 T GE image (Table 4.2-4) and a 1.5 T image was briefly treated[42]. Visual inspection showed that the 7 T image displayed better contrast, SNR and resolution. However, comparison is difficult because the acquisition parameters of the 1.5 T image were unfortunately not provided. In the same year, T2*-weighted GE images were investigated, acquired at several echo times at three different field strengths: 1.5 T, 3 T and 7 T (Table 4.2-33:35)[229]. This showed that increasing field strength resulted in a higher influence of iron on the value of R2*, making this contrast useful for iron-rich deep brain structures, such as the GP, RN, SN, and putamen[87]. A thorough quantitative investigation of the visibility of the STN related to field strength was performed in 2010[43], comparing the contrast between the STN and a baseline (containing the ZI and thalamus), the contrast between the STN and SN, the SNR in gray matter areas, and the slope of signal increase between STN and baseline among 1.5 T, 3 T and 7 T T2*-weighted GE images (Table 4.2-36:38). At higher field strengths, the

Table 4.6: Overview of studies that compare scan protocols between field strengths. The third column refers to the line of Table 4.2 that gives more details about the scan protocols used. Sequences that significantly improve imaging at 7 T compared to 1.5 T and 3 T are denoted with a double dagger (‡).

Study	Sequence	Line	Measure	Findings
Cho, 2008[42]	1. 1.5T 2. 7T T2*w	 4	Qualitative	7T has better contrast, SNR and resolution than 1.5T
Yao, 2009[229]	1. 1.5T T2*w 2. 3T T2*w 3. 7T T2*w	33 34 35	R2*	R2* becomes more sensitive to iron with increasing field strength
Cho, 2010[43]	1. 1.5T T2*w 2. 3T T2*w 3. 7T T2*w	36 37 38	Contrast Slope of signal increase SNR	$7T^{‡}>3T>1.5T$ $7T>3T>1.5T$ $7T^{‡}>3T>1.5T$
Kerl, 2012[112] Kerl, 2012[111] Kerl, 2012[113] Kerl, 2013[110]	1. 3T T1w 2. 3T T2w FLAIR 3. 3T T2w SPACE 4. 3T T2*w 5. 3T SWI 6. 3T SWI-MIP 7. 7T T1w 8. 7T T2w TSE 9. 7T T2*w 10. 7T SWI 11. 7T SWI-MIP	39 40 41 41:45 46 46 24 25 26:28 29 29	SNR CNR	3T T1w > 7T T1w 7T T2*w > 3T T2*w 7T SWI-MIP > 3T SWI-MIP axial 3T T2w SPACE > 7T T2w > 3T T2w FLAIR 7T SWI > 3T SWI 7T T2*w > 3T T2*w 7T SWI-MIP > 3T SWI-MIP 7T T2w > 3T T2w SPACE > 3T T2w FLAIR 7T SWI > 3T SWI 7T T1 > 3T T1

CNR = Contrast-to-noise ratio. FLAIR = Fluid attenuated inversion recovery. MIP = Minimum intensity projection. rZI = rostral part of zona incerta. SNR = Signal-to-noise ratio. SPACE = Sampling perfection with application of optimized contrasts using different flip angle evolutions. STN = Subthalamic nucleus. SWI = Susceptibility-weighted imaging. T1w = T1-weighted. T2w = T2-weighted. T2*w = T2*-weighted. TSE = Turbo spin echo.

STN, SN, putamen, GPi, and GPe could be visualized while the boundaries of these structures were unclear on the 1.5 T images (Figure 4.3). Furthermore, all quantitative measures increased with field strength, and the SNR and contrast were significantly improved at 7 T compared to 1.5 and 3 T. Finally, the two studies by Kerl et al. investigating the STN and the rostral ZI at 7 T[110,113] were additionally performed at 3 T. Again, they compared the SNR and CNR of these structures between different sequences: T1-weighted MPRAGE, T2-weighted FLAIR (fluid attenuated inversion recovery), T2-weighted SPACE (sampling perfection with application of optimized contrasts using different flip angle evolutions), two

T2*-weighted 2D FLASH (FLASH2D) sequences, and SW images and their MIPs (Table 4.2-39:46)[111,112]. This makes it possible to compare the SNRs and CNRs of the different studies between field strengths, when adjusted for voxel size, although it should be noted that for the T1 and T2-weighted images different sequences were used between field strengths. For both structures, the SNRs of the T2*-weighted, SWI-MIP and SW images of the 7 T images were higher than those of the 3 T images, but the SNRs of the 3 T T2-weighted SPACE image and T1-weighted images were higher at 3 T than at 7 T. However, the CNRs of both structures were substantially higher on all the 7 T sequences than on the corresponding 3 T sequences.
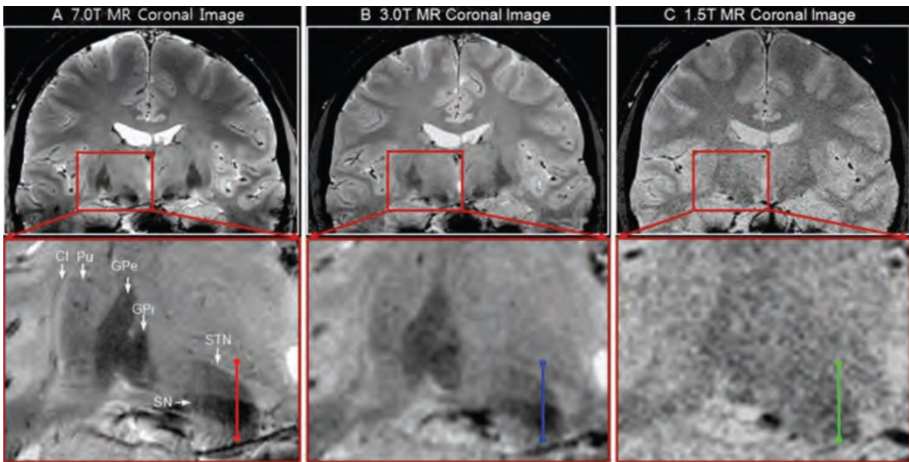

Figure 4.3: Coronal T2-weighted images obtained at 7.0 T (A), 3.0 T (B) and 1.5 T (C). Visual inspection shows a clearer identification of the substantia nigra (SN), subthalamic nucleus (STN), internal globus pallidus (GPi), external globus pallidus (GPe), and putamen (Pu) at 7 T compared to 3 T and 1.5 T. Adopted with permission from Cho et al.[43].*

These studies suggest that 7 T MRI can better facilitate accurate targeting of deep brain structures than 1.5 T or 3 T MRI.

4.5   Discussion

Accurate visualization of deep brain structures is important to improve our understanding of their anatomy, connectivity, and function, and for improved surgical targeting for DBS in movement and psychiatric disorders.

To date, targeting based on direct visualization of DBS targets with T2-weighted 1.5 T or 3 T MRI can be difficult. However, studies at ultra-high field showed good visibility of these structures on SW images based on T2* and phase contrast. Structures that have been identified at ultra-high field include: a separation between the STN and SN[2,43,56,146,193]; the lamina pallidi medialis and lamina pallidi incompleta within the GP[2,56]; a subdivision of the STN in two halves[128,146]; subdivisions of the SN possibly representing the SN pars reticulata and SN pars compacta[56,69,128]; substructures in the RN[2,69] including the medullary lamella[1,56], RN pars oralis[1], and RN pars caudalis[56]; and several regions in the thalamus[128] including the Vim[2,56], the pulvinar[56] and its anterior and medial boundaries[2], the boundary of the nucleus ventralis caudalis[2], the lateral and medial geniculate nucleus[56], the dorsomedial nucleus[56] and the dorsal nuclei group[56]. Furthermore, 7 T T2*-weighted and SW images have displayed improved CNR, SNR and resolution in the deep brain regions, compared to 1.5 T and 3 T images[43,110-113].

Based on a descriptive evaluation of different MR images, more and smaller structures can be identified on T2*-weighted, GE phase, SW images, and susceptibility and R2* maps than on T1 and T2-weighted images[1,2,56,110,113]. Although quantitative comparison between studies is difficult due to variations in scan protocols, the CNRs of deep brain structures on T2* and SW images and corresponding maps are generally higher than those of T2 and T1-weighted images[110,113]. For the SNR, the same trend can be seen, although T1-weighted images seem to have a higher SNR than SW images[110,113].

4.5.1   Perspectives

The improved visualization of the basal ganglia with ultra-high field MRI discussed here provides good perspectives for clinical practice. The clear delineation of DBS target structures and their possible subdivisions may aid in more accurate targeting, which may reduce negative side-effects and shorten surgery duration, or it may even allow surgery under general anesthesia. Furthermore, ultra-high field MRI also shows potential for more accurate diagnosis and monitoring of basal ganglia diseases due to, for example, improved identification of the SN pars compacta and SN pars

reticulata, which may in its turn facilitate improved patient-specific treatments.

In addition, ultra-high field MRI promises to be a versatile tool in clinically oriented research of the deep brain nuclei. It might help us to improve our current understanding of the functionality of the healthy basal ganglia and its disease processes with high resolution functional MRI and connectivity analyses.

4.5.2   Recommendations

When in the end considering the optimal scan protocol for visualizing the DBS targets for clinical purposes at ultra-high field, both image quality and practical requirements need to be taken into account. In terms of hardware, it is recommended to use a head coil with a high number of receive channels (i.e. 16 or higher). This has been shown to improve the SNR[52,224] which is also reflected from the studies described in Table 4.2. In terms of scan protocol, based on the described literature, we recommend to use a 3D multi-echo GE sequence with an isotropic resolution of 0.5 mm^3 and partial brain coverage. The 3D sequence facilitates small and isotropic voxel sizes, which ensures good resolution in every plane which is important for distinguishing the STN from the SN. From the multi-echo GE scan, both T2*-weighted and susceptibility-weighted images as well as T2* maps, R2* maps, and susceptibility maps can be computed, which were shown in the reviewed literature to display best basal ganglia visibility. Since the basal ganglia are located within the same axial oblique slab of approximately 4-5 cm thickness, we advise to shorten the scan time by covering only this part of the brain. If more time reduction is required, partial Fourier imaging, elliptical k-space coverage, or parallel imaging can be considered as well.

To support these guidelines, Figures 4.4 and 4.5 show examples of a T2*-weighted image and an R2* map, respectively, created with these recommendations. The images were obtained by scanning a healthy volunteer on a 7 T MRI scanner (Magnetom 7T, Siemens, Erlangen, Germany) at Scannexus (Maastricht, The Netherlands) using a 32-channel phased-array coil (Nova Medical, Wilmington, United States) with a multi-echo 3D GE sequence. Scan time was reduced to 12 minutes and 23 seconds by partial brain coverage and 75 % partial Fourier imaging (other scanning parameters can be found in Table 4.2 - line 47:48). On these 0.5 mm^3 isotropic

resolution images, the STN can be distinguished from the SN in the coronal plane, and the three laminae of the GP can be identified.
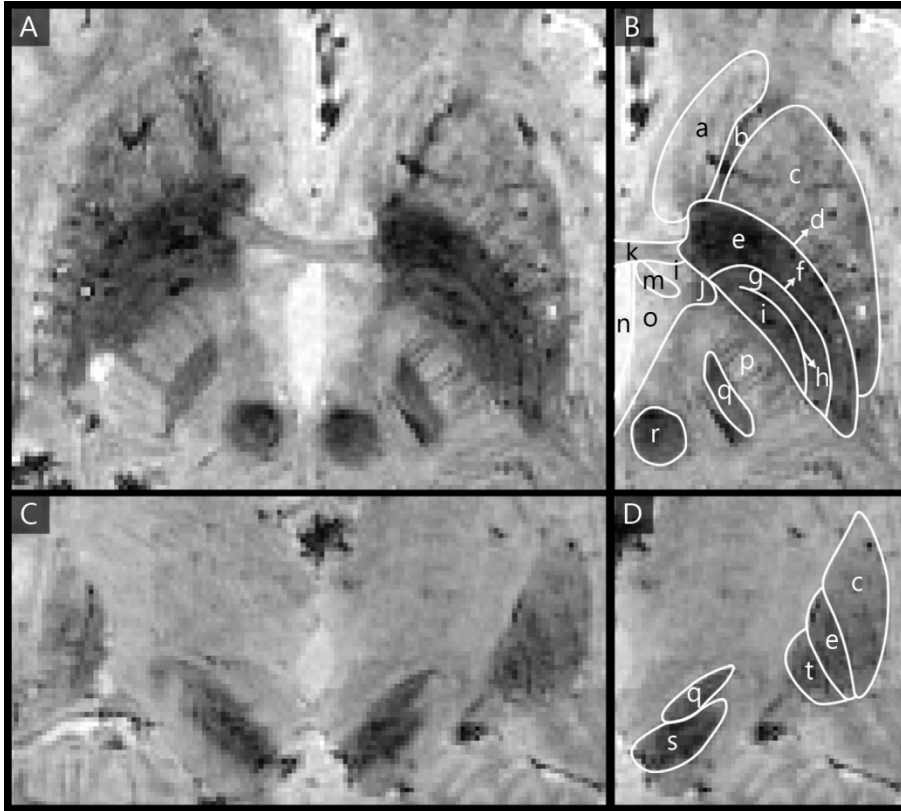

Figure 4.4: Ultra-high field (7 T) axial (A, B) and coronal (C, D) T2*-weighted images. Figures B and D show the anatomical structures that can be identified with the Schaltenbrand and Wahren atlas[194]. a = caudate nucleus. b = anterior limb of internal capsule. c = putamen. d = lamina pallidi lateralis. e = external globus pallidus. f = lamina pallidi medialis. g = pallidum mediale externum. h = lamina pallidi incompleta. i = pallidum mediale internum. j = inferior thalamic peduncle. k = anterior commissure. l = prothalamus. m = fornix. n = third ventricle. o = hypothalamus. p = posterior limb of internal capsule. q = subthalamic nucleus. r = red nucleus. s = substantia nigra. t = internal globus pallidus. (Courtesy D. Ivanov)
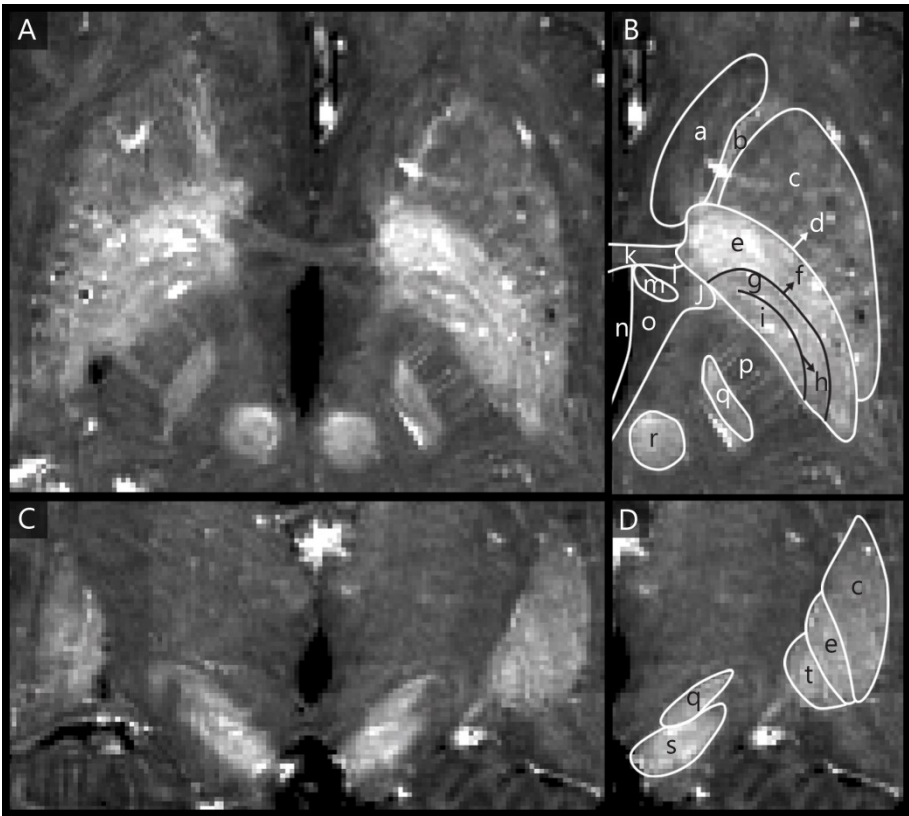
Figure 4.5: Ultra-high field (7 T) axial (A, B) and coronal (C, D) R2* maps. Figures B and D show the anatomical structures that can be identified with the Schaltenbrand and Wahren atlas[194]. a = caudate nucleus. b = anterior limb of internal capsule. c = putamen. d = lamina pallidi lateralis. e = external globus pallidus. f = lamina pallidi medialis. g = pallidum mediale externum. h = lamina pallidi incompleta. i = pallidum mediale internum. j = inferior thalamic peduncle. k = anterior commissure. l = prothalamus. m = fornix. n = third ventricle. o = hypothalamus. p = posterior limb of internal capsule. q = subthalamic nucleus. r = red nucleus. s = substantia nigra. t = internal globus pallidus. (Courtesy D. Ivanov)

When planning a DBS surgery, the MR images are often registered to X-ray computed tomography (CT) images, resulting in images that both display the stereotactic frame from the CT image as well as contrast within the brain. This registration may be more reliable however, if a whole brain MR image is available as an intermediate step. Abosch et al.[2] showed that it is already

61

possible to perform 1 mm^3 whole brain T1-weighted imaging in 3.5 minutes, which may be a good candidate for coregistration.

4.5.3 Limitations

Despite these promising results concerning accurate and high resolution visualization of the small deep brain (sub)structures, several issues still need to be addressed before they can be routinely employed in direct targeting for DBS.

Firstly, ultra-high field images have an increased risk of geometrical distortions compared to 1.5 T images. The severity of these distortions at 7 T in deep brain regions has been investigated in several studies. One study compared the coordinates of marker points in a phantom imaged with 1.5 T and 7 T MRI to their locations on CT images[50]. The maximum distortion in either x, y, or z-direction at 7 T was 1.6 mm, which was slightly larger than at 1.5 T (0.9 mm). Furthermore, the fewest distortions were observed in the center of the phantom. In another study the distortions in an anthropomorphic phantom between T2*-weighted 7 T MR and CT images were investigated, revealing a maximum deviation of 0.78 mm[43]. Finally, registration of 7 T T1 and T2-weighted images of the midbrain of PD patients to 1.5 T T1 and T2-weighted images showed that mainly rigid body transformations were required and that scaling and skew deformations were small[66]. Furthermore, the midbrain region, containing many DBS targets, required the least correction. Quantitative comparison showed that the distances of the T2-weighted images were significantly less than 1 mm suggesting that affine registration of T1 and T2-weighted 7 T images to CT images can already provide MR images with midbrain distortions comparable to those of 1.5 T images. These few studies suggest that at 7 T images can be acquired with distortions smaller than 1 mm in the deep brain areas.

Secondly, some of the mentioned imaging techniques pose additional challenges in the clinical context. Most studies were performed on young and healthy volunteers. In patients, movement during image acquisition can be less controlled counteracting the gain in SNR and spatial specificity obtained with ultra-high field. However, newer techniques, such as prospective motion correction might remedy this problem[135]. This approach monitors movement in the scanner with high accuracy and corrects the new

image acquisition adaptively according to the new head position. That is, even with large head movements – as observed in many patients – the resulting images are already coregistered and movement artifact free.

In addition, the availability of ultra-high field MRI scanners is currently limited. Firstly, the number of scanners that have been installed in the world is limited itself, which is inherent to its high cost in purchase and in operation. Secondly, due to the novel status of ultra-high field MRI, safety precautions regarding metallic objects are often more strict than on 3 T systems and the use of ultra-high field MRI is currently only allowed for research purposes.

Finally, direct targeting in DBS suffers from brain shift, intraoperative deformation of the brain compared to preoperative MR images due to difference in head position and cerebrospinal fluid loss. Without compensation for this, it will eventually still limit targeting accuracy. However, this effect is independent of the magnetic field strength and even the preoperative imaging modality.

4.6   Conclusion

Ultra-high field MRI can reliably and accurately display subdivisions within the basal ganglia and related structures, which especially benefits from T2* and phase-related contrasts. If the limitations concerning image distortions and the availability of the scanners are solved, these technical advances have the potential to improve accuracy of targeting in DBS surgery and the clinical outcome.

4.7   Acknowledgements

CHAPTER 5

QUANTITATIVE IMAGING

5.1 Abstract

Parkinson's disease is characterized by pathological changes in the basal ganglia, which are difficult to assess in vivo. However, MRI promises to assess aspects of tissue composition (e.g. iron concentration and myelination) and structure (e.g. lesions and atrophy) in vivo, by measurement of the tissue's absolute relaxation times or diffusion properties. These aspects might be relevant for diagnosis, disease monitoring, and treatment optimization.

In this study, ultra-high field MRI is employed to non-invasively investigate iron and myelin-related changes in the basal ganglia of Parkinson's disease patients.

Using 7 T MRI, quantitative T1, T2*, and mean diffusivity maps were obtained of five Parkinson's disease patients and nine age-matched control subjects. The relaxation times and mean diffusivity values of the caudate nucleus, nucleus accumbens, putamen, external and internal globus pallidus, subthalamic nucleus, and substantia nigra were then compared between patients and control subjects.

These maps revealed a decrease in the T1 value of the caudate nucleus, subthalamic nucleus, and substantia nigra, a decrease in the T2* value of the substantia nigra, and alterations in the mean diffusivity of the caudate nucleus, substantia nigra, and internal globus pallidus of Parkinson's disease patients compared to the controls.

This study shows that in addition to the known iron related pathology as reflected in the T2* value, macromolecular volume fractions and microstructure also play an important role in the pathophysiology of Parkinson's disease, as reflected in the T1 and diffusion values. Being able to quantify these changes in vivo with ultra-high field MRI may facilitate diagnosis, monitoring disease progression, and treatment optimization, and improve our understanding of the disease.

5

5.2 Introduction

Parkinson's disease (PD) is a progressive neurodegenerative disorder that is characterized by motor symptoms such as rest tremor, bradykinesia, rigidity, and postural imbalance. Its pathological process is characterized by the loss of dopamine producing neurons in the substantia nigra pars compacta[70] and dopamine depletion in the striatum[198]. In addition, intraneuronal lesions already occur in the presymptomatic phase in more deeply located brain areas[33]. The network activity of the basal ganglia, consisting of the subthalamic nucleus (STN), substantia nigra (SN), globus pallidus (GP), and striatum, is heavily affected by these pathological changes. A simplified model suggests that it leads to a reduced inhibition of the STN, internal GP, and SN pars reticulata, ultimately leading to a reduced cortical activation and slowing of movement[57,222].

Assessment of the pathological changes is sometimes performed histopathologically on post mortem tissue, for example to confirm the diagnosis of PD[64]. In vivo assessment of the structural properties of brain tissue, such as lesions, volumes, and atrophy, can in general be performed with MRI. Standard MRI signal intensity in a given voxel is also related to other tissue characteristics, such as iron and myelin concentrations. However, MR physics effects, such as choice of sequence parameters, quality of shimming, and RF coil transmit and receive profiles, can confound the direct biological interpretation of MR signal intensity. Quantitative MRI approaches, on the other hand, have the potential to provide in vivo insights into biochemical changes in the basal ganglia related to PD pathology, in addition to the structural changes already detectable with standard MRI approaches. Being able to assess these changes may provide insight into the progression of basal ganglia pathology by performing longitudinal studies monitoring the disease at multiple time points. Despite the known global brain changes related to the disease, quantitative 3 T MRI has so far mainly succeeded at identifying the iron-related pathology of the SN[17,20,145,178]. Nevertheless, we know from histopathological studies that the disease pathology is more widespread.

Ultra-high field (7 T and higher) MRI of the brain provides higher resolution, signal-to-noise ratios, and contrast-to-noise ratios compared to 1.5 T and 3 T MRI[67,215]. This reflects its potential increased sensitivity to detect pathological changes that occur in the basal ganglia of PD patients. In

this study, we explored quantitative MRI changes in T1 and T2* relaxation times and the mean diffusivity of the caudate nucleus, nucleus accumbens, putamen, external and internal GP, STN, and SN of PD patients compared to healthy controls. The results confirm changes in the T2* relaxation time of the SN and additionally reveal changes in T1 relaxation times and mean diffusivity that were previously undetected.

5.3 Methods

5.3.1 Subjects

Five patients with idiopathic PD and nine age-matched control subjects (ages 53 – 70, two females) were included in this study. The characteristics of the patients are shown in Table 5.1. Exclusion criteria were claustrophobia and contra-indications for 7 T MRI such as pacemakers and metallic implants. This study was approved by the local Medical Ethics Committee at Maastricht University Medical Center (see Appendix A) and written informed consent was obtained from each subject.

Table 5.1: Patient characteristics. UPDRS II and UPDRS III are scored while on/off medication respectively.

Patient	Gender	Age (y)	Disease duration (y)	UPDRS I	UPDRS II	UPDRS III	H&Y score
1	F	66	16	2	7/13.5	12/25	3
2	M	73	5	2	9.5/11	32/39	2.5
3	M	71	10	3	16/18	18.5/33.5	3
4	M	65	16	4	10/15	6/34.5	3
5	F	54	11	1	17/17.5	43.5/55	2.5

F = Female. H&Y = Hoehn and Yahr. M = Male. UPDRS = Unified Parkinson's Disease Rating Scale. y = years.

5.3.2 Scanning protocol

Subjects were scanned on a 7 T MRI scanner (Magnetom 7T Siemens, Erlangen, Germany), equipped with SC72 gradients capable of 70 mT/m and a 200 T/m/s slew rate using a 32-element head array coil (Nova Medical, Inc, Burlington, MA, USA). Dielectric pads[202] were applied if possible (in seven control subjects and two patients), to enhance the signal in the temporal brain regions. The scan protocol consisted of a) a whole brain MP2RAGE

(Magnetization Prepared 2 Rapid Acquisition Gradient Echoes)[144] scan with two inversion times of 900 ms and 2750 ms resulting in a T1-weighted image and a quantitative T1 map[144], b) an axial oblique gradient recalled echo (GRE) scan of 4.0 cm thickness centered around the subthalamic nuclei with four echo times (TE) allowing to determine quantitative T2* values, and c) a diffusion-weighted scan along 60 directions with a b-value of 2000 s/mm^{2} with six b0-volumes and an additional six b0-volumes recorded with opposite phase encoding direction. Details of the scan protocols can be found in Table 5.2. The T2* maps were generated from the GRE data with four echo times by fitting a monoexponential function using an in-house C++ routine. Mean diffusivity maps were computed from the diffusion-weighted images with FSL[102] after correction for susceptibility, eddy currents, and motion with FSL's eddy and topup algorithms[9].

Table 5.2: Details of the scan protocol.

Weighting	Sequence	TE (ms)	TR (ms)	Flip angle (°)	Resolution (mm^3) (x × y × z)	Acquisition time (min:sec)
T1	MP2RAGE	2.47	5000	5 and 3	0.7 × 0.7 × 0.7	8:02
T2*	GRE	2.65, 7.37, 13.10, 21.11	34	11	0.5 × 0.5 × 0.5	8:33
Diffusion	EPI	60.6	7000	90	1.5 × 1.5 × 1.5	8:17

EPI = Echo Planar Imaging. GRE = Gradient recalled echo. MP2RAGE = Magnetization prepared 2 rapid acquisition gradient echoes. TE = Echo time. TR = Repetition time.

5.3.3 Image analysis

The left and right external and internal GP, STN, and SN were manually delineated on the longest echo time GRE image (TE = 21.11 ms), and the left and right putamen, caudate nucleus, and nucleus accumbens were manually delineated on the T1-weighted image using ITK-snap[233]. This ensured that each structure was delineated on the image type on which its borders could be most accurately delineated. One observer segmented the caudate nucleus and nucleus accumbens and another observer delineated the internal and external GP, STN, SN, and putamen. Both observers were blinded to whether the images belonged to patients or controls. The GRE image and its segmentations were then registered to the T1 and diffusion spaces and the T1 image and its segmentations were registered to the GRE and diffusion spaces using a rigid-body transformation with FSL's FLIRT[101]. This resulted

in the left and right segmentations of all six basal ganglia structures being available in the three native image spaces. These masks were used to compute the average T1, T2*, and mean diffusivity values of each segmentation.

A two-sided Mann-Whitney U-test was performed to assess differences in T1, T2*, and mean diffusivity values between patients and controls in the internal and external GP, STN, SN, putamen, caudate nucleus and nucleus accumbens. The distributions were considered to be significantly different if the p-value was smaller than 0.05.

5.4 Results

The T1 and T2* values distinguished the basal ganglia structures from each other and from their surroundings, as can be seen from the quantitative maps (Figure 5.1).
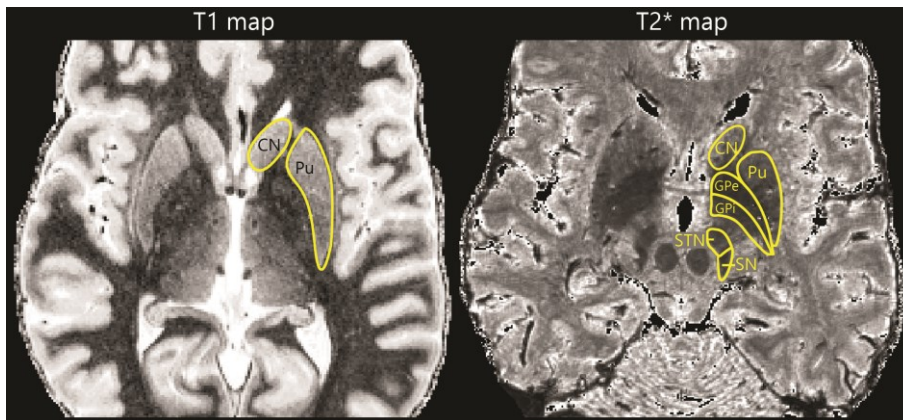
Figure 5.1: Examples of a T1 and a T2 map. The axial slices show the caudate nucleus (CN), putamen (Pu), external and internal globus pallidus (GPe and GPi), subthalamic nucleus (STN), and substantia nigra (SN).*

The mean T1 and T2* relaxation times and mean diffusivity within each of the segmented basal ganglia structures, averaged over the patients and the control subjects separately, are shown in Figure 5.2. The absolute averaged T1 and T2* relaxation times can be found in Table 5.3.

Figure 5.2: Bar plots of the T1 and T2* values and the mean diffusivity in Parkinson's disease patients and controls in the basa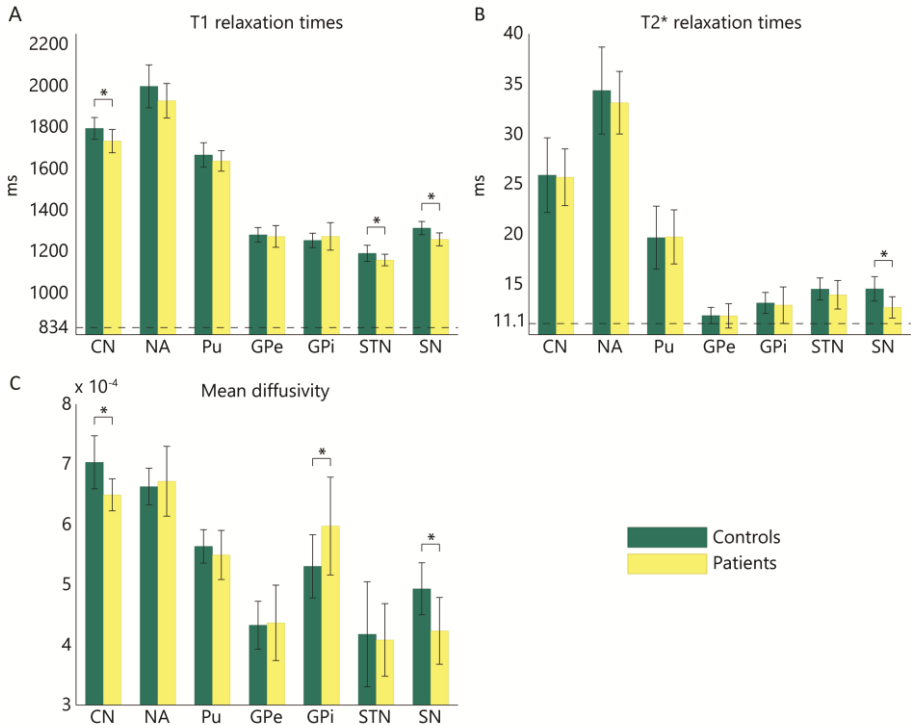l ganglia. The error bars denote the standard deviation across individuals. Statistically significant (p < 0.05) differences between patients and controls are marked with an *. The dotted lines indicate estimates of the lower boundaries of physiologically realistic brain T1 and T2* values at 7 T.

Table 5.3: Average T1 and T2* values at 7 T of the basal ganglia of the Parkinson's disease patients and controls.

Nucleus	T1 value (ms)		T2* value (ms)	
	Controls	Patients	Controls	Patients
Caudate nucleus	1794	1733	25.90	25.69
Nucleus accumbens	1997	1927	34.34	33.13
Putamen	1666	1637	19.67	19.75
External globus pallidus	1281	1273	11.90	11.87
Internal globus pallidus	1254	1273	13.16	12.94
Subthalamic nucleus	1192	1160	14.55	13.98
Substantia nigra	1314	1259	14.56	12.72

The striatum (including the caudate nucleus, putamen and nucleus accumbens) had on average longer T1 and T2* relaxation times than the internal and external GP, STN, and SN. The quantitative values of several structures differed significantly between patients and controls. The SN, which is known to progressively degenerate in patients with PD, had shorter T1 and T2* relaxation times, and a lower mean diffusivity in PD patients. Additionally, the STN, one of the targets for deep brain stimulation for PD, had a shorter T2* relaxation time in patients. The caudate nucleus also had altered values in PD patients with a shorter T1 relaxation time and a higher mean diffusivity. In the globus pallidus, the only statistically significant difference was found in the mean diffusivity of the internal GP, which was higher in PD patients.

Further inspection of the nuclei revealed that in both patients and controls, the inferior and anterior regions of the SN had shorter T1 and T2* relaxation times than the rest of the SN (Figure 5.3.). This large range of T1 and T2* relaxation times within the SN is also reflected in their 90 % intervals: 90 % of the T1 values within the SN are between 1085 and 1527 ms and 90 % of the T2* values are between 9.1 and 20.4 ms. Also, when following the caudate nucleus and putamen from their most posterior tips towards the anteriorly located nucleus accumbens, a gradient of increasing T1 relaxation time (90 % interval of caudate nucleus: 1534-2233 ms, 90 % interval of the putamen: 1412-1951 ms) and for the putamen also increasing T2* relaxation time (90 % interval: 12.1-31.1 ms) was observed. In line with this, the nucleus accumbens itself also displayed longer T1 and T2* relaxation times than the rest of the striatum (Figure 5.2).

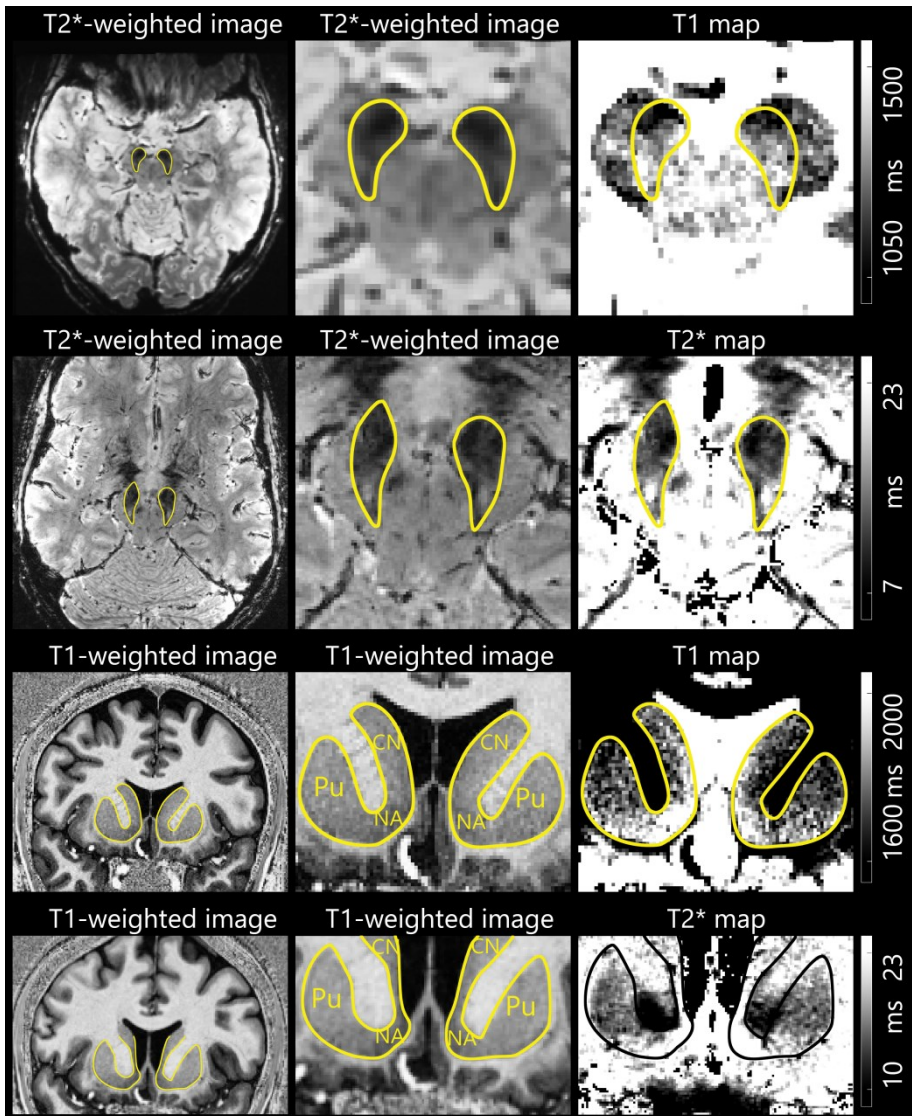*Figure 5.3: Inhomogeneities of the T1 and T2* values within the substantia nigra (row 1 and 2) and striatum (row 3 and 4). The quantitative maps (third column), have been windowed such that the inhomogeneities can be easily assessed.*

5.5 Discussion

Parkinson's disease affects the whole network of the basal ganglia. It is characterized by the degeneration of dopamine producing cells in the

substantia nigra pars compacta[70], dopamine depletion of the striatum[198], and increased iron levels[80]. This study demonstrates that the caudate nucleus, internal GP, STN, and SN of PD patients indeed display T1 and/or T2* relaxation times and diffusion properties that are significantly different from those in healthy age-matched control subjects. This reflects underlying changes in structure and biochemical composition of these anatomical structures in PD patients.

In contrast to regular T1-weighted, T2-weighted or T2*-weighted MRI, quantitative MRI directly displays the tissue's actual relaxation times T1, T2, or T2*. The weighted images, on the other hand, are confounded by MRI sequence parameter choices, and the image intensity values are usually not comparable between sites, subjects, and runs. Thus, longitudinal and/or multi-center center studies going beyond local contrast, lesion detection, and atrophy, are difficult to perform with standard MRI. Quantitative MRI approaches, however, provide, for a given magnetic field strength[190,229], absolute markers of the anatomical microstructure of the tissue.

Variations in quantitative MRI signal have mainly been attributed to variations in the concentrations of iron and macromolecules, such as myelin and neuromelanin, and to the composition and orientation of myelin relative to the main magnetic field[26,190,200,229]. The relaxation rates R1 and R2*, defined as 1/T1 and 1/T2* respectively, have been proposed to increase linearly with these concentrations[190,229]. Thus, a shorter T1 or T2* indicate increased concentrations of macromolecules and iron. Although both contrasts are influenced by both compounds, T1 is especially sensitive to macromolecules and T2* to iron. Using these linear relations[190,229], with reported brain iron values up to approximately 220 μg/g wet weight in the external GP[87] and an estimated maximum of a macromolecular mass fraction of 0.5, the lower limits for physiologically realistic brain T1 and T2* values at 7 T become approximately 834 ms and 11.1 ms, respectively (indicated with the dotted lines in Figures 5.2 A and B). In addition, the mean diffusivity represents the structural density or organization of the tissue and is derived from the diffusion properties of water molecules. The more freely they can diffuse in any direction, indicating fewer boundaries within or between cells, the larger the mean diffusivity will be.

In contrast to regular T1, or T2*-weighted images, the quantitative images can be used for correlating disease progression and for comparing between

subjects. The decreased T2* relaxation time that we observed in the SN of PD patients compared to healthy controls is in line with previous investigations into the T2* and its equivalent R2* at 3 T MRI, showing that T2* is reduced in (parts of) the SN - often the pars compacta - of PD patients[17,20,65,145,178]. It is generally assumed that this is caused by an increase in iron concentration, known to occur in the SN of PD patients[80]. Indeed, with the proposed linear relationships between the relaxation times and iron and macromolecule concentrations[190,229], the decreased T2* corresponds to an increased iron concentration in the SN of patients from 155 ppm to 186 ppm wet weight. Additionally, it is related to an increase in the macromolecular mass fraction of the SN from 0.26 in controls to 0.27 in patients. In the previous quantitative MRI studies, the SN was often manually subdivided into a pars compacta and pars reticulata, based on histological or anatomical studies[17,65,145]. Here, we chose not to do so because this indirect approach cannot account for subject-specific variations in SN anatomy[62] and may lead to wrong conclusions. We did, however, observe shorter T2* relaxation times in the anterior inferior region of the SN than in the posterior superior part, in both patients and controls, indicating that iron is not homogeneously distributed within the SN. One might argue that this difference indeed represents the SN pars compacta and the SN pars reticulata. However, this is not likely since the observed anterior-posterior divisions do not align with the expected medial and lateral locations of the SN pars compacta and SN pars reticulata.

In addition to the T2* changes, we found statistically significant shorter T1 relaxation times in the caudate nucleus, STN, and SN of PD patients compared to controls. This indicates that the macromolecule concentration or composition in these structures is also altered in PD patients. According to the previously discussed relationships[190,229], this corresponds to an increased macromolecular mass fraction of up to 6.9 % in the caudate nucleus of patients. In addition, the caudate nucleus and SN of PD patients had a significantly lower mean diffusivity, which also indicates microstructural changes in these structures. In relation to this, two of the most striking changes in the striatum of parkinsonian brains have previously been demonstrated to be dopamine depletion and loss of dendritic spines[97,198,217]. The latter of these, the change in cellular architecture, might explain the altered mean diffusivity in the caudate nucleus.

Interestingly, in the putamen, another component of the striatum, these observed differences were not statistically significant.

In both patients and controls, the relaxation times within the striatum displayed a clear distribution pattern. The nucleus accumbens, a region in the ventral transition between the putamen and the caudate nucleus involved in motivation and reward, has markedly higher T2* and T1 relaxation times than the putamen and caudate nucleus. Although the borders between the three structures are not well defined on MRI, this finding confirms their distinctly different anatomical makeup.

The T1 and T2* values that we found for the basal ganglia structures of the healthy control subjects are in the same range as previously reported values at 7 T[55,56,144,190,226,229]. Studies about the quantitative MRI values in PD patients, on the other hand, are usually performed at 3 T and mainly focus on T2, T2* or susceptibility-weighted contrast[17,20,65,145,178], which is also related to brain iron content. However, one study at 3 T also demonstrated a decrease in T1 in part of the SN[20]. At 7 T MRI, we were able to show T1 value differences not only in the SN, but also in the caudate nucleus and STN between patients and controls. This might be due to increased sensitivity to T1 value changes at ultra-high field, caused by the general increase of tissue T1 values with increasing field strength[190]. Other studies also found a reduced fractional anisotropy in the SN of PD patients[178,214]. Although the fractional anisotropy is related to the mean diffusivity, we did not find any statistically significant differences between the fractional anisotropy values of the basal ganglia in patients versus controls, and results were not reported. This might be due to the small number of patients involved in this study.

However, we would like to mention that the current study has the following limitations: first, the T2* maps were obtained from 4.0 cm axial GRE slabs acquired through the basal ganglia. In some subjects, this lead to the caudate nucleus, that was completely included in the T1 and mean diffusivity maps, being only partly included in the T2* maps. However, since on average 80 % of the caudate nucleus volume was still included, we do not expect alterations in the measured average T2* value in this structure. Second, it would be interesting to investigate whether the altered T1, T2*, and mean diffusivity are related to the disease stage, just like the increased iron levels[80] and to some extent melanin containing neurons in the SN pars compacta[120]. Although, the number of patients included in this study is too low to reliably

assess this hypothesis, an analysis of the trends showed that for all nuclei except the nucleus accumbens, the T1 value decreased with increasing Unified Parkinson's Disease Rating Scale (UPDRS) II and UPDRS III on and off scores and that the T2* value decreased with UPDRS II and increased with UPDRS III.

Parkinson's disease is a network disease. This could explain that more than one basal ganglia structure is affected. This is also corroborated by the fact that electrical stimulation of the STN as well as of the internal GP, two anatomically distinct structures, results in improved motor outcomes in PD patients[165]. Typically, the SN is designated the instigator of these symptoms. This study confirms that other basal ganglia structures are not only affected because they receive and pass on pathological signals, but also actually display altered microstructural anatomical properties themselves. Being able to quantify these changes may provide an objective tool for monitoring disease progression. Whether these changes occur as a consequence of the progressive degeneration of the SN, or whether they are simultaneous or even prior instigators of the disease is still an open question. Longitudinal studies into the alterations of the quantitative T1, T2*, and mean diffusivity values in the basal ganglia of PD patients might shed a light on this.

5.6 Acknowledgments

CHAPTER 6

PARCELLATION OF THE SUBTHALAMIC NUCLEUS

6.1 Abstract

Deep brain stimulation of the subthalamic nucleus (STN) is a widely performed surgical treatment for patients with Parkinson's disease. The goal of the surgery is to place an electrode centered in the motor region of the STN while lowering the effects of electrical stimulation on the non-motor regions. However, distinguishing the motor region from the neighboring associative and limbic areas in individual patients using imaging modalities was until recently difficult to obtain in vivo. Here, using ultra-high field MR imaging, we have performed a dissection of the subdivisions of the STN of individual Parkinson's disease patients.

We have acquired 7 T diffusion-weighted images of seventeen patients with Parkinson's disease scheduled for deep brain stimulation surgery. Using a structural connectivity-based parcellation protocol, the STN's connections to the motor, limbic, and associative cortical areas were used to map the individual subdivisions of the nucleus.

A reproducible patient-specific parcellation of the STN into a posterolateral motor and gradually overlapping central associative area was found in all STNs, taking up on average 55.3 % and 55.6 % of the total nucleus volume. The limbic area was found in the anteromedial part of the nucleus.

Our results suggest that 7 T MR imaging may facilitate individualized and highly specific planning of deep brain stimulation surgery of the STN.

6

6.2   Introduction

Deep brain stimulation (DBS) of the subthalamic nucleus (STN) is a widely performed surgical treatment for patients with Parkinson's disease (PD)[61,196]. There are two determining factors for a successful outcome: patient selection[169] and accuracy of targeting[169,170,219]. Concerning the latter, the STN is organized into three main functional territories: motor, associative, and limbic. The goal of DBS is to preferentially stimulate the motor part of the STN to obtain optimal motor outcome (Figure 6.1). Targeting is currently performed with 1.5 T or 3 T MRI, usually combined with intraoperative micro-electrode recordings and patient testing to distinguish the motor part from the neighboring associative and limbic areas[234]. In this context, behavioral side-effects have often been linked to undesired stimulation of the non-motor territories of the STN[140,167].

Figure 6.1: The goal of deep brain stimulation for Parkinson's disease is to stimulate the motor part of the subthalamic nucleus (blue) and to avoid stimulation of the non-motor areas (green and red). Figure adapted with permission from Temel et al.[204].

Although the debate is still ongoing[8,114,122], classical neuroanatomical studies in animal models place the motor territory in the posterolateral portion of the STN and the associative and limbic regions more anteromedially[175,204]. Using a 3 T clinical MRI scanner, this anatomical concept was demonstrated in healthy subjects[121]. Compared to 3 T MRI, ultra-high field (7 T and higher) MRI technology promises to improve the imaging contrast, resolution, and signal-to-noise ratio at clinically feasible scan times[2,43,128,179], which allows for a detailed visualization of the patients' STN anatomy and its connections[2,128].

6

In this study, we have acquired 7 T diffusion-weighted images of patients with PD scheduled for deep brain stimulation surgery. Using a previously established protocol applied on thalamic parcellation[23], we have performed a patient-specific dissection of the subdivisions of the STN demonstrating a clear topographical organization of major functional territories that may allow for individualized surgical planning.

6.3 Materials and methods

6.3.1 Subjects

We have included seventeen patients with idiopathic PD (five female, ages: 48-74 years, mean age: 62 years, mean Unified Parkinson's Disease Rating Scale (UPDRS) III score on/off medication: 18.3/37.5) who were referred for DBS surgery at the University of Minnesota (Minneapolis, MN, USA) and Maastricht University Medical Center (Maastricht, Netherlands). The inclusion criteria for surgery were clinical findings consistent with idiopathic PD, severe response fluctuations and/or dyskinesias (despite optimal pharmacological treatment) and good initial L-dopa response. The exclusion criteria were significant atrophy, focal brain abnormalities on MRI, a score of less than 24 on the Mini-Mental State Examination, psychosis, and general contraindications for surgery such as severe hypertension or blood coagulation disorders. Subjects with claustrophobia or other contra-indications for 7 T MRI (such as pacemakers and metallic implants) were also excluded from the study. This study was approved by the Institutional Review Board at the University of Minnesota and the Local Medical Ethics Committee at Maastricht University Medical Center (Appendix A).

6.3.2 Scanning protocol

Patients were scanned on a 7 T MRI scanner (Magnetom 7T Siemens, Erlangen, Germany), available at both institutions, equipped with SC72 gradients capable of 70 mT/m and a 200 T/m/s slew rate using a 32-element head array coil (Nova Medical, Inc, Burlington, MA, USA), while taking their usual antiparkinsonian medication. Dielectric pads[202] were applied, when possible (n = 11), to enhance signal in the temporal regions. The scan protocol consisted of a) a T1-weighted whole brain scan with an inversion

time of 1500 ms, b) a T2-weighted coronal slab through the STNs, and c) a whole brain diffusion-weighted scan along 50 directions with a b-value of 1500 s/mm^2 and four additional b0-volumes, performed twice with anterior-posterior and posterior-anterior phase encoding directions. Details of the scan protocol can be found in Table 6.1. Five patients were scanned with a slightly different protocol, including a diffusion-weighted scan with a b-value of 2000 s/mm^2, 60 directions, and twelve b0-volumes of which six with opposite phase encoding directions, and a T2*-weighted 0.5 mm isotropic gradient recalled echo (GRE) scan. These small protocol differences did not significantly alter the individual findings.

Table 6.1: Scan sequence parameters.

Weighting	Sequence	TE (ms)	TR (ms)	Flip angle (°)	Matrix size	Resolution (mm^3)	Acquisition time (min)
T1	3D GR/IR	3.5	3100	5	312 × 384 × 256	0.6 × 0.6 × 0.6	6.5
T2	2D SE	58	± 8000	150	512 × 26 × 512	0.39 × 1.0 × 0.39	6.5
Diffusion	2D EP	55.6	± 5000	90	136 × 136 × 66	1.5 × 1.5 × 1.5	2 × 4.5

EP = Echo planar. GR/IR = Gradient-recalled echo/inversion recovery. SE = Spin echo. TE = Echo time. TR = Repetition time.

6.3.3   Image analysis

The image analysis methods to compute the STN parcellations are described in Sections 6.3.3.1-6.3.3.3 and are summarized in a flowchart in Figure 6.2.

6.3.3.1   Cortical masks

A 1 mm^3 isotropic T1-weighted reference brain, developed by the Montreal Neurological Institute (MNI)[82], was manually divided into four cortical areas: the motor, associative, and limbic cortical areas, and the remaining cortex (see Figure 6.3 A and B). The motor area included the primary motor, supplementary motor, and pre-motor cortex. On the MNI brain, this was defined as the cortical area bounded posteriorly by the central sulcus, medially by the cingulate sulcus, laterally by the border between the precentral gyrus and frontal operculum gyrus, and anteriorly as defined by the human motor area template[147]. The limbic area was made symmetrical across hemispheres and included the orbitofrontal and entorhinal cortices based on the definition by Mai et al.[136], and the anterior cingulate cortex,
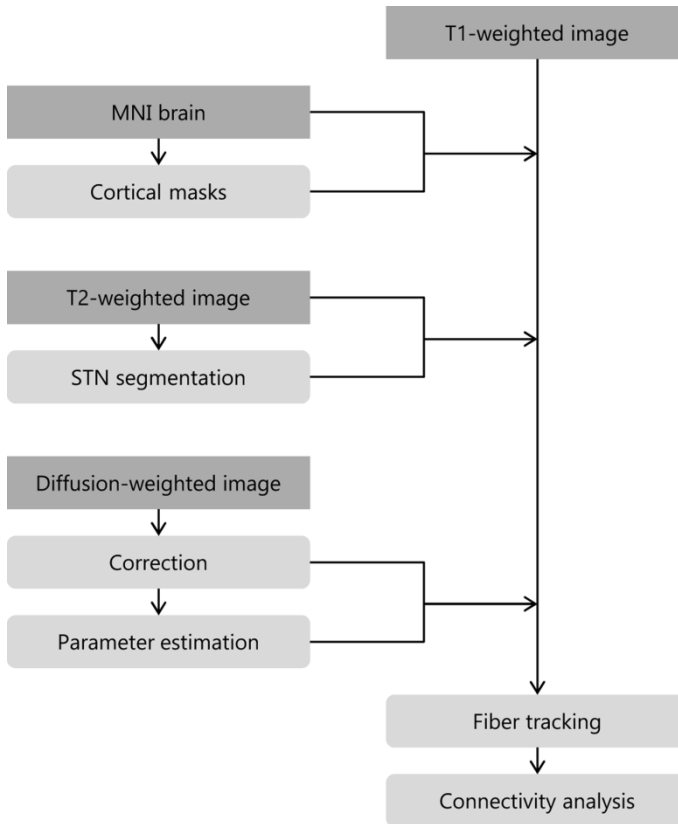
Figure 6.2: Image analysis pipeline, consisting of the definition of the cortical masks on the Montreal Neurological Institute (MNI) brain[82], the segmentation of the subthalamic nuclei (STNs) on the T2-weighted image, and the tractography and connectivity analysis steps in T1-space.

amygdala, and hippocampus as adopted from the Harvard-Oxford atlas[60]. The associative area was defined as the cortical region bounded by the limbic cortical area anteriorly and the motor cortical area posteriorly. The fourth cortical area consisted of the remaining cortex, including the occipital lobe, parietal lobe, and part of the temporal lobe. The MNI brain and cortical masks were non-linearly registered to each patient's T1-image with FSL's FNIRT[10] and masked with gray matter segmentations of the T1-images produced with FSL's FAST[235] that were dilated with one voxel. This resulted in four gray matter cortical masks in each subject's native space.
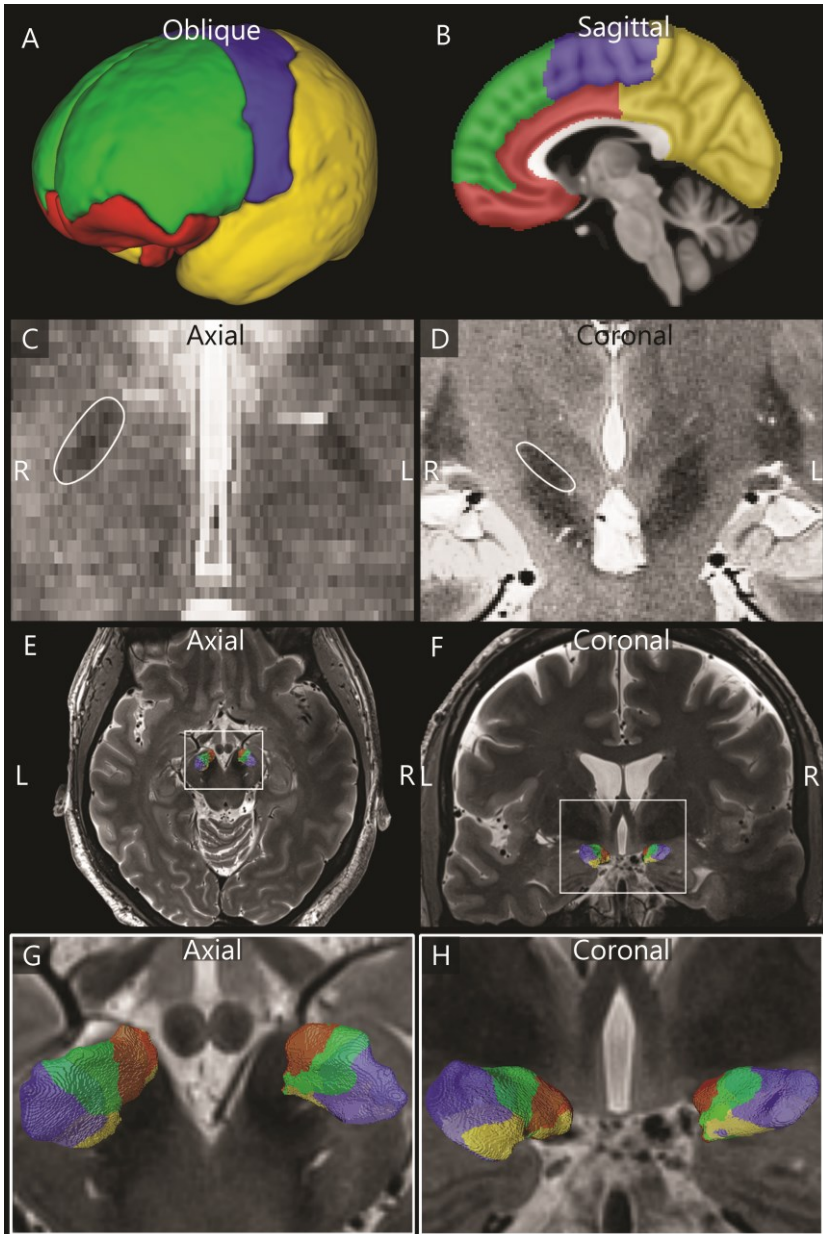
Figure 6.3: The STN is parcellated based on its connections to the limbic, associative, motor, and remaining cortical areas. A-B) Division of the cortex into limbic (red), associative (green), motor (blue) and remaining (yellow) cortical areas. C-D) Visualization of the hypointense STNs in the axial (C) and coronal (D) planes. The right STN is delineated in white. E-H) Example of the parcellation of the STNs of one subject in axial (E,G) and coronal (F,H) views.

6

6.3.3.2   STN segmentations

For each subject, the STNs, which were visible as a hypointense structure superior to the substantia nigra in the coronal plane (Figure 6.3 D), were manually segmented on the T2-weighted images with Amira software (FEI, Hillsboro, OR, USA). The good intra-observer agreement index for segmentations of the basal ganglia based on similar images was demonstrated previously[128]. Along with the T2-weighted images, these binary segmentations were rigidly coregistered to each subject's T1-space with FSL's FLIRT, using sinc interpolation with a Hanning window[101]. These segmentations were then binarized again using a threshold of 0.45, which was empirically determined to least affect the volumes of the segmentations.

6.3.3.3   Diffusion analysis

After correction for motion and for susceptibility and eddy current distortions with FSL's eddy and topup algorithms[9], diffusion parameters were estimated using a three-fiber model with FSL's bedpostx[22]. Probabilistic fiber tracking with FSL's probtrackx2 was performed in T1-space, using a rigid transformation matrix, with the STN as a seed region and 500 samples per voxel (equivalent to 2315 samples per mm^3). Other fiber tracking settings included FSL's default curvature threshold of 0.2, maximum number of steps per sample of 2000, step length of 0.5 mm, subsidiary fiber volume threshold of 0.01, and termination of pathways that looped back on themselves. Using the ipsilateral cortex as inclusion region and the contralateral hemisphere as exclusion region, the percentage of tracks reaching either of the four ipsilateral cortical regions was computed for each voxel in the STN (Figure 6.3 E-H). A voxel was considered to be connected to that cortical area if at least 25 % of its probabilistic tracks connected the two, allowing for one voxel to be connected to more than one cortical area. This threshold was preferred over a winner-takes-all approach, because with a diffusion resolution of 1.5 mm isotropic, one voxel might contain several white matter tracks.

6.3.4   Validation

As a first step to validate our methods, we have used our protocol to map the known thalamic connections to the prefrontal-temporal, motor,

somatosensory, and parieto-occipital cortical areas. The results were compared to the thalamic connectivity based segmentation as demonstrated by Behrens et al.[23].

Second, in five STNs, the classification of the motor STN region was compared to the position of the active contact, by registering the postoperative X-ray computed tomography (CT) image showing the DBS lead, to our anatomical model. These contacts had been confirmed to stimulate the motor area of the STN, through intraoperative micro-electrode recording, intraoperative testing, and postoperative surveys, and were confirmed by improved motor performance of the patients.

6.3.5   *Reproducibility*

In order to assess the reproducibility, a 26 years old healthy male subject was scanned four times on three different days with the same scan protocol as described in Section 6.3.2 and Table 6.1. The four datasets were then analyzed as described above and the reproducibility of the outcome results was assessed.

6.3.6   *Statistical analysis*

Volumes of the STN and of its subdivisions are presented as means and standard deviations. Statistical comparisons were made using the related samples Wilcoxon signed rank test to evaluate right and left differences in STN volumes. A p-value < 0.05 was considered statistically significant.

6.4   Results

6.4.1   *Validation*

The first step of this study was to validate our analysis approach by reproducing the results of Behrens et al.[23] (Figure 6.4). This demonstrates that our methods allow us to create detailed parcellations of subcortical structures of individual PD patients.
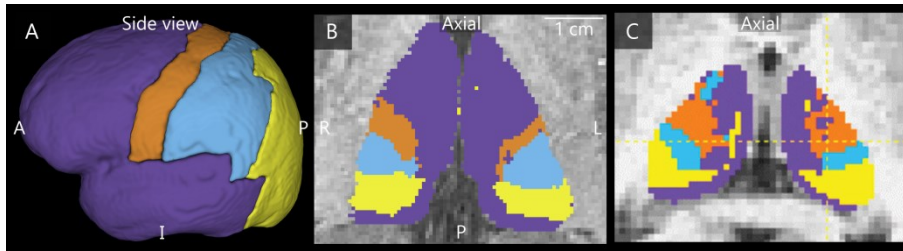
Figure 6.4: Connectivity mapping of the thalamus. A) Manual segmentation of the cortex into prefrontal and temporal (purple), motor (orange), somatosensory (blue), and parieto-occipital (yellow) cortical areas as defined by Behrens et al.[23]. B) A patient-specific thalamic subdivision in one of our subjects. C) Thalamic subdivision as demonstrated by Behrens et al.[23]. (Adopted from Behrens et al.[23])

6.4.2   STN segmentation

The mean volume of the segmented STNs in their native space across all patients was 125.4 mm^3 ($\pm$ 22.9 mm^3). The biconvex structure was consistently oriented along an axis that ran from its superior posterolateral to its inferior anteromedial apex; the most anterior apex of the STN was also located at its most medial and most inferior border and its most posterior apex also formed its most lateral and most posterior ends. No significant differences were found between the volumes of the left and right STNs (p = 0.52).

6.4.3   STN parcellation

A consistent functional organization was observed in all STNs, with the zones arranged mainly along its longest axis, as was visually assessed from 3D displays of the STNs. In all 34 STNs, the superior posterolateral division of the STN showed strong connections to the motor cortical areas, and a partly overlapping zone located centrally along the STN's longest axis was mainly connected to associative cortical areas. Connections to the limbic cortical brain areas could be identified in 30 of 34 STNs, originating from STN territories with varying volumes, but in all 30 cases located at the inferior anteromedial section of the STN. This ordering of the motor, associative, and limbic zones of the STN along the posterolateral-anteromedial axis is illustrated in three representative examples (Figure 6.5). Connections of the STN to the remaining cortical regions were found as well,

although they did not have a consistent origin within the STN and these zones were relatively small.
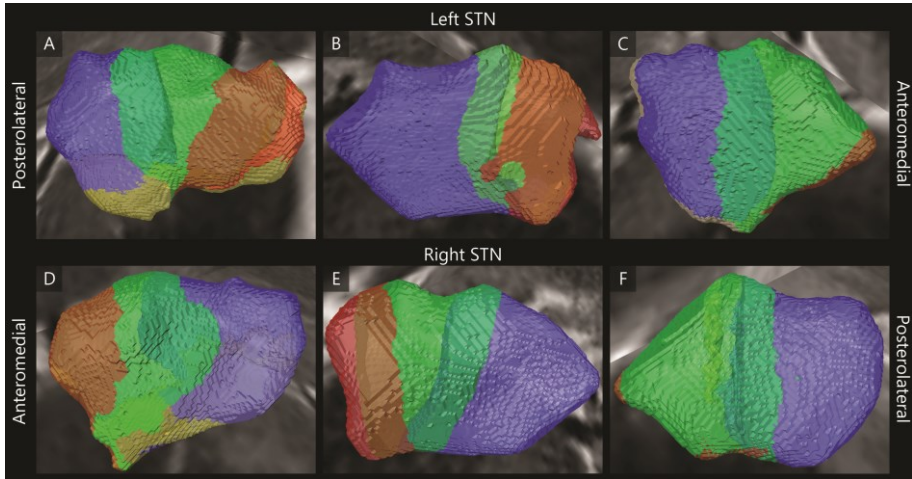

Figure 6.5: Examples of the subdivisions of the left (A-C) and right (D-F) subthalamic nuclei of three subjects into a limbic (red), associative (green), and motor (blue) zone. Intermediate colors show overlap between the motor and associative zones (light blue) and between the associative and limbic zones (brown).

6.4.4   Volumes of the STN's functional zones

Figure 6.6 illustrates the variations in the relative volumes, defined by a relative connectivity of at least 25 %, of each zone between patients and hemispheres. The average volumes, per region, were 55.3 % (± 14.0 %) for the motor area, 55.6 % (± 15.9 %) for the associative area, 20.3 % (± 16.3 %) for the limbic area, and 12.5 % (± 16.2 %) for STN volumes connected to other cortical areas. This corresponds to volumes of 68.7 mm^3 (± 19.7 mm^3), 70.6 mm^3 (± 26.7 mm^3), 25.8 mm^3 (± 20.8 mm^3), and 16.1 mm^3 (± 21.0 mm^3) for the motor, associative, limbic, and other cortical areas, respectively. Note that the percentages add up to more than 100 %, because of overlap (as described in Section 6.3.3.3), with 17.01 % (± 8.85 %) of the STN volume assigned to both motor and associative functions and 15.56 % (± 13.15) to both associative and limbic functions, corresponding to average volumes of 21.0 mm^3 and 19.3 mm^3 respectively.
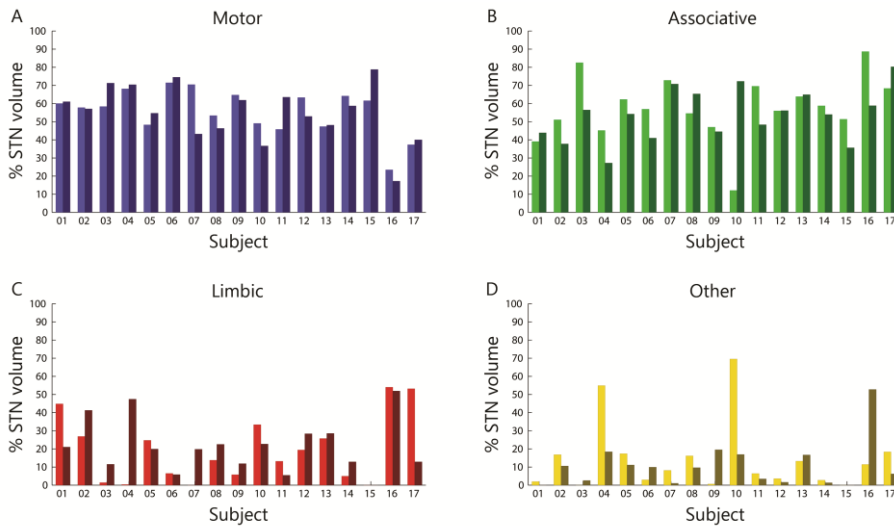
Figure 6.6: Relative volumes of each functional zone compared to the total STN volume within the left and right STN (left and right bar) of each subject.

6.4.5   Reproducibility

To examine the reliability of our findings, the same analysis was applied to four independently repeated scan sessions of a single healthy subject. Although there were some intra-subject variations of both the total STN volumes as well as the relative volumes of the subdivisions, they were consistently smaller than the inter-subject standard deviations among our patient population (Table 6.2 and Figure 6.7). This example suggests adequate reproducibility of the methods and sensitivity to actual patient-specific variations.

Table 6.2: *Standard deviations of the STN volumes (mm³) and the relative volumes of their functional zones (%).*

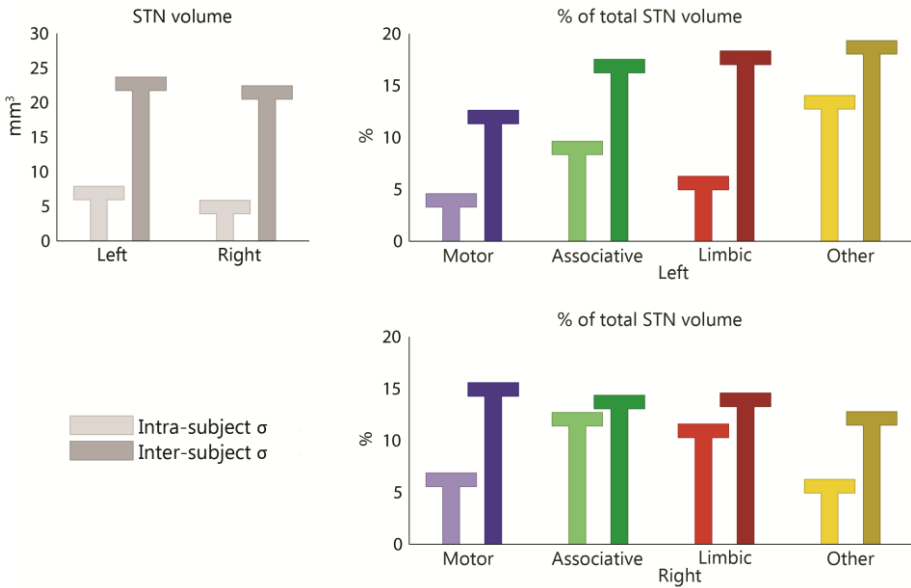| Area		Within subject	Between subject
Left	STN	7.9	23.69
	Motor	4.58	12.61
	Associative	9.63	17.52
	Limbic	6.25	18.32
	Other	14.03	19.32
Right	STN	5.87	22.43
	Motor	6.86	15.57
	Associative	12.7	14.36
	Limbic	11.58	14.57
	Other	6.24	12.78

Figure 6.7: *Comparison of the intra-subject (light bars) standard deviations (σ) and inter-subject (dark bars) standard deviations of the volumes of the subthalamic nucleus (STN) and the relative volumes of the sub-territories.*

6.4.6   Overlap

The overlap of the subdivisions within the STN indicates that one voxel can be connected to more than one cortical mask. This is also reflected in the underlying probability maps of the connections of the STN to each cortical mask. Figure 6.8 shows examples of these probability maps of three subjects. This indicates that the functional zones indeed gradually transition into each other.
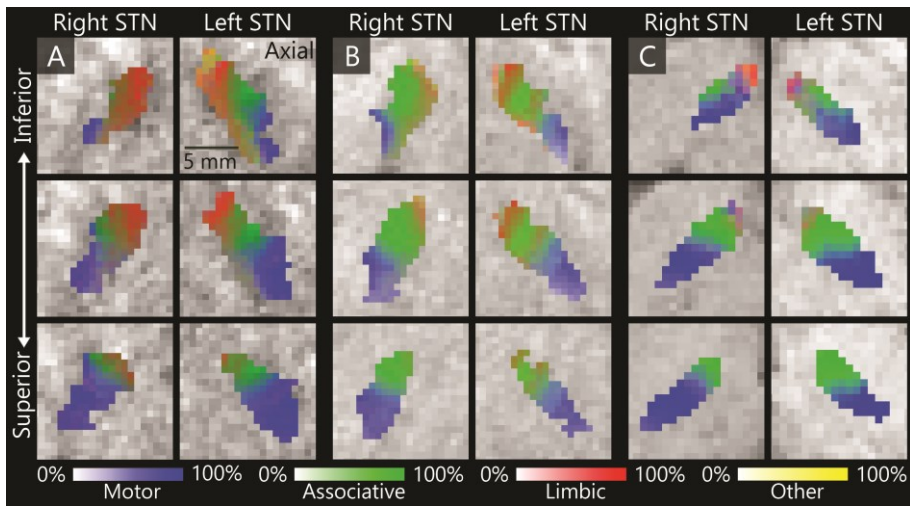
Figure 6.8: The percentage of connectivity to the motor (blue), associative (green), limbic (red), and remaining (yellow) cortical areas in three axial slices through the left and right STN ordered from inferior to superior in three subjects (A, B, and C).

6.4.7   Illustrative cases of implanted electrodes in the motor part of the STN

Figure 6.9 shows that the active contacts of five example cases, as defined during the postoperative programming, indeed correspond to our predicted motor zones, which were created with solely non-invasive preoperative data.
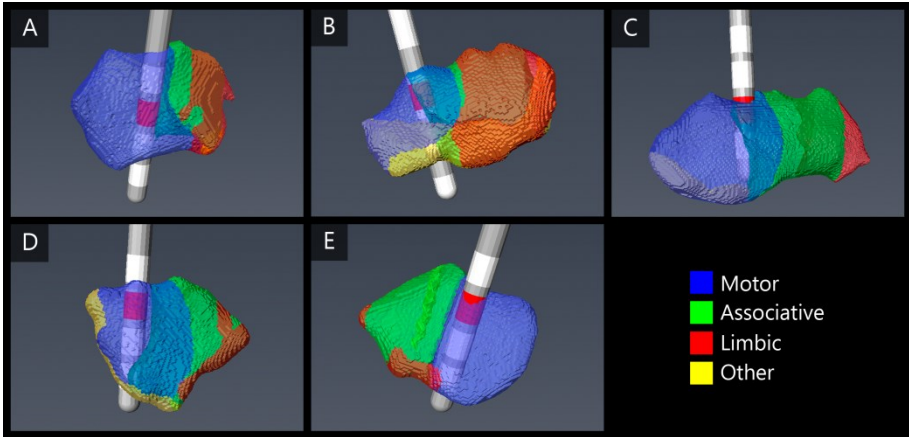
Figure 6.9: Examples of the electrode position in five STNs. The active contacts (red) lie within the computed motor areas.

6.5   Discussion

Ultra-high field MR imaging has enabled us to reliably visualize the motor and non-motor zones of the STN of individual patients with PD referred for deep brain stimulation surgery. We expect that this will facilitate patient-specific and selective targeting of the motor part of the STN, thereby enhancing surgical planning at the level of the individual patient. Moreover, the possibility of more accurate image-guided placement has the potential to reduce surgery duration and/or perform surgery under general anesthesia, which both greatly reduce the burden on patients. In addition, the ability to fuse the postoperative CT images with the preoperative 7 T data allows for the visualization of the position of the electrode and contacts. This may provide vital information to determine the optimal location for implantation of DBS leads, not only within the STN but also within its motor zone. Additionally, the optimal lead location could potentially be used, in conjunction with volume of tissue activated models, to determine the best possible programming settings personalized to each patient.

Anatomical, behavioral, and electrophysiological studies have contributed to our understanding of the organization of the STN into subdivisions. Tracers injected in different territories of the primate external globus pallidus showed a segregated labeling of the STN[107], and GABA agonist and antagonist injections into the posterior, medial, and anterior STN had

different effects on behavioral and motor symptoms in non-human primates[106]. Similarly, electrophysiological recordings in patients with PD localized the neurons activated in limb movement (motor region) in the dorsolateral region of the STN[189]. This parcellation has also been investigated in MRI studies of healthy subjects at 3 T. One study investigating the STN's connectivity in twelve healthy subjects showed that there are most probably three connectivity clusters within the STN related to motor, associative, and limbic functions[121]. The averaged locations of these zones in healthy subjects correspond with our findings in individual patients. This arrangement was also observed in another 3 T functional and structural connectivity study based on averaged data of healthy subjects, but could not be demonstrated consistently in all individual subjects[35]. Finally the STN's connectivity was previously investigated in PD patients as well, although this only concerned its motor area and analyses were only performed in a qualitative manner[16]. Here, we show that the three zones can also be objectively and quantitatively identified in patients with PD and, importantly, on an individual basis. With these methods there is no need to average the data to create a general STN model, but rather, patient-specific and individual models for each patient can be created.

We have found a considerable overlap between the different segmented zones of the STN. Two possible explanations could account for these results; first, the probabilistic nature of the applied connectivity measure and partial volume effects allow for multiple connections per individual voxel. Second, the overlap may indeed reflect the actual pathways that are not segregated but partially integrated. This is in line with a tracing study in non-human primates showing overlapping projections from M1 to the dorsolateral STN and from prefrontal cortical areas to the anterior, ventral, and medial half of the STN[92]. It is known that STN neurons located in the border zones receive multiple inputs and are responsible for the integration of information from different cortical regions performing different functions. To what extend stimulation of this overlapping area will result in beneficial motor effects or unwanted side-effects, remains to be seen.

The average STN volume that we found (125.4 mm^3) is in line with previous findings[121,146]. A variation in the total volumes exists and is reflected also in the relative volumes of the different functional zones. However, regardless of this variability, we also found a few outliers of exceptionally small

associative (n = 1), motor (n = 2), or limbic zones (n = 9). In addition, in some cases we observed deviations of the arrangement of the functional zones, in the sense that the one STN territory showed small protrusions into another territory to a larger extend than the expected overlap. Finally, we observed sporadic connections to the remaining cortical areas. These deviations might be the result of false positives and negatives inherent to probabilistic tractography. Nevertheless, the relatively small contribution of the remaining cortical area to the STNs' maps indicates that the reconstructed connectivity we found here represents actual anatomical connections. Despite these few deviations, in all 34 STNs, the posterolateral portion was consistently connected to the motor cortical areas.

Our data and methods were validated by reproducing the earlier demonstrated connectivity based parcellation of the thalamus[23]. Our results are very similar to the established segregation of the thalamus, demonstrating that our ultra-high field MRI data and methods are suitable for parcellating subcortical structures. The small discrepancies found between our and Behrens's et al. thalamic parcellation may be explained by underlying differences between subjects, discrepancies in the definitions of the cortical areas, or differences in the orientation and location of the visualized cut through the thalamus. Furthermore, the STN parcellation was validated with the final DBS electrode location in five example cases. We confirm that the active contacts, as determined by the micro-electrode recording during surgery and the programming post-surgery, were indeed located within the motor zone as defined by this work. This illustrates its future potential value.

To assess the reproducibility of our methods, the measurements and analyses were repeated four times on one subject. Although the numbers are too small to reliably assess significance, the within subject standard deviation was smaller than the between subject standard deviation for both the total STN volumes and all volumes of the sub-territories. This suggests that the variability that we find between patients can, at least partially, be explained by the underlying variability in the patients' anatomy; thus providing a detailed mapping of the patient's own STN, not based on a standard and common anatomical atlas, which should have a high priority for enhancing targeting accuracy for DBS surgeries. Furthermore, the fact that similar results were produced with datasets collected at two different

6

centers (with small differences in the scanning protocols), also indicates that the used analysis pipeline is robust and independent of acquisition parameters.

The clear visualization of the STN, relatively short scan times, and high resolution parcellation of the STN, result from the known benefits of ultra-high field MRI[67,215,228] and demonstrate its clinical utility. Although 7 T MR scanners are not yet accessible for all DBS centers, their numbers are growing quickly; in fact, an FDA approved system is expected to be released in the near future.

There are a few limiting factors that are inherent to high resolution MRI and structural connectivity mapping of brain structures. For one, movement artifacts are an obvious limitation when scanning movement disorder patients. They were minimized by using scan protocols that were optimized for this patient group[2,128]. Second, ultra-high field diffusion imaging is sensitive to signal loss in the temporal lobes[180]. To partly overcome these problems, dielectric pads were used if they could be fitted comfortably. Nevertheless, this issue may explain why the observed connections to the limbic regions in the temporal and orbitofrontal areas were less prominent than expected. Also, contrary to, for example, tracing or electrophysiological studies, diffusion-based tractography cannot infer information on the signaling direction of the connections. In addition, despite the sub-millimeter details provided by 7 T MRI, connections occurring at a smaller scale, such as disynaptic connections, may have been ignored in the analyses. Furthermore, sampling the distribution of diffusion directions in each step, using probabilistic tractography will result in some false positives and false negatives depending on data quality, track length, crossing fiber areas, and partial volume effects. The latter of those, which may have occurred in voxels bordering the STN, might further explain the tracked connections to the remaining cortical areas. It may also account for the variability in observed volume of the limbic zone of the STN, which was previously demonstrated to extend to the neighboring lateral hypothalamus in primates[92]. In addition, we only considered the cortico-subthalamic connections. Although the subcortical connections of the STN underpin its important role in the basal ganglia[128,175], creating functional segregation maps from them is difficult because of the complex interplay of different functions. The functional segregation of the cortex and especially of the

6

motor cortical areas is much better understood and their large surface areas make them more robust to small segmentation errors in the cortex. Therefore, using these connections to functionally subdivide the STN is more realistic. Finally, the number of zones detected within the STN is related to the predefined number of cortical segmentations and can in this study not exceed four. Using a clustering algorithm to parcellate the cortex and STN, might result in a more individualized number of clusters. Future studies, with higher spatial resolution, will address the clustering approach to determine the number of zones independently.

Although the ability to identify the different sub-territories of the STN is a leap forward in the process of direct targeting, more extensive study is needed to bring it to clinical practice. Furthermore, the methods developed here, open new doors for a better understanding of Parkinson's disease and its treatments. Comparisons with healthy control subjects may provide new insight into the pathologic anatomy in PD. Moreover, the proposed methods may lead to a better understanding of what circuits are being stimulated and how this affects patient outcome.

6.6   Conclusion

The motor part of the STN is the main target in deep brain stimulation surgery for patients with PD. Using ultra-high field MRI technology and tractography-based data analysis methods, we have provided a proof of concept for identifying the motor and non-motor zones of the STN in individual patients. We have observed that there is a substantial variation between individuals with PD. This type of new data may potentially allow for optimized surgical planning at the level of the individual patient preoperatively and create the possibility of patient-specific targeting and programming of the DBS therapy postoperatively. We see this as a critical step towards development of patient-specific deep brain stimulation for PD.

6.7   Acknowledgements

6

CHAPTER 7

POST MORTEM CONNECTIVITY

7.1 Abstract

The subthalamic nucleus, substantia nigra, and globus pallidus, three nuclei of the human basal ganglia, play an important role in motor, associative, and limbic processing. The network of the basal ganglia is generally characterized by a direct, indirect, and hyperdirect pathway. This study aims to investigate the mesoscopic nature of these connections between the subthalamic nucleus, substantia nigra, and globus pallidus and their surrounding structures.

A human post mortem brain specimen including the substantia nigra, subthalamic nucleus, and globus pallidus was scanned on a 7 T MRI scanner. High resolution diffusion-weighted images were used to reconstruct the fibers intersecting the substantia nigra, subthalamic nucleus, and globus pallidus. The course and density of these tracks was analyzed.

Most of the commonly established projections of the subthalamic nucleus, substantia nigra, and globus pallidus were successfully reconstructed. However, some of the reconstructed fiber tracks such as the connections of the substantia nigra pars compacta to the other included nuclei and the connections with the anterior commissure have not been shown previously. In addition, the quantitative tractography approach showed a typical degree of connectivity previously not documented. An example is the relatively larger projections of the subthalamic nucleus to the substantia nigra pars reticulata when compared to the projections to the globus pallidus internus.

This study shows that ultra-high field post mortem tractography allows for detailed 3D reconstruction of the projection of deep brain structures in humans. Although the results should be interpreted carefully, the newly identified connections contribute to our understanding of the basal ganglia.

7

7.2   Introduction

The basal ganglia are a network of nuclei deep in the brain, consisting of the substantia nigra (SN), subthalamic nucleus (STN), globus pallidus (GP), and striatum as their core structures. The network plays a fundamental role in a wide range of processes related to motor, associative, and limbic functions[151,204]. Its key role is illustrated by diseases of the basal ganglia, such as Parkinson's disease (PD), where disruptions in the circuit lead to the typical motor, cognitive, and mood changes[57,164]. Modulation by electrical stimulation of motor and limbic parts of the basal ganglia nuclei, such as the STN and GP, has substantial therapeutic effects in neuropsychiatric disorders, including PD, obsessive-compulsive disorder, and Tourette's syndrome[108,139,196].

In humans, the striatum can be divided into the caudate nucleus, putamen, and nucleus accumbens; the substantia nigra can be divided into a pars compacta (SNc) and a pars reticulata (SNr); and the globus pallidus into an internal (GPi) and an external part (GPe) and the ventral pallidum. Classically, the basal ganglia circuit consists of three pathways: the direct, the indirect, and the hyperdirect pathway[156]. In the direct pathway, the cortex projects onto the striatum, which directly connects to the GPi and SNr; known as the output structures of the basal ganglia. In the indirect pathway, the striatum also projects onto the GPi and SNr, but via a detour through the GPe and STN. Finally, in the hyperdirect pathway, the STN directly receives its input from the cortex and then transfers it to the GPi and SNr again. This model is largely based on histology, electrophysiology, and tracing studies in rodents[77,173] and monkeys[7,41,92,96,160,221,231], and on anatomical and histological studies in dissected human brains[46,137].

MRI techniques allow for imaging of the 3D anatomy, connectivity, and functionality of the intact human brain[35,63,127,128]. However, although these studies provide human-specific contributions to the basal ganglia model, they can only infer the brain's connections at a coarse scale. Newly emerging ultra-high field (7 T) MRI scanners provide the opportunity to investigate the human brain at a higher resolution, higher contrast, and with less noise compared to the more widely available 1.5 and 3 T MRI scanners. Moreover, scanning of post mortem specimens allows for increasing the scan times, which leads to an additional improvement in image quality[179]. In this study, we acquired ultra-high resolution structural and diffusion-weighted images

7

of a human post mortem brain specimen including the GP, STN, and SN at 7 T. Reconstructed pathways of these nuclei demonstrate both the detailed wiring of a subset of the basal ganglia network in line with the established models, as well as novel details.

7.3 Materials and methods

7.3.1 Data acquisition

A unilateral formalin-fixed human brain specimen (Figure 7.1) was acquired from the Maastricht University Body donation program, Department of Anatomy and Embryology. The Local Medical Ethics Committee of Maastricht University has been informed about educational and research activities concerning donor material. A handwritten and signed codicil from the donor, drafted when still alive and well, is kept at this department, as is required by Dutch law for the use of cadavers for scientific research and education. The donor, who was aged between 70 and 95 years, had no known neurological disorders. Time from death to formalin fixation was approximately 12 hours. Three basal ganglia nuclei were completely enclosed in the post mortem piece: the STN, SN, and GP. Approximately 12 months after time of death, the specimen was embedded in phosphate buffered saline (PBS) for seven days during which the PBS was refreshed three times, before being scanned in PBS on a 7 T MRI scanner (Magnetom 7 T, Siemens, Erlangen, Germany). The protocol consisted of a 3D gradient recalled echo (GRE) and a pulsed gradient spin echo segmented 3D diffusion-weighted echo planar imaging (3D-dwEPI) sequence. The 3D-dwEPI was acquired with 3 lines-per-shot (segmentation factor 40), and a b-value of 2800 s/mm^2. In addition to 8 b0-volumes, 60 diffusion directions were sampled. Given the scan time of 42 hours, this allowed for a good identification of multiple fiber orientations while still being capable of scanning with a high spatial resolution of 0.5 × 0.5 × 0.5 mm^3. Other scanning parameters are listed in Table 7.1.

7

Table 7.1: Scan parameters.

Sequence	Resolution (mm^3)	Matrix size	TE (ms)	TR (ms)	Flip angle (°)	Scan time (hh:mm:ss)
GRE	0.3 × 0.3 × 0.3	192 × 192 × 208	11	37	8	00:13:04
3D-dwEPI	0.5 × 0.5 × 0.5	120 × 120 × 112	60	500	90	42:22:13

3D-dwEPI = 3D diffusion-weighted echo planar imaging. GRE = Gradient recalled echo. TE = Echo time. TR = Repitition time.
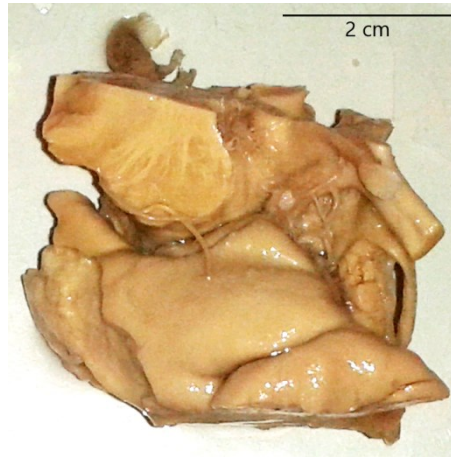
Figure 7.1: Unilateral human post mortem sample including the globus pallidus, subthalamic nucleus, and substantia nigra.

7.3.2   Data processing

The diffusion-weighted images were corrected for eddy current-induced distortions and motion with FSL (Analysis Group, FMRIB, Oxford, UK)[102]. The STN, SNc, SNr, GPi, and GPe were manually delineated from the GRE image using ITK-SNAP software[233]. Because the striatum was only partially enclosed in the specimen, it was not considered in the analysis. These segmentations were then affinely coregistered to the corrected diffusion-weighted space along with the GRE image using FSL's FLIRT[10].

7.3.3   Fiber tracking

Constrained spherical deconvolution-based probabilistic fiber tracking with a maximum harmonic order (lmax) of 8 was performed on the whole specimen with MRtrix[208]. Optimal parameter values were determined by visual inspection of the obtained fiber tracks in 3D; parameter sets that

resulted in unrealistically short, long, straight, and/or noisy fiber tracks were excluded. This resulted in a step size of 0.05 mm, a minimum radius of curvature of 0.1 mm, a fiber orientation distribution (FOD) amplitude cutoff of 0.3, and an FOD amplitude cutoff for initiation of 0.01. Only fiber tracks intersecting the SN, STN, or GP were selected for further analysis, which resulted in a total of 416,832 fiber tracks.

7.3.4 Connectivity analysis

To investigate the connectivity pattern of the included basal ganglia nuclei, various sets of fiber tracks were isolated, based on their direct or indirect connections to other manually segmented nuclei and known fiber bundles, including the red nucleus, ventral pallidum, anterior commissure, ansa lenticularis, internal capsule, sublenticular internal capsule, interthalamic adhesion, and the region of the medial lemniscus. The origin of these projections within the STN, SN, or GP was then mapped by computing for every voxel within these nuclei, the percentage of fibers running to each of its projection sites. Both these steps were performed with MRtrix[208]. Only projection sites with at least 1 % of the fibers connecting to either of the basal ganglia nuclei were taken into account. In addition to these indirect connections, where a fiber track connects two structures via a detour through another structure, the direct connections between the SNc, SNr, STN, GPi and GPe were also analyzed. To this end, custom written MATLAB (The MathWorks, Natick, U.S.A.) code was used to cut the original tracks into single track segments that directly connected the STN, SNc, SNr, GPi, or GPe with each other without passing through another of these five structures. To reduce the computation time of the analysis of the direct connections to less than 24 hours, it was performed on only 9,000 randomly selected original tracks, resulting in a total of 14,542 direct track segments.

7.3.5 Description of the results

Anatomical orientations will be expressed in posterior-anterior, lateral-medial, and superior-inferior directions. Visualizations of the fiber bundles either have one color, or they follow the standard color coding for fiber orientation (posterior-anterior = green, lateral-medial = red, superior-inferior = blue).

7.4   Results

Three axial slices through the GRE images, with their anatomical annotations are shown in Figure 7.2. The hypointense SNc can be clearly separated from the SNr (Figure 7.2 A), and the GPe and GPi are separated by
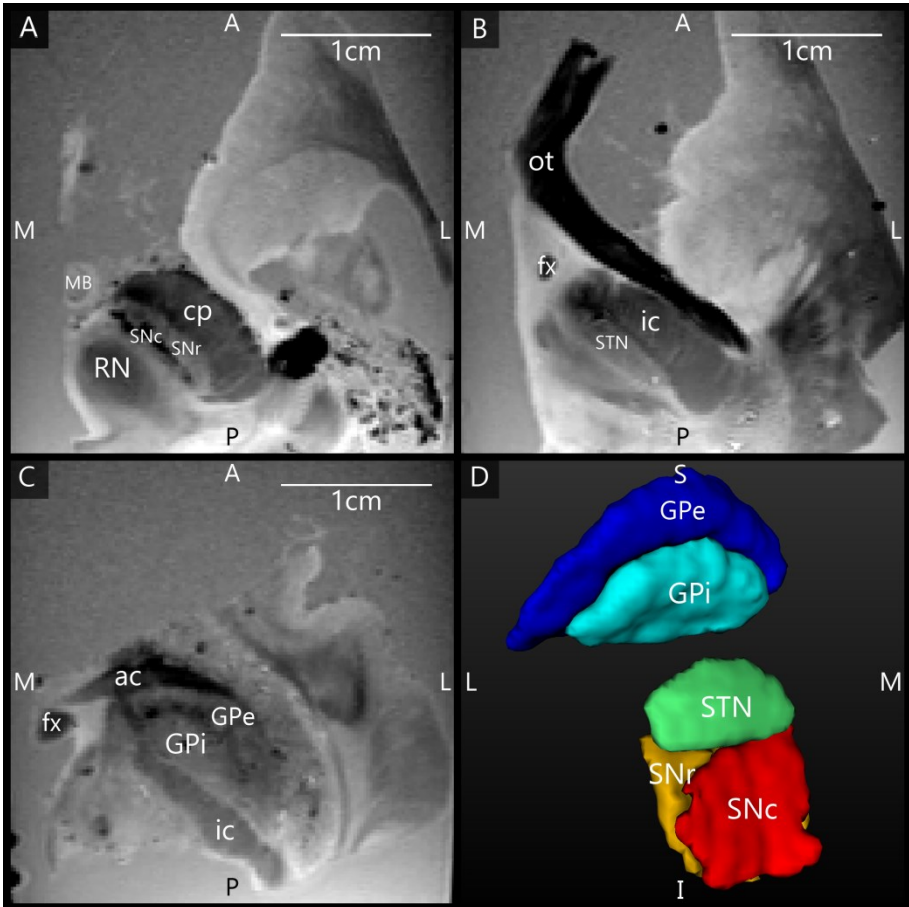
Figure 7.2: A-C) Axial GRE images through the SNc and SNr, STN, and GPi and GPe, at three different levels ordered from the most inferior level (A) to the most superior level (C). D) 3D Visualization of the segmented structures. A = Anterior. ac = anterior commissure. cp = cerebral peduncle. fx = fornix. GPe = External globus pallidus. GPi = Internal globus pallidus. I = Inferior. ic = internal capsule. L = Lateral. MB = Mammillary body. M = Medial. ot = optic tract. P = Posterior. RN = Red nucleus. S = Superior. SNc = Substantia nigra pars compacta. SNr = Substantia nigra pars reticulata. STN = Subthalamic nucleus.

the darker medial medullary lamina (Figure 7.2 C). Figure 7.2 D shows 3D representations of the segmented structures, which had the following volumes: STN = 100.5 mm³, SNc = 138.8 mm³, SNr = 142.6 mm³, GPe = 611.9 mm³, and GPi = 271.8 mm³.

7.4.1 Connections

Table 7.2 gives an overview of structures directly and indirectly connected to the STN, SNc, SNr, GPe, and GPi. The number of tracks connecting two structures is expressed as a percentage of the total number of tracks through either the STN, SNc, SNr, GPe, or GPi. For example, 35.5 % of all connections that course through the STN connect to the SN. The percentages of tracks through each structure add up to more than 100 %, because a fiber track often connects one seed structure to multiple targets. Each track is counted once, even if it leaves a seed structure at two different borders. Connections to the GP are subdivided into connections going to the anteromedial and posterolateral halves of the GPe and GPi. A few of the reconstructed paths could not be reliably identified as known fiber bundles, and are therefore, in Table 7.2, described by their location.

7

Table 7.2: *Structures and fiber paths connected to the STN, SNc, SNr, GPe, and GPi. Each column shows the percentage of reconstructed tracks that connected the STN, SNc, SNr, GPe, or GPi (seed structures) with their targets. Only target structures connected with at least 1 % of the seed's tracks were analyzed.*

	Seed structures				
	STN	SNc	SNr	GPe	GPi
Connecting structures	%	%	%	%	%
Subthalamic nucleus		17.1	13.3	6.0	6.6
Substantia nigra	35.5			32.3	29.7
SN pars compacta	30.2		58.8	22.7	22.4
SN pars reticulata	28.6	71.4		26.7	20.2
Globus pallidus	29.9	51.4	43.7		
External GP	19.3	41.1	39.8		64.7
Anterior GPe	10.6	16.1	11.1		15.9
Posterior GPe	9.5	28.3	31.5		53.1
Internal GP	17.2	32.8	24.5	52.4	
Anterior GPi	17.0	30.3	15.9	30.3	
Posterior GPi	4.0	21.4	19.0	40.5	
Ventral pallidum				2.8	
Red nucleus				1.1	2.5
Connecting fiber paths	%	%	%	%	%
Anterior commissure				6.1	1.6
Ansa lenticularis	8.8	19.5	6.3	15.1	36.9
Inferior of SN	17.6	79.4	58.5	22.6	24.0
Internal capsule	94.7	89.7	98.2	78.5	73.1
Interthalamic adhesion					1.7
Lateral of ic		2.9	24.7		1.8
Medial to RN				1.8	1.7
Medial to STN	10.7			2.4	5.2
Sublenticular ic	10.5	9.3	12.0	21.7	29.6

GPe = External globus pallidus. GPi = Internal globus pallidus. ic = internal capsule. RN = Red nucleus. SNc = Substantia nigra pars compacta. SNr = Substantia nigra pars reticulata. STN = Subthalamic nucleus.

7.4.2   Direct connections within the basal ganglia

The tracks described in Table 7.2 represent both direct and indirect connections. In indirect connections, tracks connect two structures via a detour through another structure. At least half of the original tracks connect more than two structures. Table 7.3 and Figure 7.3 focus solely on the direct connections between the STN, SNc, SNr, GPe, and GPi. The table is asymmetric because it shows the percentage of connections relative to the total number of direct connections of each structure. For example, of all direct connections between the STN and the four other involved structures 39.9 % directly connected the STN with the SNc. Even though this step was performed on only a subset of 14,542 direct track segments, the number of direct connections between each pair of structures varied from 61 to 6,683. It

Table 7.3: Percentage of fibers directly connecting each structure. Each column shows the percentage of tracks connecting two nuclei, relative to the total number of direct connections through this nucleus.

	STN	SNc	SNr	GPe	GPi
STN	x	10.3	9.3	3.4	4.8
SNc	39.9	x	76.7	1.3	7.9
SNr	39.4	83.5	x	9.8	13.6
GPe	7.8	0.8	5.3	x	73.7
GPi	12.9	5.5	8.7	85.6	x
Total	100	100	100	100	100

GPe = External globus pallidus. GPi = Internal globus pallidus. SNc = Substantia nigra pars compacta. SNr = Substantia nigra pars reticulata. STN = Subthalamic nucleus.
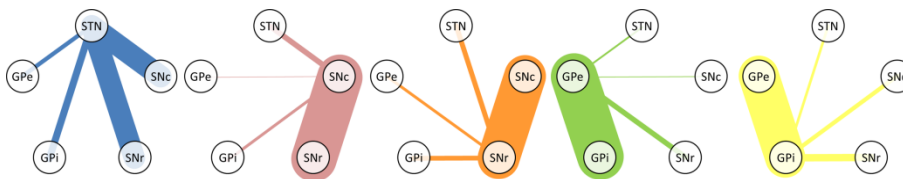
Figure 7.3: Graphical representation of Table 7.3. The line thickness is proportional to the relative number of fiber tracks connecting the structures. GPe = External globus pallidus. GPi = Internal globus pallidus. SNc = Substantia nigra pars compacta. SNr = Substantia nigra pars reticulata. STN = Subthalamic nucleus.

is therefore expected that performing this step on only a subset of the entire set of fiber tracks, will not have greatly influenced the results. The following sections (Section 7.4.2.1 to Section 7.4.2.6), describe the anatomy of these connections.

7.4.2.1 STN

The fiber tracks within the STN ran from its posterolateral to its anteromedial side. This is in line with the direction of the dendrites that also arborize along this main axis[191]. Towards the anteromedial side of the STN, the tracks fanned out in two directions, slightly more medial and slightly more lateral than their initial direction. This fiber direction within the STN also clearly separated it from the laterally bordering internal capsule whose fibers run inferior-superiorly (see Figures 7.4 A and B).
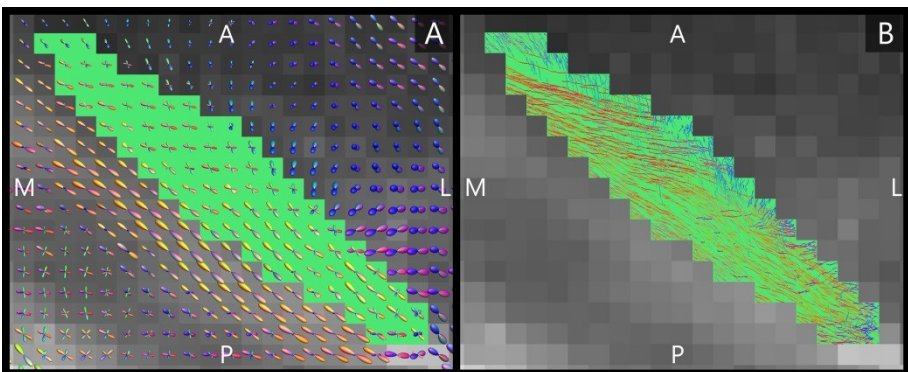
Figure 7.4: Orientation of the fiber tracks of the subthalamic nucleus. A) The diffusion direction within the STN (green, axial plane) and its surrounding structures. B) The fibers tracked within the STN. In A) and B), the FOD-glyphs and tracks are color coded for orientation. A = Anterior. L = Lateral. M = Medial. P = Posterior.

7.4.2.2 STN-GP connections

The GPi is classically considered one of the output structures of the basal ganglia, receiving excitatory input from the STN[157]. These connecting fibers were successfully reconstructed in this study and were found to leave the STN at the anterior and medial side, circle anteriorly around the internal capsule and enter the GPi at its anterior and inferior borders, putatively

following the course of the ansa lenticularis (Figure 7.5 A). The STN has also been shown to excite the GPe[157]. These connections to the GPe were also reproduced and coursed either anteriorly around the internal capsule, in a bundle superior to the fibers connecting to the GPi, or they coursed straight through the internal capsule to the GPe's medial border (Figure 7.5 A).
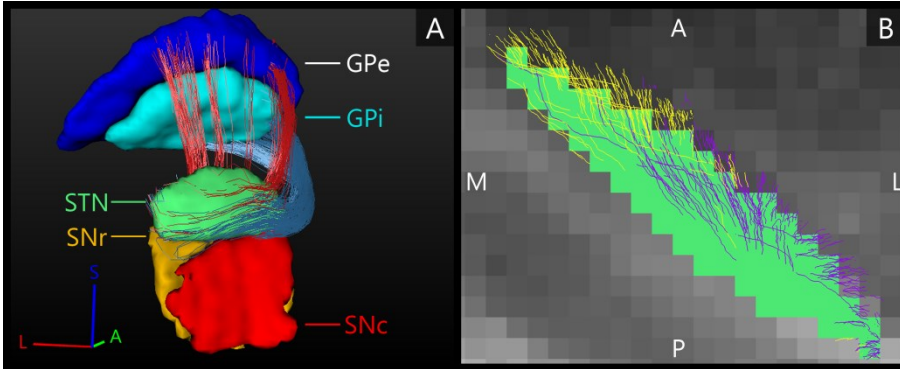
Figure 7.5: Connections of the STN. A) Reconstructed tracks directly connecting the STN to the GPe (red tracks) and to the GPi (blue tracks). Note that it is difficult to appreciate the actual number of tracks in the figure. B) The STN (green, axial plane) and the fiber tracks connecting it to the SNc (purple tracks) and to the SNr (yellow tracks). GPe = External globus pallidus. GPi = Internal globus pallidus. SNc = Substantia nigra pars compacta. SNr = Substantia nigra pars reticulata. STN = Subthalamic nucleus.

7.4.2.3   STN-SN connections

Just like the GPi, the SNr is classically considered one of the output structures of the basal ganglia receiving excitatory input from the STN[159]. In addition to these known connections between the STN and SNr, in this study we also found connections between the STN and SNc. The number of tracks found to directly connect the STN with the SNr and with the SNc was approximately the same. The STN borders the superior boundaries of both the SNc and the SNr. Not surprisingly, the tracks left the STN at its inferior lateral border and entered the SN at the superior border, where these two structures meet. The tracks to the SNc left the STN more anteriorly than the tracks to the SNr (see Figure 7.5 B).

The tracks entered the SNc throughout its entire superior border, whereas the connections to the SNr mainly connected to the posterior part of its superior border. For both parts of the SN, the tracks were concentrated in the posterior parts of the SNc and SNr, but in the SNc a small proportion of the tracks also fanned out throughout a large part of the SNc (see Figure 7.6). This means that although the percentage of STN tracks that reached the SNc and SNr (either directly or indirectly) are similar (30.2 % and 28.6 %), within the SNc they connected to a larger volume than within the SNr.
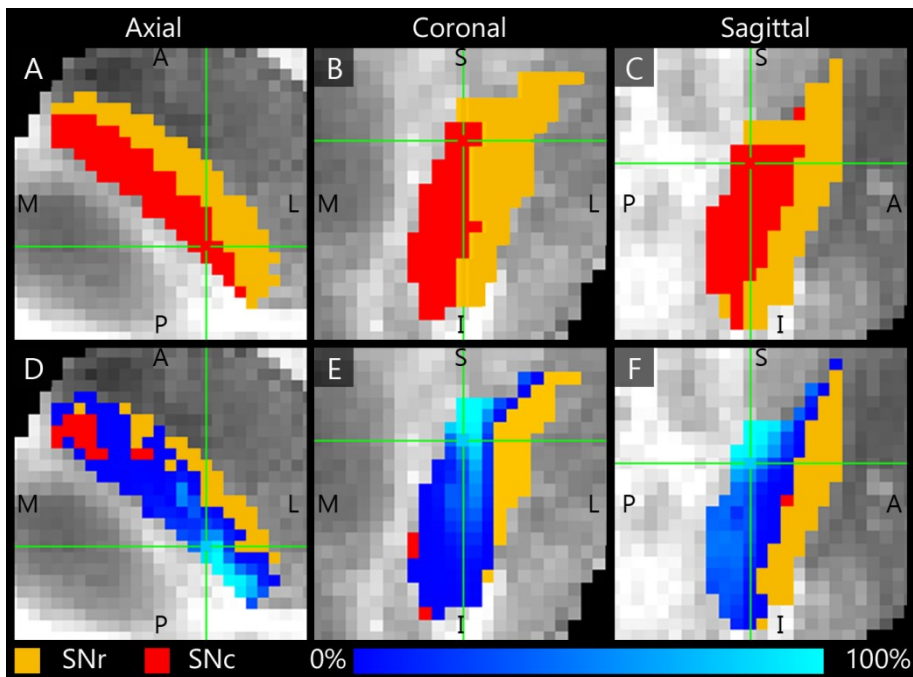
Figure 7.6: Percentage of fiber tracks from the STN that entered the SNc (red) and SNr (orange). The top row (A-C) shows three slices through the SNc and SNr. The bottom row (D-E) shows these same slices, with on top of it, for each voxel, the number of tracks connecting that voxel with the STN expressed as a percentage of the total number of tracks through that voxel. A = Anterior. I = Inferior. L = Lateral. M = Medial. P = Posterior. S = Superior. SNc = Substantia nigra pars compacta. SNr = Substantia nigra pars reticulata.

7

7.4.2.4   SNc-SNr connections

Being two adjacent structures, many fiber tracks were found to connect the SNc with the SNr. Although in both segments the fibers traveled along the plane of the border of the both structures, interestingly, in the SNc the fibers traveled on average in superior-posterior direction, whereas in the SNr they traveled more diagonally from superior-medial to inferior-lateral (see Figures 7.7 A and B).

7.4.2.5   SN-GP connections

The SNr and GPi represent a common structure separated by the internal capsule, both providing the output of the basal ganglia network. The SNr and GPi both receive, among other sources, inhibitory input from the GPe[57,159]. This relation between the GP and the SNr was also found here, with connections tracked between both structures. Additionally we found connections between the SNc and both elements of the GP.

Similar to the STN-GPi connection, the tracks from the SNc to the GPi circled anteriorly around the internal capsule to enter the GPi at the anterior part of its medial border. Some connections between the SNr and GPi followed this path as well, but others traversed straight through the internal capsule, entering the GPi more laterally along its medial border. The fiber tracks circling anteriorly of the internal capsule, left the SNr and SNc at their anterior side, but the fibers crossing through the internal capsule left the SNc at its lateral border (Figure 7.7 C).

The connections between the SN and the GPe mainly traversed straight through the internal capsule. Relatively fewer fiber tracks connected the GPe to the SNc than to the SNr (1.3 % vs 9.8 %) leaving only the anterior superior apex of the SNc connected to the anterior inferior border of the GPi. The fiber tracks of the SNr emerged from the anterior half of the superior border of the SNr and entered the GPe at its border with the internal capsule (Figure 7.7 D).
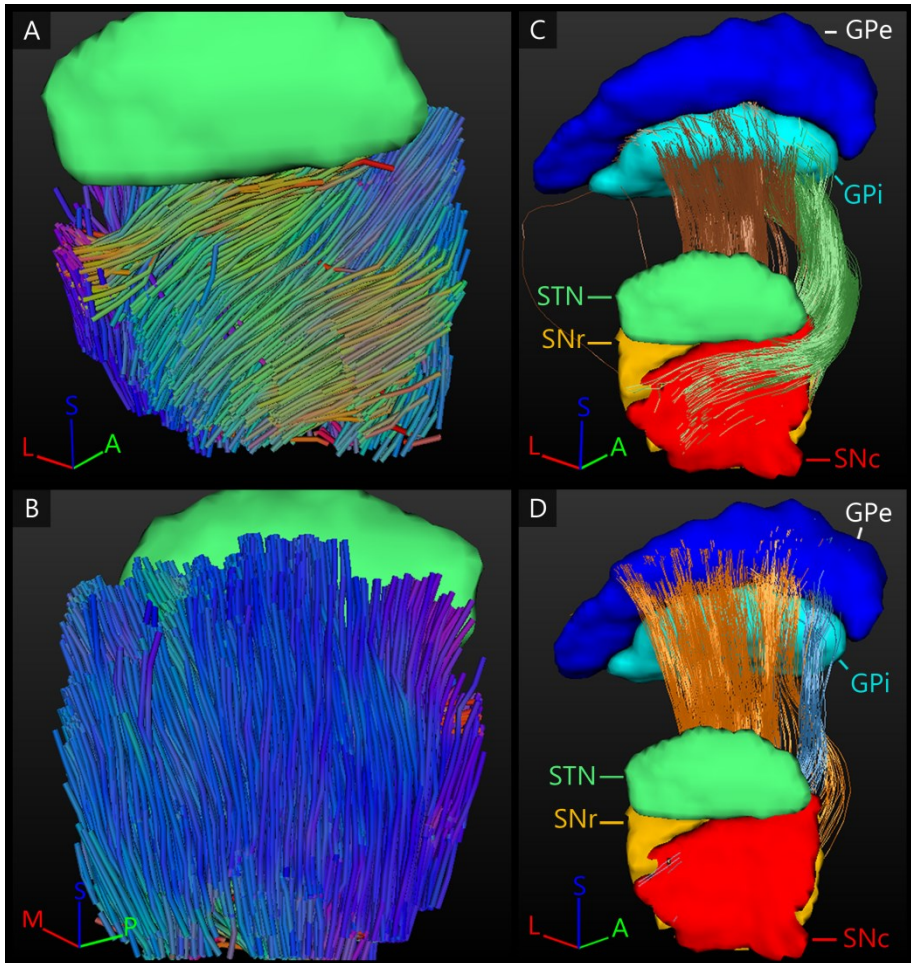
Figure 7.7: Fiber tracks of the SNc and SNr. A-B) Fiber direction within the SNc (A) and SNr (B) color coded for orientation. C) Fibers tracked between the GPi and SNr (brown tracks) and SNc (green tracks). D) Fibers tracked between the GPe and SNr (orange tracks) and SNc (blue tracks). A = Anterior. GPe = External globus pallidus. GPi = Internal globus pallidus. L = Lateral. M = Medial. P = Posterior. S = Superior. SNc = Substantia nigra pars compacta. SNr = Substantia nigra pars reticulata. STN = Subthalamic nucleus.

7.4.2.6 GPe-GPi connections

The GPe inhibits the GPi[57,159]. Connections between these two structures were indeed established here. In the GPi, the tracked fibers were mainly oriented from its anterior and medial side to its posterior and lateral borders

(Figure 7.8 A). Similarly, connections between the GPi and GPe started in the medial inferior part of the GPi and coursed in a slight curve along the GPe's longest axis towards the superior lateral part of the GPe (Figure 7.8 B). Being a bigger structure, the fiber direction in the GPe was less homogeneous, with the majority of the fibers following the same direction as in the GPi, but part of the fibers left the GPe at its posterior border (Figure 7.8 C).
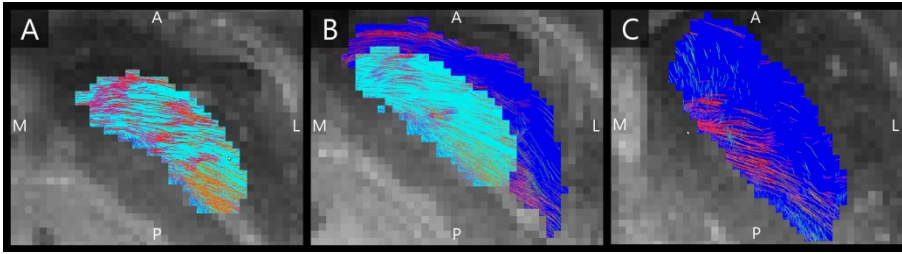
Figure 7.8: Tracked fibers through the internal globus pallidus (light blue) and external globus pallidus (dark blue) in three different axial planes. The tracks are color coded for orientation and the planes are ordered from inferior (A) to superior (C). A = Anterior. L = Lateral. M = Medial. P = Posterior. S = Superior.

7.4.3 Connections to other structures and fiber tracks

Additional to these direct connections within the basal ganglia structures, direct and indirect connections with other basal ganglia structures and fiber paths were found as well (Table 7.2). From the GP, fiber tracks were reconstructed to the red nucleus and ventral pallidum although the percentages of reconstructed paths were low (less than 3 %).

The most dominant of the connected white matter tracks were the strong connections to the internal capsule, which separates the STN and SN from the GP. In case of the STN for example, 95 % of its tracked fibers either followed the internal capsule in superior direction, or crossed straight through it to connect to the GP (as explained in section 7.4.2.5) (see Figure 7.9 A).

Also, fibers were tracked from these nuclei coursing inferiorly towards the brain stem. The SNc and SNr received more than 50 % of their tracks from a fiber bundle located inferiorly in the area of the medial lemniscus. Many of these tracks continued to follow the course of the internal capsule in superior direction (see Figure 7.9 B).

Fiber tracks that left the GP at its lateral side, continued to fan out along the path of the sublenticular internal capsule, thereby also indirectly connecting the SN and STN to this fiber path (see Figure 7.9 C). The SN was also connected to a fiber bundle that coursed laterally upwards around the internal capsule to follow the course of the sublenticular internal capsule. Finally, a small amount of fiber tracks was found connecting the GP to the bordering anterior commissure, to the areas medial of the STN and the red nucleus, and to the putative interthalamic adhesion.
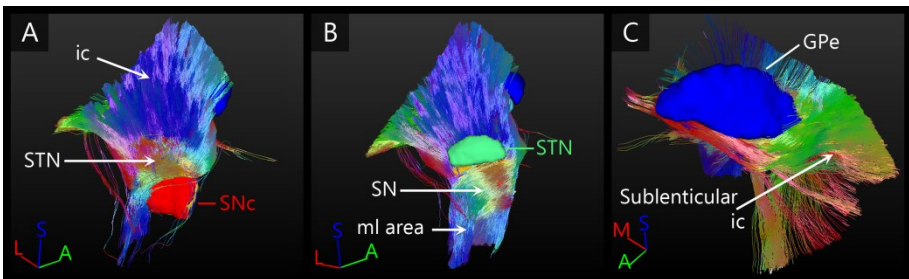
Figure 7.9: Connections with fiber paths. A) Fiber tracks connecting the subthalamic nucleus (STN) and the internal capsule (ic). B) Fiber tracks coursing inferiorly from the substantia nigra (SN) C) Tracks fanning out along the course of the sublenticular internal capsule. All tracks are color coded for orientation. A = anterior. GPe = External globus pallidus. I = Inferior. ic = internal capsule. L = Lateral. M = Medial. ml = medial lemniscus. S = Superior. SNc = SN pars compacta.

7.5   Discussion

We performed high resolution tractography of a formalin-fixed post mortem human brain sample including the substantia nigra, subthalamic nucleus, and   globus   pallidus.   With   a   diffusion-weighted   resolution   of $0.5 \times 0.5 \times 0.5$ mm^3 isotropic, we generated detailed reconstructions of the connections of these nuclei.

Diffusion-weighted imaging depends on the passive diffusion of water molecules, also called Brownian motion, that also occurs in post mortem tissue. An important advantage of ex vivo diffusion-weighted imaging over in vivo imaging is the possibility of long scan times. This again facilitates diffusion images with high resolution, high contrast, and low noise.

Compared to a resolution of $2 \times 2 \times 2$ mm^3 isotropic, which is common practice for in vivo diffusion imaging, we were able to investigate the brain's connections with a 64 times higher resolution, allowing for investigation of the connections of basal ganglia in great detail and specific to humans.

A few technical considerations have to be taken into account. Firstly, tractography, and especially probabilistic tractography, is sensitive to false positives (reconstructed tracks do not match actual fiber paths) and false negatives (actual fiber paths are not reconstructed). Therefore one should be cautious when interpreting these results, and in particular any asymmetry in the connectivity values between structures, especially when a ground truth is missing. Also, compared to previously reported volumes of the left STN[121] and GP and SN[5] measured with in vivo MRI, our measured volumes are on average 66.7 % smaller, indicating shrinkage of the specimen potentially related to the formalin fixation[184,197]. However, this shrinkage is not expected to affect the relative structural organization of the tissue. Indeed, the sample analyzed here included a few well described fiber bundles, including the anterior commissure and the internal capsule. The reconstructed fibers tracked through them corresponded well with known anatomy, which supports the validity of the remaining tracked connections that are not commonly established. Furthermore, it is likely that short distance connections are overrepresented because they are easier to track than long distance connections. The observed STN-GPi connections (17.2 % of all tracks through the STN), for example, are fewer than the STN-SNr connections (28.6 %). This could reflect a relatively important role for the STN-SNr connection in humans, or it could be an overestimation due to its shorter distance. The same holds for the many projections found between the GPi and GPe. Compensation methods have been proposed[35,155], but were not used in this study to prevent the risk of overcompensation resulting in too many long-distance connections and too few short distance connections. Additionally, the direction of the connections cannot be inferred with tractography techniques. This directionality is already known for many of the basal ganglia connections; however, it is impossible to verify this with diffusion-weighted tractography. It is therefore important to realize that the used descriptions of the courses of the tracks do not reflect the directionality of the projections. For example, the mentioned GPe-STN connections, may also reflect known STN-GPe connections[116]. Similarly, it cannot be inferred whether the connections are inhibitory or excitatory. Finally, the STN, SN,

7

and GP all had many tracks following the internal capsule in superior direction. These tracks could be carrying the connections to the striatum or cortex as incorporated in the basal ganglia model[57,159]. However, the cortex was not included in this study, but it would be interesting to investigate them in a larger post mortem specimen.

We could reconstruct some of the commonly established projections and white matter tracks of the SN, STN, and GP such as the internal capsule, anterior commissure, and ansa lenticularis. Also, we could confirm, at a fine scale and specific to humans, the connections between the STN, SNr, GPi, and GPe, that have been previously established on the basis of rodent, non-human primates[92,191], and a few human studies[11,39,128]. Post mortem diffusion tractography studies in humans have previously been performed at ultra-high field, resulting in a high resolution map of the brain stem[4] and a detailed reconstruction of the dentorubrothalamic tract[39]. A tractography study about the connections within the basal ganglia was previously performed in vivo by Lenglet et al.[128]. The STN-GPe, STN-GPi, STN-SN and SN-GPi that we find are in line with their results. However, some of the observed fiber tracks, such as the connections of the GP with the anterior commissure, challenge the existing concepts of the basal ganglia network. Although it is not our intention to change the current way of thinking, we would like to stimulate a discussion about some of the novel findings without being too speculative.

To reduce scan time and increase imaging resolution, only a small brain sample was scanned. Because the striatum was not completely incorporated in the specimen, it was disregarded in the analysis. However, the observed connections from the SNc within the internal capsule may represent some of the known connections to the striatum[57,164] as also observed in other anatomical studies[137]. Less well described connections that we found are connections of the SNc with the STN, SNr, and GP. It should be noted however, that diffusion based tractography cannot infer if a fiber projects onto a structure or passes through it. It might therefore be that some of these reconstructed tracks from the SNc merely traverse through the STN or GP without projecting onto them. Indeed, in a non-human primate tracing study, Sato et al. noticed that projections from the STN to the SNr coursed through the SNc without projecting onto it[191]. However, despite its underappreciation in the functional basal ganglia models, the observed SNc-

7

STN and SNc-GP connections have been previously indirectly demonstrated with tyrosine hydroxylase (TH) stainings in human tissue[46,74]. In line with our study, Cossette et al. showed dopaminergic connections from the SNc that followed the ansa lenticularis to reach the GP at its ventral surface[46]. However, we did not observe the additionally demonstrated connections from the SNc following the lenticular fasciculus[46]. Regarding the fiber organization within the SN, a prominent fiber bundle (bundle K) has been described to run along the caudal border of the SNr, parallel to the cerebral peduncle to bend at the base of the SN[91]. Although this is in line with the main fiber direction that we observed within the SNr, it does not explain the observed SNc-SNr connections. They might arise from unknown connections between the two parts of the SN. In in vivo human studies with 1.5 T or 3 T MRI, it is often difficult to distinguish the SNc from the SNr[126], which renders it difficult to infer their separate connectivity patterns. Sometimes, the identification of these two parts is even performed post hoc, based on their expected projection sites[128,149], which might explain why this connection has not been previously observed with in vivo MRI. Alternatively these SNc-SNr connections might arise from falsely tracked pathways due to partial volume effects; voxels at the borders of a structure likely contain multiple types of tissue or fiber bundles from two distinct but bordering structures. Two other remarkable connections that we observed were the connections of the GPi with the interthalamic adhesion and of the GPi and GPe with the anterior commissure. Both these structures bridge the left and right hemisphere, although the basal ganglia are generally assumed not to have contralateral projections. A few explanations might account for this. One is that the observed fiber tracks represent actual connections that are difficult to observe with histological techniques or that are absent in rodents. Another explanation is that they are the result of falsely tracked fibers. This is indeed supported by the low number of connected fibers and the encapsulation of the anterior commissure by the GP. Finally, the GP, STN, and SN all had connections coursing inferiorly into the brain stem. These fiber tracks were located near the known course of the medial lemniscus. However, the medial lemniscus has been documented to be separate from the basal ganglia, which makes it unlikely for the reconstructed fiber tracks to represent the medial lemniscus. It putatively represents an adjacent bundle connecting to the periphery. However, in the

7

brain stem the fiber paths become denser, hindering both accurate reconstruction as well as accurate identification of the tracks.

7.6 Conclusion

Ultra-high field post mortem MR imaging allowed for reconstructing the connections of the human subthalamic nucleus, substantia nigra and globus pallidus in great detail. In addition to the previously established basal ganglia projections, novel connections were seen as well. The latter may contribute to a more detailed understanding of basal ganglia function.

7.7 Acknowledgements

7

CHAPTER 8

GENERAL DISCUSSION

8.1   Overview

The research described in this thesis aimed to investigate the basal ganglia and their role in Parkinson's disease with ultra-high field MRI. Several studies were employed, focusing on different aspects of this topic. The first study, described in Chapter 4, investigated the potential of ultra-high field MRI for the anatomical visualization of the basal ganglia and related structures. In Chapter 5 this was further expanded by comparing the quantitative MR characteristics of the basal ganglia between Parkinson's disease patients and age-matched controls. Chapter 6 continued by focusing on the subthalamic nucleus (STN) in a study in which we subdivided this nucleus into functional zones in Parkinson's disease patients. Finally, in Chapter 7, the organisation of the network of the basal ganglia was investigated with the aid of high resolution post mortem tractography techniques. These studies illustrate the versatile character of ultra-high field MRI.

8.2   Basal ganglia network

The deeply located STN, substantia nigra (SN), globus pallidus (GP), and striatum, together called the basal ganglia, play an important role in a range of functions including the processing and modulation of motor, limbic, and cognitive actions[151,204]. The way the network is connected has often been described and revised[6,57,156,163,174,175]. Classically, the basal ganglia model consists of the direct and indirect pathway, that act as positive and negative feedback loops respectively, and a hyperdirect pathway (Figure 8.1 A)[6].

Several studies described in this thesis have also investigated connections of the basal ganglia, both at high resolution ex vivo, but also in a population of Parkinson's disease (PD) patients in vivo. In contrast to the often performed histological studies, such as tracing studies in animals that tend to only focus on one aspect, i.e., one pathway, one neurotransmitter, or one 2D slice, the studies described in this thesis focused on the 3D network of multiple basal ganglia connections.

Using 7 T MRI tractography, we were able to consistently identify the hyperdirect pathway in individual PD patients (Figure 8.1 B), with

8

connections from the motor, associative, and limbic cortices to the STN (Chapter 6). This pathway was only later added to the basal ganglia model. Although the corticosubthalamic connection had been described before[89,117,158], it was first characterized as the hyperdirect pathway in 2002 by Nambu et al.[159] and is now becoming a more widely accepted part of the basal ganglia network. It is a fast acting connection that first inhibits all desired and undesired actions, before the direct pathway releases the desired program[159]. In humans, this pathway was later also described with functional MRI[21,100] and tractography[35] studies, but could not always consistently be identified in all subjects. That we were able to identify this pathway consistently in all individual subjects may possibly be explained by the improved visualization and identification of the STN at 7 T and the increased diffusion-weighted spatial resolution.
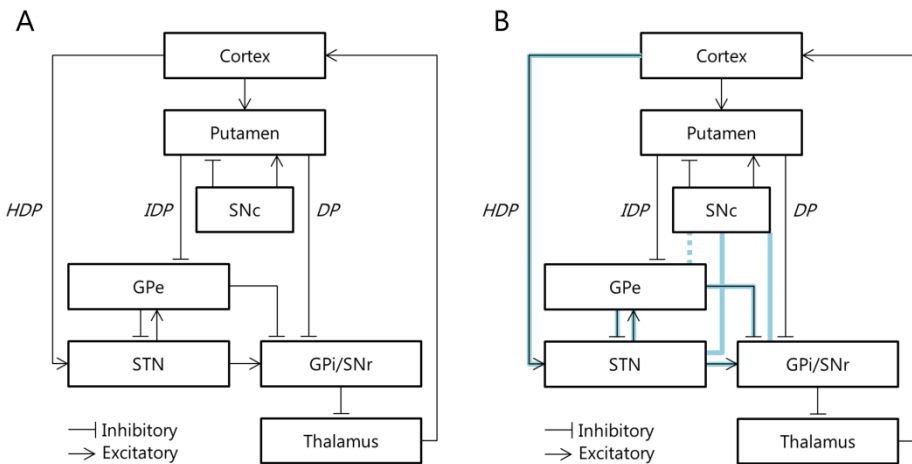
Figure 8.1: Classical basal ganglia model (A), with the connections identified using 7 T human tractography as described in this thesis shown in blue (B). DP = Direct pathway. GPe = External globus pallidus. GPi = Internal globus pallidus. HDP = Hyperdirect pathway. IDP = Indirect pathway. SNc = Substantia nigra pars compacta. SNr = Substantia nigra pars reticulata. STN = Subthalamic nucleus.

In addition to these in vivo connections, we have employed high resolution human post mortem diffusion MRI at 7 T to investigate the connections within the basal ganglia (Chapter 7). These include the connections of the STN to the external globus pallidus (GPe) and the internal globus

pallidus/substantia nigra pars reticulata (GPi/SNr), and the connections of the GPe to the GPi/SNr. Additionally, we observed several connections that are not classically included in the basal ganglia model (Figure 8.1 B). These connections suggest a more prominent role for the substantia nigra pars compacta (SNc), with connections to the STN, GPi/SNr, and to a lesser extend also the GPe. Several competing explanations may account for this. One explanation could be that these are false positives that are inherent to the probabilistic nature of the tractography algorithm, or that they are caused by partial volume effects. Especially the close proximity of the STN and SNr to the SNc could lead to an overrepresentation of their extent of connectivity. However, another explanation could be that these connections really do exists in the human basal ganglia, indicating that the classical model is incomplete and that the SNc does indeed play a more important role than what is currently assumed. These connections may have been unnoticed so far, because the classical model is largely based on findings in animals. Unfortunately diffusion tractography cannot infer information on the directionality of connections or if they are inhibitory or excitatory. Therefore it is difficult to speculate on the neurofunctional meaning of these connections. In any case diffusion MRI, especially when performed at high resolution, shows to be an interesting modality for reinvestigating the subject of the basal ganglia connections at a relatively small scale.

8.3   Subthalamic nucleus

In this thesis the STN, which is a target for deep brain stimulation (DBS) in PD patients, plays a central role. Despite it being a small structure (approximately 125 mm^3), it is involved in a range of functions, including motor, associative, and limbic processing. Several investigations have already focused on the question of how these different functionalities are organized within the STN[8,35,92,121]. There has been debate about whether or not these are organized into neatly segregated clusters, and if so, what the number of clusters should be. However, I do not expect different functional areas to be completely separated from each other. It would be in line with the brain's generally efficient organization for functionalities to interconnect and overlap. Concerning the latter, the number of cluster becomes dependent on the definition of the functions. In our study about the parcellation of the STN (Chapter 6) we found a motor, associative, and

limbic part, but this is also inherent to the definition of the four clusters on the cortex. However, it is not necessarily the number of clusters that is of interest, but rather the location of the functional areas. Which exact functions these are, depends on the question to be answered. For DBS in PD for example, the treatment mainly focusses on the motor symptoms. Therefore in this case, it is important to know the location of the motor area in each individual patient and its overlap with non-motor areas, so as to best suppress the motor symptoms, and prevent side-effects such as cognitive problems and depression[205]. Alternatively, the limbic zone of the STN is a target for DBS in patients with obsessive compulsive disorder (OCD)[139]. In these patients it might be more useful to focus on the locations and overlap of the limbic and non-limbic zones of the STN.

8.4   Clinical perspectives

The basal ganglia play a crucial role in PD. The disease is characterized by the degeneration of dopamine producing neurons in the SNc and dopamine depletion in the putamen and caudate nucleus[198]. That one of the other nuclei, the STN, is a successful target for DBS again underscores the network character of the basal ganglia.

The pathological changes in the parkinsonian brain have been shown difficult to monitor and diagnosis can sometimes only be confirmed post mortem[64]. Biomarkers have been proposed based on genetics[76], proteins[177], and brain imaging[145,178], but have so far not led to standard practice[152]. In Chapter 5 we have shown that part of the PD pathology can be identified in groups of PD patients using 7 T MRI. The altered MR parameters were not only observed in the SN, which have also been observed using 3 T MRI[17,20,65,145,178], but also in the STN, caudate nucleus, and GPi. These alterations can be linked to the concentration of iron and macromolecules and to the microstructure of these nuclei. The investigated populations were small, indicating that the results should be interpreted with care, but this also demonstrates the sensitivity of the technique. Especially the latter is an important prerequisite to be able to draw conclusions from it about individual patients concerning a more accurate diagnosis of the disease, but also monitoring of the disease and evaluation of the treatment. Furthermore the quantitative maps may provide a useful research tool to characterize the

8

diverse spectrum of symptoms associated with PD and to relate this to the disease progression in the brain. Potentially this may also contribute to a more patient-specific treatment, both with medication as well as with DBS.

With the anticipated population aging, the number of PD patients is also expected to increase over the coming years. The demand for efficient and accurate treatment will therefore also grow. Where DBS for PD used to be a last resort treatment, it is now becoming more widely accepted, also for patients with a shorter disease history[196]. Careful patient selection is an important predictor for a successful DBS therapy[34]. Nevertheless, there is still room for improving the clinical outcome and reducing the side-effects of the surgery. The reliable identification of the boundaries of the STN, but also of its motor and non-motor zones, as demonstrated in Chapter 6, can potentially improve DBS through a better prediction of the ideal target location. I hypothesize that using these parcellations for targeting can improve the accuracy and shorten the surgery duration. I expect that the improved accuracy will lead to a better suppression of the symptoms and to a reduction in stimulation induced side-effects, medication use and medication-related side-effects. A shorter surgery duration will impose less burden on the patient and may potentially allow for more patients to receive the surgery. If the targeting is accurate enough, it may potentially also dismiss the need for intraoperative micro-electrode recordings and patient testing, allowing for the surgery to be performed under general anesthesia. This opens the treatment to patients who do not tolerate staying awake during the surgery. However, before these images can actually be applied in clinical practice, their added value first needs to be assessed. An interesting follow up study would be to investigate the relation between the expected target based on 3 T MRI and that based on 7 T anatomical and diffusion-weighted MRI, and to correlate this to the final active contact location as selected after intraoperative micro-electrode recording and patient testing, and postoperative programming. Furthermore, a clinical trial may be performed to assess if the clinical outcome of the surgery does indeed improve if the targeting is performed based on 7 T MRI compared to standard 3 T or atlas-based methods. Outcome measures could be: clinical outcome, for example expressed as Unified Parkinson's Disease Rating Scale (UPDRS) scores, side-effects, and medication use. I anticipate that if this shows targeting based on 7 T MRI to be beneficial over 3 T MRI, this will

8

influence the current practice regarding DBS surgery, especially once 7 T scanners have become clinically available.

The demonstrated options of 7 T MRI and their relevance for PD and DBS also encourage exploration of their use for other applications. One could speculate, for example, on indirect stimulation of the STN through stimulation of its connections with the motor cortex, thereby omitting the need for the insertion of the long lead. However, the observed large surface area of the connected cortex makes stimulating this cortex infeasible and more invasive than current practice DBS. However, another more feasible option is to use the improved identification of deep brain target regions to contribute to the treatment of other diseases. In addition to PD, essential tremor is another prominent indication for DBS, for which accurate targeting of, in this case, the ventral intermediate nucleus of the thalamus, is an important prerequisite. Furthermore, high resolution anatomical imaging and tractography may help DBS for less common indications, such as epilepsy, OCD, and Tourette's syndrome, forward. These indications have less agreement on the optimal target for each individual patient. In OCD for example, both the limbic zone of the STN as well as the ventral capsule/ventral striatum (VC/VS) have been identified as potential targets[83,139]. Being able to visualize the connected regions of each of these targets, may in these cases allow for a better prediction of the optimal target location.

Efforts to improve the outcome of DBS surgery have not only focused on the preoperative planning of the surgery, but also on the postoperative fine-tuning of the stimulated area. New developments involve directional stimulation facilitated by new electrode designs that can be programmed to asymmetrically stimulate its surrounding tissue so as to further fine-tune the volume of tissue activated[45,181]. Another development is the introduction of closed loop stimulation that adapts the stimulation settings automatically and dynamically based on measurements of the patient's clinical state[12]. For example, by predicting the onset of tremor in PD patients, the stimulation paradigm can be adapted to partly compensate for the fluctuations of symptoms[19]. These two interesting developments also benefit from an accurate visualization of the STN's anatomy and can potentially improve the positive effect of more accurate planning even further.

8

8.5   Considerations of ultra-high field MRI

The studies described in this thesis demonstrate the potential value of 7 T MRI for improving the knowledge and treatment of PD. This has, among other things, to do with the improved properties of 7 T MRI, compared to the clinically available field strengths of 1.5 T and 3 T. Depending on the scan protocol, 7 T MRI allows for scanning with a higher resolution, signal-to-noise ratio, contrast-to-noise ratio and/or a shorter scan time. The basal ganglia profit from an added advantage that the sensitivity of MRI to iron also increases with the field strength[229], leading to even better contrast for the iron-rich basal ganglia[87]. Indeed, we showed that even though the quality of the MR images in clinical practice is not always sufficient to use for targeting in DBS, by using 7 T T2* or susceptibility-weighted MRI the boundaries of the STN become sharper and the nucleus can even be distinguished from the SN. Also other small structures become visible at 7 T in vivo MRI, such as the laminae of the GP and substructures of the thalamus and red nucleus[2,56,69] (Chapter 4). This can all be done within relatively short scan times (5-15 minutes), which is an important advantage, since for reasons of logistics and patient comfort, this is a prerequisite for being able to bring it to clinical practice.

However, there is still some skepticism about 7 T MRI, especially when considering its applicability in clinical practice. For one, the scans are more sensitive to geometric distortions and inhomogeneities. Second, its pioneer status also requires adequate safety precautions; the risks of inserting metallic implants in the scanners have been better described for 1.5 T and 3 T scanners than for 7 T scanners. Furthermore, with an increase in resolution, the sensitivity to motion also increases. Many subjects of 7 T MRI research are compliant and experienced MRI researchers, however, the risks for motion will likely only increase in clinical practice, when scanning inexperienced subjects and especially patients with movement disorders. I expect that, considering the developments in the field over the past years, a large number of these concerns will be solved in the coming years. The problems with geometric distortions have already decreased due to the development of optimized scan protocols that compensate for the distortions and due to the development of dedicated hardware such as dielectric pads[202]. The movement artifacts also have better perspectives due to increased experience and research. Scan protocols need to be optimized for

each patient population, plus the introduction of prospective motion correction techniques may solve many of the problems[135]. Also the risks for subjects with metallic implants, that can displace or heat up due to the magnetic field and radio frequency pulses, have to be assessed further to make the technique available to more people. Finally, a sufficient number of 7 T scanners needs to be available to investigate their relevance. However, the scanners will likely only be introduced in clinical practice once their relevance has been demonstrated. Nevertheless, I expect that the availability of 7 T scanners will improve over the coming years, especially now that a clinically approved 7 T scanner is on the way.

8.6   Conclusion

Ultra-high field MRI provides a versatile way of investigating the basal ganglia and their role in Parkinson's disease. It can visualize the basal ganglia in great detail, is sensitive to quantitative MRI properties, and can be used to create a patient-specific parcellation of the STN. This provides good perspective for improving the knowledge about and the treatment of Parkinson's disease.

8

References

1. Abduljalil AM, Schmalbrock P, Novak V, Chakeres DW. Enhanced gray and white matter contrast of phase susceptibility-weighted images in ultra-high-field magnetic resonance imaging. *Journal of magnetic resonance imaging: JMRI* 2003; **18**(3): 284-90.

2. Abosch A, Yacoub E, Ugurbil K, Harel N. An assessment of current brain targets for deep brain stimulation surgery with susceptibility-weighted imaging at 7 tesla. *Neurosurgery* 2010; **67**(6): 1745-56.

3. Ackermans L, Temel Y, Visser-Vandewalle V. Deep brain stimulation in Tourette's syndrome. *Neurotherapeutics* 2008; **5**(2): 339-44.

4. Aggarwal M, Zhang J, Pletnikova O, Crain B, Troncoso J, Mori S. Feasibility of creating a high-resolution 3D diffusion tensor imaging based atlas of the human brainstem: a case study at 11.7 T. *Neuroimage* 2013; **74**: 117-27.

5. Ahsan RL, Allom R, Gousias IS, Habib H, Turkheimer FE, Free S, et al. Volumes, spatial extents and a probabilistic atlas of the human basal ganglia and thalamus. *Neuroimage* 2007; **38**(2): 261-70.

6. Alexander GE, Crutcher MD. Functional architecture of basal ganglia circuits: neural substrates of parallel processing. *Trends Neurosci* 1990; **13**(7): 266-71.

7. Alexander GE, DeLong MR, Strick PL. Parallel organization of functionally segregated circuits linking basal ganglia and cortex. *Annual review of neuroscience* 1986; **9**: 357-81.

8. Alkemade A, Forstmann BU. Do we need to revise the tripartite subdivision hypothesis of the human subthalamic nucleus (STN)? *Neuroimage* 2014; **95**: 326-9.

9. Andersson JL, Skare S, Ashburner J. How to correct susceptibility distortions in spin-echo echo-planar images: application to diffusion tensor imaging. *Neuroimage* 2003; **20**(2): 870-88.

10. Andersson JLR, Jenkinson M, Smith S. Non-linear registration aka Spatial normalisation: FMRIB Centre, Oxford, United Kingdom, 2007.

11. Aravamuthan BR, Muthusamy KA, Stein JF, Aziz TZ, Johansen-Berg H. Topography of cortical and subcortical connections of the human pedunculopontine and subthalamic nuclei. *Neuroimage* 2007; **37**(3): 694-705.

12. Arlotti M, Rosa M, Marceglia S, Barbieri S, Priori A. The adaptive deep brain stimulation challenge. *Parkinsonism Relat Disord* 2016; **28**: 12-7.

13. Arrubla J, Neuner I, Hahn D, Boers F, Shah NJ. Recording visual evoked potentials and auditory evoked P300 at 9.4T static magnetic field. *PLoS One* 2013; **8**(5): e62915.

14. Ashkan K, Blomstedt P, Zrinzo L, Tisch S, Yousry T, Limousin-Dowsey P, et al. Variability of the subthalamic nucleus: The case for direct MRI guided targeting. *British Journal of Neurosurgery* 2007; **21**(2): 197-200.

15. Augustinack JC, van der Kouwe AJ, Blackwell ML, Salat DH, Wiggins CJ, Frosch MP, et al. Detection of entorhinal layer II using 7Tesla [corrected] magnetic resonance imaging. *Ann Neurol* 2005; **57**(4): 489-94.

16. Avecillas-Chasin JM, Alonso-Frech F, Parras O, Del Prado N, Barcia JA. Assessment of a method to determine deep brain stimulation targets using deterministic tractography in a navigation system. *Neurosurg Rev* 2015; **38**(4): 739-51.

17. Barbosa JH, Santos AC, Tumas V, Liu M, Zheng W, Haacke EM, et al. Quantifying brain iron deposition in patients with Parkinson's disease using quantitative susceptibility mapping, R2 and R2. *Magn Reson Imaging* 2015; **33**(5): 559-65.

18. Basser PJ, Pajevic S, Pierpaoli C, Duda J, Aldroubi A. In vivo fiber tractography using DT-MRI data. *Magn Reson Med* 2000; **44**(4): 625-32.

19. Basu I, Graupe D, Tuninetti D, Shukla P, Slavin KV, Metman LV, et al. Pathological tremor prediction using surface electromyogram and acceleration: potential use in 'ON-OFF' demand driven deep brain stimulator design. *Journal of neural engineering* 2013; **10**(3): 036019.

20. Baudrexel S, Nurnberger L, Rub U, Seifried C, Klein JC, Deller T, et al. Quantitative mapping of T1 and T2* discloses nigral and brainstem pathology in early Parkinson's disease. *Neuroimage* 2010; **51**(2): 512-20.

21. Baudrexel S, Witte T, Seifried C, von Wegner F, Beissner F, Klein JC, et al. Resting state fMRI reveals increased subthalamic nucleus-motor cortex connectivity in Parkinson's disease. *Neuroimage* 2011; **55**(4): 1728-38.

22. Behrens TE, Berg HJ, Jbabdi S, Rushworth MF, Woolrich MW. Probabilistic diffusion tractography with multiple fibre orientations: What can we gain? *Neuroimage* 2007; **34**(1): 144-55.

23. Behrens TE, Johansen-Berg H, Woolrich MW, Smith SM, Wheeler-Kingshott CA, Boulby PA, et al. Non-invasive mapping of connections between human thalamus and cortex using diffusion imaging. *Nat Neurosci* 2003; **6**(7): 750-7.

24. Benabid AL, Chabardes S, Mitrofanis J, Pollak P. Deep brain stimulation of the subthalamic nucleus for the treatment of Parkinson's disease. *Lancet Neurol* 2009; **8**(1): 67-81.

25. Benazzouz A, Gross C, Feger J, Boraud T, Bioulac B. Reversal of rigidity and improvement in motor performance by subthalamic high-frequency stimulation in MPTP-treated monkeys. *Eur J Neurosci* 1993; **5**(4): 382-9.

26. Bender B, Klose U. The in vivo influence of white matter fiber orientation towards B(0) on T2* in the human brain. *NMR Biomed* 2010; **23**(9): 1071-6.

27. Bender B, Manz C, Korn A, Nagele T, Klose U. Optimized 3D magnetization-prepared rapid acquisition of gradient echo: identification of thalamus substructures at 3T. *AJNR Am J Neuroradiol* 2011; **32**(11): 2110-5.

28. Bergman H, Wichmann T, Karmon B, DeLong MR. The primate subthalamic nucleus. II. Neuronal activity in the MPTP model of parkinsonism. *J Neurophysiol* 1994; **72**(2): 507-20.

29. Berrington A, Jezzard P, Clare S, Emir U. Two-voxel Hadamard encoded semi-LASER spectroscopy for in vivo MRS at ultra-high field. Joint Annual Meeting ISMRM-ESMRMB; 2014; Milan, Italy; 2014.

30. Bhagat YA, Rajapakse CS, Magland JF, Love JH, Wright AC, Wald MJ, et al. Performance of muMRI-Based virtual bone biopsy for structural and mechanical analysis at the distal tibia at 7T field strength. *J Magn Reson Imaging* 2011; **33**(2): 372-81.

31. Boulant N, Cloos MA, Amadon A. B1 and B0 inhomogeneity mitigation in the human brain at 7 T with selective pulses by using average Hamiltonian theory. *Magn Reson Med* 2011; **65**(3): 680-91.

32. Bourekas EC, Christoforidis GA, Abduljalil AM, Kangarlu A, Chakeres DW, Spigos DG, et al. High resolution MRI of the deep gray nuclei at 8 Tesla. *J Comput Assist Tomogr* 1999; **23**(6): 867-74.

33. Braak H, Del Tredici K. Cortico-basal ganglia-cortical circuitry in Parkinson's disease reconsidered. *Exp Neurol* 2008; **212**(1): 226-9.

34. Bronstein JM, Tagliati M, Alterman RL, Lozano AM, Volkmann J, Stefani A, et al. Deep brain stimulation for Parkinson disease: an expert consensus and review of key issues. *Arch Neurol* 2011; **68**(2): 165.

35. Brunenberg EJ, Moeskops P, Backes WH, Pollo C, Cammoun L, Vilanova A, et al. Structural and resting state functional connectivity of the subthalamic nucleus: identification of motor STN parts and the hyperdirect pathway. *PLoS One* 2012; **7**(6): e39061.

36. Brunenberg EJ, Platel B, Hofman PA, Ter Haar Romeny BM, Visser-Vandewalle V. Magnetic resonance imaging techniques for visualization of the subthalamic nucleus. *Journal of neurosurgery* 2011; **115**(5): 971-84.

37. Budde J, Shajan G, Scheffler K, Pohmann R. Ultra-high resolution imaging of the human brain using acquisition-weighted imaging at 9.4T. *Neuroimage* 2014; **86**: 592-8.

38. Buxton RB. The physics of functional magnetic resonance imaging (fMRI). *Reports on progress in physics Physical Society (Great Britain)* 2013; **76**(9): 096601.

39. Calabrese E, Hickey P, Hulette C, Zhang J, Parente B, Lad SP, et al. Postmortem diffusion MRI of the human brainstem and thalamus for deep brain stimulator electrode localization. *Hum Brain Mapp* 2015; **36**(8): 3167-78.

40. Calamante F, Oh SH, Tournier JD, Park SY, Son YD, Chung JY, et al. Super-resolution track-density imaging of thalamic substructures: Comparison with high-resolution anatomical magnetic resonance imaging at 7.0T. *Human brain mapping* 2012.

41. Carpenter MB, Peter P. Nigrostriatal and nigrothalamic fibers in the rhesus monkey. *The Journal of comparative neurology* 1972; **144**(1): 93-115.

42. Cho Z-H, Kim Y-B, Han J-Y, Min H-K, Kim K-N, Choi S-H, et al. New brain atlas—Mapping the human brain in vivo with 7.0 T MRI and comparison with postmortem histology: Will these images change modern medicine? *International Journal of Imaging Systems and Technology* 2008; **18**(1): 2-8.

43. Cho ZH, Min HK, Oh SH, Han JY, Park CW, Chi JG, et al. Direct visualization of deep brain stimulation targets in Parkinson disease with the use of 7-tesla magnetic resonance imaging. *Journal of neurosurgery* 2010; **113**(3): 639-47.

44. Cloos M, Wiggins C, Wiggins G, Sodickson D. Plug and Play Parallel Transmission at 7 and 9.4 Tesla Based on Principles from MR Fingerprinting. Joint Annual Meeting ISMRM-ESMRMB; 2014; Milan, Italy; 2014.

45. Contarino MF, Bour LJ, Verhagen R, Lourens MA, de Bie RM, van den Munckhof P, et al. Directional steering: A novel approach to deep brain stimulation. *Neurology* 2014; **83**(13): 1163-9.

46. Cossette M, Lévesque M, Parent A. Extrastriatal dopaminergic innervation of human basal ganglia. *Neuroscience Research* 1999; **34**(1): 51-4.

47. Costagli M, Kelley DA, Symms MR, Biagi L, Stara R, Maggioni E, et al. Tissue Border Enhancement by inversion recovery MRI at 7.0 Tesla. *Neuroradiology* 2014; **56**(7): 517-23.

48.   D'Arceuil HE, Westmoreland S, de Crespigny AJ. An approach to high resolution diffusion tensor imaging in fixed primate brain. *Neuroimage* 2007; **35**(2): 553-65.

49.   Damier P, Thobois S, Witjas T, Cuny E, Derost P, Raoul S, et al. Bilateral deep brain stimulation of the globus pallidus to treat tardive dyskinesia. *Arch Gen Psychiatry* 2007; **64**(2): 170-6.

50.   Dammann P, Kraff O, Wrede KH, Ozkan N, Orzada S, Mueller OM, et al. Evaluation of hardware-related geometrical distortion in structural MRI at 7 Tesla for image-guided applications in neurosurgery. *Acad Radiol* 2011; **18**(7): 910-6.

51.   de Bresser J, Brundel M, Conijn MM, van Dillen JJ, Geerlings MI, Viergever MA, et al. Visual cerebral microbleed detection on 7T MR imaging: reliability and effects of image processing. *AJNR Am J Neuroradiol* 2013; **34**(6): E61-4.

52.   de Zwart JA, Ledden PJ, van Gelderen P, Bodurka J, Chu R, Duyn JH. Signal-to-noise ratio and parallel imaging performance of a 16-channel receive-only brain coil array at 3.0 Tesla. *Magn Reson Med* 2004; **51**(1): 22-6.

53.   Deelchand DK, Van de Moortele PF, Adriany G, Iltis I, Andersen P, Strupp JP, et al. In vivo 1H NMR spectroscopy of the human brain at 9.4 T: initial results. *Journal of magnetic resonance (San Diego, Calif: 1997)* 2010; **206**(1): 74-80.

54.   Deep-Brain Stimulation for Parkinson's Disease Study Group. Deep-brain stimulation of the subthalamic nucleus or the pars interna of the globus pallidus in Parkinson's disease. *N Engl J Med* 2001; **345**(13): 956-63.

55.   Deistung A, Schafer A, Schweser F, Biedermann U, Gullmar D, Trampel R, et al. High-Resolution MR Imaging of the Human Brainstem In vivo at 7 Tesla. *Front Hum Neurosci* 2013; **7**: 710.

56.   Deistung A, Schafer A, Schweser F, Biedermann U, Turner R, Reichenbach JR. Toward in vivo histology: a comparison of quantitative susceptibility mapping (QSM) with magnitude-, phase-,

and R2*-imaging at ultra-high magnetic field strength. *Neuroimage* 2013; **65**: 299-314.

57.   DeLong MR, Wichmann T. Circuits and circuit disorders of the basal ganglia. *Arch Neurol* 2007; **64**(1): 20-4.

58.   Denney TS, Bolding M, Beyers R, Salibi N, Li M, Zhang X, et al. Differential Motion In Orbital And Global Layers Of Extraocular Muscles Measured By Tagged MRI At 7T. Joint Annual Meeting ISMRM-ESMRMB. Milan, Italy; 2014.

59.   Denys D, Mantione M, Figee M, van den Munckhof P, Koerselman F, Westenberg H, et al. Deep brain stimulation of the nucleus accumbens for treatment-refractory obsessive-compulsive disorder. *Arch Gen Psychiatry* 2010; **67**(10): 1061-8.

60.   Desikan RS, Segonne F, Fischl B, Quinn BT, Dickerson BC, Blacker D, et al. An automated labeling system for subdividing the human cerebral cortex on MRI scans into gyral based regions of interest. *Neuroimage* 2006; **31**(3): 968-80.

61.   Deuschl G, Schade-Brittinger C, Krack P, Volkmann J, Schafer H, Botzel K, et al. A randomized trial of deep-brain stimulation for Parkinson's disease. *N Engl J Med* 2006; **355**(9): 896-908.

62.   Di Lorenzo Alho AT, Suemoto CK, Polichiso L, Tampellini E, de Oliveira KC, Molina M, et al. Three-dimensional and stereological characterization of the human substantia nigra during aging. *Brain structure & function* 2015.

63.   Di Martino A, Scheres A, Margulies DS, Kelly AM, Uddin LQ, Shehzad Z, et al. Functional connectivity of human striatum: a resting state FMRI study. *Cerebral cortex (New York, NY: 1991)* 2008; **18**(12): 2735-47.

64.   Dickson DW, Braak H, Duda JE, Duyckaerts C, Gasser T, Halliday GM, et al. Neuropathological assessment of Parkinson's disease: refining the diagnostic criteria. *The Lancet Neurology* 2009; **8**(12): 1150-7.

65.   Du G, Liu T, Lewis MM, Kong L, Wang Y, Connor J, et al. Quantitative susceptibility mapping of the midbrain in Parkinson's

disease. *Movement disorders: official journal of the Movement Disorder Society* 2015.

66.   Duchin Y, Abosch A, Yacoub E, Sapiro G, Harel N. Feasibility of using ultra-high field (7 T) MRI for clinical surgical targeting. *PLoS One* 2012; **7**(5): e37328.

67.   Duyn JH. The future of ultra-high field MRI and fMRI for study of the human brain. *Neuroimage* 2012; **62**(2): 1241-8.

68.   Dzyubachyk O, Lelieveldt BP, Blaas J, Reijnierse M, Webb A, van der Geest RJ. Automated algorithm for reconstruction of the complete spine from multistation 7T MR data. *Magn Reson Med* 2013; **69**(6): 1777-86.

69.   Eapen M, Zald DH, Gatenby JC, Ding Z, Gore JC. Using high-resolution MR imaging at 7T to evaluate the anatomy of the midbrain dopaminergic system. *AJNR Am J Neuroradiol* 2011; **32**(4): 688-94.

70.   Fearnley JM, Lees AJ. Ageing and Parkinson's disease: substantia nigra regional selectivity. *Brain* 1991; **114 (Pt 5)**: 2283-301.

71.   Fisher R, Salanova V, Witt T, Worth R, Henry T, Gross R, et al. Electrical stimulation of the anterior nucleus of thalamus for treatment of refractory epilepsy. *Epilepsia* 2010; **51**(5): 899-908.

72.   Follett KA, Torres-Russotto D. Deep brain stimulation of globus pallidus interna, subthalamic nucleus, and pedunculopontine nucleus for Parkinson's disease: which target? *Parkinsonism & related disorders* 2012; **18 Suppl 1**: S165-7.

73.   Foroutan P, Murray ME, Fujioka S, Schweitzer KJ, Dickson DW, Wszolek ZK, et al. Progressive supranuclear palsy: high-field-strength MR microscopy in the human substantia nigra and globus pallidus. *Radiology* 2013; **266**(1): 280-8.

74.   Francois C, Savy C, Jan C, Tande D, Hirsch EC, Yelnik J. Dopaminergic innervation of the subthalamic nucleus in the normal state, in MPTP-treated monkeys, and in Parkinson's disease patients. *The Journal of comparative neurology* 2000; **425**(1): 121-9.

75.   Gaitan MI, Sati P, Inati SJ, Reich DS. Initial investigation of the blood-brain barrier in MS lesions at 7 tesla. *Multiple sclerosis (Houndmills, Basingstoke, England)* 2013; **19**(8): 1068-73.

76.   Gasser T. Genomic and proteomic biomarkers for Parkinson disease. *Neurology* 2009; **72**(7 Suppl): S27-31.

77.   Gerfen CR. The neostriatal mosaic. I. compartmental organization of projections from the striatum to the substantia nigra in the rat. *The Journal of comparative neurology* 1985; **236**(4): 454-76.

78.   Glover PM, Cavin I, Qian W, Bowtell R, Gowland PA. Magnetic-field-induced vertigo: a theoretical and experimental investigation. *Bioelectromagnetics* 2007; **28**(5): 349-61.

79.   Goetz CG, Tilley BC, Shaftman SR, Stebbins GT, Fahn S, Martinez-Martin P, et al. Movement Disorder Society-sponsored revision of the Unified Parkinson's Disease Rating Scale (MDS-UPDRS): scale presentation and clinimetric testing results. *Movement disorders: official journal of the Movement Disorder Society* 2008; **23**(15): 2129-70.

80.   Gotz ME, Double K, Gerlach M, Youdim MB, Riederer P. The relevance of iron in the pathogenesis of Parkinson's disease. *Ann N Y Acad Sci* 2004; **1012**: 193-208.

81.   Goubran M, Rudko DA, Santyr B, Gati J, Szekeres T, Peters TM, et al. In vivo normative atlas of the hippocampal subfields using multi-echo susceptibility imaging at 7 Tesla. *Hum Brain Mapp* 2014; **35**(8): 3588-601.

82.   Grabner G, Janke A, Budge M, Smith D, Pruessner J, Collins DL. Symmetric Atlasing and Model Based Segmentation: An Application to the Hippocampus in Older Adults. In: Larsen R, Nielsen M, Sporring J, eds. Medical Image Computing and Computer-Assisted Intervention – MICCAI 2006: Springer Berlin Heidelberg; 2006: 58-66.

83.   Greenberg BD, Gabriels LA, Malone DA, Jr., Rezai AR, Friehs GM, Okun MS, et al. Deep brain stimulation of the ventral internal capsule/ventral striatum for obsessive-compulsive disorder: worldwide experience. *Mol Psychiatry* 2010; **15**(1): 64-79.

84.   Grill WM, Snyder AN, Miocinovic S. Deep brain stimulation creates an informational lesion of the stimulated nucleus. *Neuroreport* 2004; **15**(7): 1137-40.

85.   Haacke EM, Reichenbach JR. Susceptibility Weighted Imaging in MRI: Basic Concepts and Clinical Applications: Wiley; 2011.

86.   Haase A, Frahm J, Matthaei D, Hanicke W, Merboldt KD. FLASH imaging: rapid NMR imaging using low flip-angle pulses. 1986. *Journal of magnetic resonance (San Diego, Calif: 1997)* 2011; **213**(2): 533-41.

87.   Hallgren B, Sourander P. The effect of age on the non-haemin iron in the human brain. *J Neurochem* 1958; **3**(1): 41-51.

88.   Hamani C, Temel Y. Deep brain stimulation for psychiatric disease: contributions and validity of animal models. *Sci Transl Med* 2012; **4**(142): 142rv8.

89.   Hartmann-von Monakow K, Akert K, Künzle H. Projections of the precentral motor cortex and other cortical areas of the frontal lobe to the subthalamic nucleus in the monkey. *Experimental Brain Research* 1978; **33**(3): 395-403.

90.   Hashimoto T, Elder CM, Okun MS, Patrick SK, Vitek JL. Stimulation of the subthalamic nucleus changes the firing pattern of pallidal neurons. *J Neurosci* 2003; **23**(5): 1916-23.

91.   Hassler R. Zur Normalanatomie der Substantia nigra. Versuch einer architektonischen Gliederung. *J Psychol Neurol* 1937; **48**(1-2): 1-55.

92.   Haynes WI, Haber SN. The organization of prefrontal-subthalamic inputs in primates provides an anatomical substrate for both functional specificity and integration: implications for basal ganglia models and deep brain stimulation. *J Neurosci* 2013; **33**(11): 4804-14.

93.   He L, Zuo Z, Chen L, Humphreys G. Effects of Number Magnitude and Notation at 7T: Separating the Neural Response to Small and Large, Symbolic and Nonsymbolic Number. *Cerebral cortex (New York, NY: 1991)* 2014; **24**(8): 2199-209.

94.   Hennig J, Nauerth A, Friedburg H. RARE imaging: a fast imaging method for clinical MR. *Magn Reson Med* 1986; **3**(6): 823-33.

95. Hershey T, Revilla FJ, Wernle AR, McGee-Minnich L, Antenor JV, Videen TO, et al. Cortical and subcortical blood flow effects of subthalamic nucleus stimulation in PD. *Neurology* 2003; **61**(6): 816-21.

96. Hoover JE, Strick PL. Multiple output channels in the basal ganglia. *Science (New York, NY)* 1993; **259**(5096): 819-21.

97. Hornykiewicz O. Chemical neuroanatomy of the basal ganglia — normal and in Parkinson's disease. *Journal of Chemical Neuroanatomy* 2001; **22**(1–2): 3-12.

98. Intrapiromkul J, Zhu H, Cheng Y, Barker PB, Edden RA. Determining the in vivo transverse relaxation time of GABA in the human brain at 7T. *J Magn Reson Imaging* 2013; **38**(5): 1224-9.

99. Ivanov D, Poser B, Huber L, Pfeuffer J, Uludağ K. Whole-Brain Perfusion Measurements at 7T Using Pulsed Arterial Spin Labelling and Simultaneous Multi-Slice Multi-Echo Echo Planar Imaging. Joint Annual Meeting ISMRM-ESMRMB; 2014; Milan, Italy; 2014.

100. Jahfari S, Waldorp L, van den Wildenberg WPM, Scholte HS, Ridderinkhof KR, Forstmann BU. Effective connectivity reveals important roles for both the hyperdirect (fronto-subthalamic) and the indirect (fronto-striatal-pallidal) fronto-basal ganglia pathways during response inhibition. *J Neurosci* 2011; **31**(18): 6891-9.

101. Jenkinson M, Bannister P, Brady M, Smith S. Improved optimization for the robust and accurate linear registration and motion correction of brain images. *Neuroimage* 2002; **17**(2): 825-41.

102. Jenkinson M, Beckmann CF, Behrens TE, Woolrich MW, Smith SM. FSL. *Neuroimage* 2012; **62**(2): 782-90.

103. Kabasawa H, Nabetani A, Matsuzawa H, Nakada T. Imaging optimization for in-vivo human micro imaging at 7T. Joint Annual Meeting ISMRM-ESMRMB; 2006; 2006.

104. Kalia LV, Lang AE. Parkinson's disease. *Lancet (London, England)* 2015; **386**(9996): 896-912.

105. Kanowski M, Voges J, Tempelmann C. Delineation of the nucleus centre median by proton density weighted magnetic resonance

imaging at 3 T. *Neurosurgery* 2010; **66**(3 Suppl Operative): E121-3; discussion E3.

106.   Karachi C, Grabli D, Baup N, Mounayar S, Tande D, Francois C, et al. Dysfunction of the subthalamic nucleus induces behavioral and movement disorders in monkeys. *Mov Disord* 2009; **24**(8): 1183-92.

107.   Karachi C, Yelnik J, Tande D, Tremblay L, Hirsch EC, Francois C. The pallidosubthalamic projection: an anatomical substrate for nonmotor functions of the subthalamic nucleus in primates. *Mov Disord* 2005; **20**(2): 172-80.

108.   Kefalopoulou Z, Zrinzo L, Jahanshahi M, Candelario J, Milabo C, Beigi M, et al. Bilateral globus pallidus stimulation for severe Tourette's syndrome: a double-blind, randomised crossover trial. *Lancet Neurol* 2015; **14**(6): 595-605.

109.   Kerchner GA, Deutsch GK, Zeineh M, Dougherty RF, Saranathan M, Rutt BK. Hippocampal CA1 apical neuropil atrophy and memory performance in Alzheimer's disease. *Neuroimage* 2012; **63**(1): 194-202.

110.   Kerl HU, Gerigk L, Brockmann MA, Huck S, Al-Zghloul M, Groden C, et al. Imaging for deep brain stimulation: The zona incerta at 7 Tesla. *World J Radiol* 2013; **5**(1): 5-16.

111.   Kerl HU, Gerigk L, Huck S, Al-Zghloul M, Groden C, Nolte IS. Visualisation of the zona incerta for deep brain stimulation at 3.0 Tesla. *Clin Neuroradiol* 2012; **22**(1): 55-68.

112.   Kerl HU, Gerigk L, Pechlivanis I, Al-Zghloul M, Groden C, Nolte I. The subthalamic nucleus at 3.0 Tesla: choice of optimal sequence and orientation for deep brain stimulation using a standard installation protocol: clinical article. *Journal of neurosurgery* 2012; **117**(6): 1155-65.

113.   Kerl HU, Gerigk L, Pechlivanis I, Al-Zghloul M, Groden C, Nölte IS. The subthalamic nucleus at 7.0 Tesla: evaluation of sequence and orientation for deep-brain stimulation. *Acta Neurochir (Wien)* 2012.

114.   Keuken MC, Uylings HB, Geyer S, Schafer A, Turner R, Forstmann BU. Are there three subdivisions in the primate subthalamic nucleus? *Front Neuroanat* 2012; **6**: 14.

115. Kickler N, van der Zwaag W, Mekle R, Kober T, Marques JP, Krueger G, et al. Eddy current effects on a clinical 7T-68 cm bore scanner. *MAGMA* 2010; **23**(1): 39-43.

116. Kita H, Tachibana Y, Nambu A, Chiken S. Balance of monosynaptic excitatory and disynaptic inhibitory responses of the globus pallidus induced after stimulation of the subthalamic nucleus in the monkey. *J Neurosci* 2005; **25**(38): 8611-9.

117. Kitai ST, Deniau JM. Cortical inputs to the subthalamus: intracellular analysis. *Brain Res* 1981; **214**(2): 411-5.

118. Kleiner-Fisman G, Herzog J, Fisman DN, Tamma F, Lyons KE, Pahwa R, et al. Subthalamic nucleus deep brain stimulation: summary and meta-analysis of outcomes. *Movement disorders: official journal of the Movement Disorder Society* 2006; **21 Suppl 14**: S290-304.

119. Kocabicak E, Temel Y. Deep brain stimulation of the subthalamic nucleus in Parkinson's disease: surgical technique, tips, tricks and complications. *Clinical neurology and neurosurgery* 2013; **115**(11): 2318-23.

120. Kordower JH, Olanow CW, Dodiya HB, Chu Y, Beach TG, Adler CH, et al. Disease duration and the integrity of the nigrostriatal system in Parkinson's disease. *Brain* 2013; **136**(Pt 8): 2419-31.

121. Lambert C, Zrinzo L, Nagy Z, Lutti A, Hariz M, Foltynie T, et al. Confirmation of functional zones within the human subthalamic nucleus: patterns of connectivity and sub-parcellation using diffusion weighted imaging. *Neuroimage* 2012; **60**(1): 83-94.

122. Lambert C, Zrinzo L, Nagy Z, Lutti A, Hariz M, Foltynie T, et al. Do we need to revise the tripartite subdivision hypothesis of the human subthalamic nucleus (STN)? Response to Alkemade and Forstmann. *Neuroimage* 2015; **110**: 1-2.

123. Le Bihan D. Looking into the functional architecture of the brain with diffusion MRI. *Nature reviews Neuroscience* 2003; **4**(6): 469-80.

124. Lee JY, Deogaonkar M, Rezai A. Deep brain stimulation of globus pallidus internus for dystonia. *Parkinsonism & related disorders* 2007; **13**(5): 261-5.

125. Lefaucheur JP. Principles of therapeutic use of transcranial and epidural cortical stimulation. *Clinical neurophysiology: official journal of the International Federation of Clinical Neurophysiology* 2008; **119**(10): 2179-84.

126. Lehericy S, Bardinet E, Poupon C, Vidailhet M, Francois C. 7 Tesla magnetic resonance imaging: a closer look at substantia nigra anatomy in Parkinson's disease. *Movement disorders: official journal of the Movement Disorder Society* 2014; **29**(13): 1574-81.

127. Lehericy S, Bardinet E, Tremblay L, Van de Moortele PF, Pochon JB, Dormont D, et al. Motor control in basal ganglia circuits using fMRI and brain atlas approaches. *Cerebral cortex (New York, NY: 1991)* 2006; **16**(2): 149-61.

128. Lenglet C, Abosch A, Yacoub E, De Martino F, Sapiro G, Harel N. Comprehensive in vivo mapping of the human basal ganglia and thalamic connectome in individuals using 7T MRI. *PLoS One* 2012; **7**(1): e29153.

129. Limousin P, Martinez-Torres I. Deep brain stimulation for Parkinson's disease. *Neurotherapeutics* 2008; **5**(2): 309-19.

130. Limousin P, Pollak P, Benazzouz A, Hoffmann D, Le Bas JF, Broussolle E, et al. Effect of parkinsonian signs and symptoms of bilateral subthalamic nucleus stimulation. *Lancet (London, England)* 1995; **345**(8942): 91-5.

131. Liu T, Eskreis-Winkler S, Schweitzer AD, Chen W, Kaplitt MG, Tsiouris AJ, et al. Improved Subthalamic Nucleus Depiction with Quantitative Susceptibility Mapping. *Radiology* 2013.

132. Lotfipour AK, Wharton S, Schwarz ST, Gontu V, Schafer A, Peters AM, et al. High resolution magnetic susceptibility mapping of the substantia nigra in Parkinson's disease. *Journal of magnetic resonance imaging: JMRI* 2012; **35**(1): 48-55.

133. Lozano AM, Dostrovsky J, Chen R, Ashby P. Deep brain stimulation for Parkinson's disease: disrupting the disruption. *Lancet Neurol* 2002; **1**(4): 225-31.

134. Lu A, Atkinson IC, Zhou XJ, Thulborn KR. PCr/ATP ratio mapping of the human head by simultaneously imaging of multiple spectral peaks with interleaved excitations and flexible twisted projection imaging readout trajectories at 9.4 T. *Magn Reson Med* 2013; **69**(2): 538-44.

135. Maclaren J, Herbst M, Speck O, Zaitsev M. Prospective motion correction in brain imaging: a review. *Magn Reson Med* 2013; **69**(3): 621-36.

136. Mai JK, Paxinos G, Voss T. Atlas of the Human Brain: Academic Press; 2008.

137. Mai JK, Stephens PH, Hopf A, Cuello AC. Substance P in the human brain. *Neuroscience* 1986; **17**(3): 709-39.

138. Maia TV, Cooney RE, Peterson BS. The neural bases of obsessive-compulsive disorder in children and adults. *Dev Psychopathol* 2008; **20**(4): 1251-83.

139. Mallet L, Polosan M, Jaafari N, Baup N, Welter ML, Fontaine D, et al. Subthalamic nucleus stimulation in severe obsessive-compulsive disorder. *N Engl J Med* 2008; **359**(20): 2121-34.

140. Mallet L, Schupbach M, N'Diaye K, Remy P, Bardinet E, Czernecki V, et al. Stimulation of subterritories of the subthalamic nucleus reveals its role in the integration of the emotional and motor aspects of behavior. *Proceedings of the National Academy of Sciences of the United States of America* 2007; **104**(25): 10661-6.

141. Malone DA, Jr., Dougherty DD, Rezai AR, Carpenter LL, Friehs GM, Eskandar EN, et al. Deep brain stimulation of the ventral capsule/ventral striatum for treatment-resistant depression. *Biological psychiatry* 2009; **65**(4): 267-75.

142. Mang SC, Busza A, Reiterer S, Grodd W, Klose AU. Thalamus segmentation based on the local diffusion direction: a group study. *Magn Reson Med* 2012; **67**(1): 118-26.

143. Markram H. The blue brain project. *Nature reviews Neuroscience* 2006; **7**(2): 153-60.

144. Marques JP, Kober T, Krueger G, van der Zwaag W, Van de Moortele PF, Gruetter R. MP2RAGE, a self bias-field corrected sequence for improved segmentation and T1-mapping at high field. *Neuroimage* 2010; **49**(2): 1271-81.

145. Martin WR, Wieler M, Gee M. Midbrain iron content in early Parkinson disease: a potential biomarker of disease status. *Neurology* 2008; **70**(16 Pt 2): 1411-7.

146. Massey LA, Miranda MA, Zrinzo L, Al-Helli O, Parkes HG, Thornton JS, et al. High resolution MR anatomy of the subthalamic nucleus: imaging at 9.4 T with histological validation. *Neuroimage* 2012; **59**(3): 2035-44.

147. Mayka MA, Corcos DM, Leurgans SE, Vaillancourt DE. Three-dimensional locations and boundaries of motor and premotor cortices as defined by functional brain imaging: a meta-analysis. *Neuroimage* 2006; **31**(4): 1453-74.

148. Meissner W, Leblois A, Hansel D, Bioulac B, Gross CE, Benazzouz A, et al. Subthalamic high frequency stimulation resets subthalamic firing and reduces abnormal oscillations. *Brain* 2005; **128**(Pt 10): 2372-82.

149. Menke RA, Jbabdi S, Miller KL, Matthews PM, Zarei M. Connectivity-based segmentation of the substantia nigra in human and its implications in Parkinson's disease. *NeuroImage* 2010; **52**(4): 1175-80.

150. Metcalf M, Xu D, Okuda DT, Carvajal L, Srinivasan R, Kelley DA, et al. High-resolution phased-array MRI of the human brain at 7 tesla: initial experience in multiple sclerosis patients. *Journal of neuroimaging: official journal of the American Society of Neuroimaging* 2010; **20**(2): 141-7.

151. Middleton FA, Strick PL. Basal ganglia and cerebellar loops: motor and cognitive circuits. *Brain research Brain research reviews* 2000; **31**(2-3): 236-50.

152. Miller DB, O'Callaghan JP. Biomarkers of Parkinson's disease: present and future. *Metabolism: clinical and experimental* 2015; **64**(3 Suppl 1): S40-6.

153. Mink JW. Neurobiology of basal ganglia and Tourette syndrome: basal ganglia circuits and thalamocortical outputs. *Adv Neurol* 2006; **99**: 89-98.

154. Moon CH, Kim JH, Zhao T, Bae KT. Quantitative (23) Na MRI of human knee cartilage using dual-tuned (1) H/(23) Na transceiver array radiofrequency coil at 7 tesla. *J Magn Reson Imaging* 2013; **38**(5): 1063-72.

155. Morris DM, Embleton KV, Parker GJM. Probabilistic fibre tracking: Differentiation of connections from chance events. *NeuroImage* 2008; **42**(4): 1329-39.

156. Nambu A. Somatotopic organization of the primate Basal Ganglia. *Front Neuroanat* 2011; **5**: 26.

157. Nambu A, Tokuno H, Hamada I, Kita H, Imanishi M, Akazawa T, et al. Excitatory cortical inputs to pallidal neurons via the subthalamic nucleus in the monkey. *J Neurophysiol* 2000; **84**(1): 289-300.

158. Nambu A, Tokuno H, Inase M, Takada M. Corticosubthalamic input zones from forelimb representations of the dorsal and ventral divisions of the premotor cortex in the macaque monkey: comparison with the input zones from the primary motor cortex and the supplementary motor area. *Neurosci Lett* 1997; **239**(1): 13-6.

159. Nambu A, Tokuno H, Takada M. Functional significance of the cortico-subthalamo-pallidal 'hyperdirect' pathway. *Neurosci Res* 2002; **43**(2): 111-7.

160. Nauta WJH, Mehler WR. Projections of the lentiform nucleus in the monkey. *Brain Research* 1966; **1**(1): 3-42.

161. Nolte IS, Gerigk L, Al-Zghloul M, Groden C, Kerl HU. Visualization of the internal globus pallidus: sequence and orientation for deep brain stimulation using a standard installation protocol at 3.0 Tesla. *Acta neurochirurgica* 2012; **154**(3): 481-94.

162. Novak P, Novak V, Kangarlu A, Abduljalil AM, Chakeres DW, Robitaille PM. High resolution MRI of the brainstem at 8 T. *J Comput Assist Tomogr* 2001; **25**(2): 242-6.

163. Obeso JA, Marin C, Rodriguez-Oroz C, Blesa J, Benitez-Temino B, Mena-Segovia J, et al. The basal ganglia in Parkinson's disease: current concepts and unexplained observations. *Annals of neurology* 2008; **64 Suppl 2**: S30-46.

164. Obeso JA, Rodriguez-Oroz MC, Stamelou M, Bhatia KP, Burn DJ. The expanding universe of disorders of the basal ganglia. *Lancet (London, England)* 2014; **384**(9942): 523-31.

165. Odekerken VJ, van Laar T, Staal MJ, Mosch A, Hoffmann CF, Nijssen PC, et al. Subthalamic nucleus versus globus pallidus bilateral deep brain stimulation for advanced Parkinson's disease (NSTAPS study): a randomised controlled trial. *Lancet Neurol* 2013; **12**(1): 37-44.

166. Oh MY, Abosch A, Kim SH, Lang AE, Lozano AM. Long-term hardware-related complications of deep brain stimulation. *Neurosurgery* 2002; **50**(6): 1268-74; discussion 74-6.

167. Okun MS, Fernandez HH, Wu SS, Kirsch-Darrow L, Bowers D, Bova F, et al. Cognition and mood in Parkinson's disease in subthalamic nucleus versus globus pallidus interna deep brain stimulation: the COMPARE trial. *Ann Neurol* 2009; **65**(5): 586-95.

168. Okun MS, Foote KD. Parkinson's disease DBS: what, when, who and why? The time has come to tailor DBS targets. *Expert Rev Neurother* 2010; **10**(12): 1847-57.

169. Okun MS, Tagliati M, Pourfar M, Fernandez HH, Rodriguez RL, Alterman RL, et al. Management of referred deep brain stimulation failures: a retrospective analysis from 2 movement disorders centers. *Arch Neurol* 2005; **62**(8): 1250-5.

170. Paek SH, Yun JY, Song SW, Kim IK, Hwang JH, Kim JW, et al. The clinical impact of precise electrode positioning in STN DBS on three-year outcomes. *J Neurol Sci* 2013; **327**(1-2): 25-31.

171. Pakin SK, Cavalcanti C, La Rocca R, Schweitzer ME, Regatte RR. Ultra-high-field MRI of knee joint at 7.0T: preliminary experience. *Acad Radiol* 2006; **13**(9): 1135-42.

172. Pan JW, Avdievich N, Hetherington HP. J-refocused coherence transfer spectroscopic imaging at 7 T in human brain. *Magn Reson Med* 2010; **64**(5): 1237-46.

173. Parent A, Hazrati L-N. Anatomical aspects of information processing in primate basal ganglia. *Trends Neurosci* 1993; **16**(3): 111-6.

174. Parent A, Hazrati LN. Functional anatomy of the basal ganglia. I. The cortico-basal ganglia-thalamo-cortical loop. *Brain research Brain research reviews* 1995; **20**(1): 91-127.

175. Parent A, Hazrati LN. Functional anatomy of the basal ganglia. II. The place of subthalamic nucleus and external pallidum in basal ganglia circuitry. *Brain Research Reviews* 1995; **20**(1): 128-54.

176. Parkinson J. An Essay on the Shaking Palsy. *The Journal of neuropsychiatry and clinical neurosciences* 2002; **14**(2): 223-36.

177. Parnetti L, Castrioto A, Chiasserini D, Persichetti E, Tambasco N, El-Agnaf O, et al. Cerebrospinal fluid biomarkers in Parkinson disease. *Nature reviews Neurology* 2013; **9**(3): 131-40.

178. Peran P, Cherubini A, Assogna F, Piras F, Quattrocchi C, Peppe A, et al. Magnetic resonance imaging markers of Parkinson's disease nigrostriatal signature. *Brain* 2010; **133**(11): 3423-33.

179. Plantinga BR, Temel Y, Roebroeck A, Uludag K, Ivanov D, Kuijf ML, et al. Ultra-high field magnetic resonance imaging of the basal ganglia and related structures. *Front Hum Neurosci* 2014; **8**: 876.

180. Polders DL, Leemans A, Hendrikse J, Donahue MJ, Luijten PR, Hoogduin JM. Signal to noise ratio and uncertainty in diffusion tensor imaging at 1.5, 3.0, and 7.0 Tesla. *J Magn Reson Imaging* 2011; **33**(6): 1456-63.

181. Pollo C, Kaelin-Lang A, Oertel MF, Stieglitz L, Taub E, Fuhr P, et al. Directional deep brain stimulation: an intraoperative double-blind pilot study. *Brain* 2014; **137**(Pt 7): 2015-26.

182. Postuma RB, Berg D, Stern M, Poewe W, Olanow CW, Oertel W, et al. MDS clinical diagnostic criteria for Parkinson's disease. *Movement disorders: official journal of the Movement Disorder Society* 2015; **30**(12): 1591-601.

183. Pouratian N, Zheng Z, Bari AA, Behnke E, Elias WJ, Desalles AA. Multi-institutional evaluation of deep brain stimulation targeting using probabilistic connectivity-based thalamic segmentation. *Journal of neurosurgery* 2011; **115**(5): 995-1004.

184. Quester R, Schroder R. The shrinkage of the human brain stem during formalin fixation and embedding in paraffin. *J Neurosci Methods* 1997; **75**(1): 81-9.

185. Ren J, Lakoski S, Haller RG, Sherry AD, Malloy CR. Dynamic monitoring of carnitine and acetylcarnitine in the trimethylamine signal after exercise in human skeletal muscle by 7T 1H-MRS. *Magn Reson Med* 2013; **69**(1): 7-17.

186. Richter EO, Hoque T, Halliday W, Lozano AM, Saint-Cyr JA. Determining the position and size of the subthalamic nucleus based on magnetic resonance imaging results in patients with advanced Parkinson disease. *Journal of Neurosurgery* 2004; **100**(3): 541-6.

187. Rijkers K, Temel Y, Visser-Vandewalle V, Vanormelingen L, Vandersteen M, Adriaensens P, et al. The microanatomical environment of the subthalamic nucleus. Technical note. *Journal of neurosurgery* 2007; **107**(1): 198-201.

188. Robitaille PM, Warner R, Jagadeesh J, Abduljalil AM, Kangarlu A, Burgess RE, et al. Design and assembly of an 8 tesla whole-body MR scanner. *J Comput Assist Tomogr* 1999; **23**(6): 808-20.

189. Rodriguez-Oroz MC, Rodriguez M, Guridi J, Mewes K, Chockkman V, Vitek J, et al. The subthalamic nucleus in Parkinson's disease: somatotopic organization and physiological characteristics. *Brain* 2001; **124**(Pt 9): 1777-90.

190. Rooney WD, Johnson G, Li X, Cohen ER, Kim SG, Ugurbil K, et al. Magnetic field and tissue dependencies of human brain longitudinal 1H2O relaxation in vivo. *Magn Reson Med* 2007; **57**(2): 308-18.

191. Sato F, Parent M, Levesque M, Parent A. Axonal branching pattern of neurons of the subthalamic nucleus in primates. *The Journal of comparative neurology* 2000; **424**(1): 142-52.

192. Sato H, Kawagishi K. Labyrinthine artery detection in patients with idiopathic sudden sensorineural hearing loss by 7-T MRI. *Otolaryngology--head and neck surgery: official journal of American Academy of Otolaryngology-Head and Neck Surgery* 2014; **150**(3): 455-9.

193. Schafer A, Forstmann BU, Neumann J, Wharton S, Mietke A, Bowtell R, et al. Direct visualization of the subthalamic nucleus and its iron distribution using high-resolution susceptibility mapping. *Human brain mapping* 2012; **33**(12): 2831-42.

194. Schaltenbrand G, Wahren W. Atlas for stereotaxy of the human brain: with an accompanying guide. Stuttgart: Thieme; 2005.

195. Schaltenbrand G, Wahren W, Hassler R. Atlas for Stereotaxy of the Human Brain. 2nd ed. Stuttgart, Germany: Thieme; 1977.

196. Schuepbach WM, Rau J, Knudsen K, Volkmann J, Krack P, Timmermann L, et al. Neurostimulation for Parkinson's disease with early motor complications. *N Engl J Med* 2013; **368**(7): 610-22.

197. Schulz G, Crooijmans HJA, Germann M, Scheffler K, Müller-Gerbl M, Müller B. Three-dimensional strain fields in human brain resulting from formalin fixation. *Journal of Neuroscience Methods* 2011; **202**(1): 17-27.

198. Smith Y, Villalba R. Striatal and extrastriatal dopamine in the basal ganglia: an overview of its anatomical organization in normal and Parkinsonian brains. *Movement disorders: official journal of the Movement Disorder Society* 2008; **23 Suppl 3**: S534-47.

199. Soria G, De Notaris M, Tudela R, Blasco G, Puig J, Planas AM, et al. Improved assessment of ex vivo brainstem neuroanatomy with high-resolution MRI and DTI at 7 Tesla. *Anat Rec (Hoboken)* 2011; **294**(6): 1035-44.

200. Stuber C, Morawski M, Schafer A, Labadie C, Wahnert M, Leuze C, et al. Myelin and iron concentration in the human brain: a quantitative study of MRI contrast. *Neuroimage* 2014; **93 Pt 1**: 95-106.

201. Sulzer J, Haller S, Scharnowski F, Weiskopf N, Birbaumer N, Blefari ML, et al. Real-time fMRI neurofeedback: progress and challenges. *Neuroimage* 2013; **76**: 386-99.

202. Teeuwisse WM, Brink WM, Webb AG. Quantitative assessment of the effects of high-permittivity pads in 7 Tesla MRI of the brain. *Magn Reson Med* 2012; **67**(5): 1285-93.

203. Temel Y, Ackermans L, Celik H, Spincemaille GH, van der Linden C, Walenkamp GH, et al. Management of hardware infections following deep brain stimulation. *Acta Neurochir (Wien)* 2004; **146**(4): 355-61; discussion 61.

204. Temel Y, Blokland A, Steinbusch HWM, Visser-Vandewalle V. The functional role of the subthalamic nucleus in cognitive and limbic circuits. *Prog Neurobiol* 2005; **76**(6): 393-413.

205. Temel Y, Kessels A, Tan S, Topdag A, Boon P, Visser-Vandewalle V. Behavioural changes after bilateral subthalamic stimulation in advanced Parkinson disease: a systematic review. *Parkinsonism Relat Disord* 2006; **12**(5): 265-72.

206. Theysohn JM, Maderwald S, Kraff O, Moenninghoff C, Ladd ME, Ladd SC. Subjective acceptance of 7 Tesla MRI for human imaging. *MAGMA* 2008; **21**(1-2): 63-72.

207. Tonge M, Ackermans L, Kocabicak E, van Kranen-Mastenbroek V, Kuijf M, Oosterloo M, et al. A detailed analysis of intracerebral hemorrhages in DBS surgeries. *Clinical neurology and neurosurgery* 2015; **139**: 183-7.

208. Tournier J-D, Calamante F, Connelly A. MRtrix: Diffusion tractography in crossing fiber regions. *Int J Imaging Syst Technol* 2012; **22**(1): 53-66.

209. Tournier JD, Calamante F, Connelly A. Robust determination of the fibre orientation distribution in diffusion MRI: non-negativity constrained super-resolved spherical deconvolution. *Neuroimage* 2007; **35**(4): 1459-72.

210. Tournier JD, Calamante F, Gadian DG, Connelly A. Direct estimation of the fiber orientation density function from diffusion-weighted MRI data using spherical deconvolution. *Neuroimage* 2004; **23**(3): 1176-85.

211. Tournier JD, Mori S, Leemans A. Diffusion tensor imaging and beyond. *Magn Reson Med* 2011; **65**(6): 1532-56.

212. Tovi M, Ericsson A. Measurements of T1 and T2 over time in formalin-fixed human whole-brain specimens. *Acta Radiologica* 1992; **33**(5): 400-4.

213. Unrath A, Klose U, Grodd W, Ludolph AC, Kassubek J. Directional colour encoding of the human thalamus by diffusion tensor imaging. *Neuroscience letters* 2008; **434**(3): 322-7.

214. Vaillancourt DE, Spraker MB, Prodoehl J, Abraham I, Corcos DM, Zhou XJ, et al. High-resolution diffusion tensor imaging in the substantia nigra of de novo Parkinson disease. *Neurology* 2009; **72**(16): 1378-84.

215. Vaughan JT, Garwood M, Collins CM, Liu W, DelaBarre L, Adriany G, et al. 7T vs. 4T: RF power, homogeneity, and signal-to-noise comparison in head images. *Magn Reson Med* 2001; **46**(1): 24-30.

216. Vedrine P, Aubert G, Belorgey J, Berriaud C, Bourquard A, Bredy P, et al. Manufacturing of the Iseult/INUMAC Whole Body 11.7 T MRI Magnet. *Applied Superconductivity, IEEE Transactions on* 2014; **24**(3): 1-6.

217. Villalba RM, Lee H, Smith Y. Dopaminergic denervation and spine loss in the striatum of MPTP-treated monkeys. *Experimental Neurology* 2009; **215**(2): 220-7.

218. Voelker MN, Kraff O, Brenner D, Wollrab A, Weinberger O, Berger MC, et al. The traveling heads: multicenter brain imaging at 7 Tesla. *Magnetic Resonance Materials in Physics, Biology and Medicine* 2016; **29**(3): 399-415.

219. Welter ML, Schupbach M, Czernecki V, Karachi C, Fernandez-Vidal S, Golmard JL, et al. Optimal target localization for subthalamic stimulation in patients with Parkinson disease. *Neurology* 2014; **82**(15): 1352-61.

220. Wharton S, Bowtell R. Whole-brain susceptibility mapping at high field: a comparison of multiple- and single-orientation methods. *Neuroimage* 2010; **53**(2): 515-25.

221. Wichmann T, Bergman H, DeLong MR. The primate subthalamic nucleus. I. Functional properties in intact animals. *J Neurophysiol* 1994; **72**(2): 494-506.

222. Wichmann T, Dostrovsky JO. Pathological basal ganglia activity in movement disorders. *Neuroscience* 2011; **198**: 232-44.

223. Wiegell MR, Tuch DS, Larsson HB, Wedeen VJ. Automatic segmentation of thalamic nuclei from diffusion tensor magnetic resonance imaging. *Neuroimage* 2003; **19**(2 Pt 1): 391-401.

224. Wiggins GC, Triantafyllou C, Potthast A, Reykowski A, Nittka M, Wald LL. 32-channel 3 Tesla receive-only phased-array head coil with soccer-ball element geometry. *Magn Reson Med* 2006; **56**(1): 216-23.

225. Wodarg F, Herzog J, Reese R, Falk D, Pinsker MO, Steigerwald F, et al. Stimulation site within the MRI-defined STN predicts postoperative motor outcome. *Movement disorders: official journal of the Movement Disorder Society* 2012; **27**(7): 874-9.

226. Wright PJ, Mougin OE, Totman JJ, Peters AM, Brookes MJ, Coxon R, et al. Water proton T1 measurements in brain tissue at 7, 3, and 1.5 T using IR-EPI, IR-TSE, and MPRAGE: results and optimization. *MAGMA* 2008; **21**(1-2): 121-30.

227. Wyss M, Bruegger M, Daeubler B, Vionnet L, Brunner D, Pruessmann K. Visualization of human brainstem substructures using gray matter nulling 3D-MPRAGE at 7Tesla. Joint Annual Meeting ISMRM-ESMRMB; 2014; Milan, Italy; 2014.

228. Yacoub E, Harel N, Ugurbil K. High-field fMRI unveils orientation columns in humans. *Proceedings of the National Academy of Sciences of the United States of America* 2008; **105**(30): 10607-12.

229. Yao B, Li TQ, Gelderen P, Shmueli K, de Zwart JA, Duyn JH. Susceptibility contrast in high field MRI of human brain as a function of tissue iron content. *Neuroimage* 2009; **44**(4): 1259-66.

230. Yokoyama T, Ando N, Sugiyama K, Akamine S, Namba H. Relationship of stimulation site location within the subthalamic nucleus region to clinical effects on parkinsonian symptoms. *Stereotact Funct Neurosurg* 2006; **84**(4): 170-5.

231. Yoshida S, Nambu A, Jinnai K. The distribution of the globus pallidus neurons with input from various cortical areas in the monkeys. *Brain Res* 1993; **611**(1): 170-4.

232. Yovel Y, Assaf Y. Virtual definition of neuronal tissue by cluster analysis of multi-parametric imaging (virtual-dot-com imaging). *Neuroimage* 2007; **35**(1): 58-69.

233. Yushkevich PA, Piven J, Hazlett HC, Smith RG, Ho S, Gee JC, et al. User-guided 3D active contour segmentation of anatomical structures: significantly improved efficiency and reliability. *Neuroimage* 2006; **31**(3): 1116-28.

234. Zaidel A, Spivak A, Grieb B, Bergman H, Israel Z. Subthalamic span of beta oscillations predicts deep brain stimulation efficacy for patients with Parkinson's disease. *Brain* 2010; **133**(Pt 7): 2007-21.

235. Zhang Y, Brady M, Smith S. Segmentation of brain MR images through a hidden Markov random field model and the expectation-maximization algorithm. *IEEE Trans Med Imaging* 2001; **20**(1): 45-57.

APPENDIX A

MEDICAL ETHICS COMMITTEE DOCUMENTATION

Research protocol as approved by the Medical Ethics Committee at Maastricht University Medical Center.
Appendix to Chapters 5 and 6.

A.1 Overview

Protocol title: Ultra-high field imaging of the cortico-striato-subthalamic functional and structural connectivity to improve deep brain stimulation surgery in Parkinson's disease patients

Protocol ID: STN connectivity

ABR number: NL42613.068.13

Short title: STN connectivity in PD with MRI

Version: 5

Date: 07-08-2013

Project leader: Prof. Dr. Yasin Temel
Y.Temel@MaastrichtUniversity.nl

Project team: Prof. Dr. Yasin Temel
Y.Temel@MaastrichtUniversity.nl
Prof. Dr. Ir. Bart ter Haar Romeny
B.M.terHaarRomeny@tue.nl
Ir. Birgit Plantinga
B.R.Plantinga@tue.nl

Contact person: Ir. Birgit Plantinga
B.R.Plantinga@tue.nl

Sponsor: Academic Hospital Maastricht

Subsiding party: Netherlands Organisation for Scientific Research (NWO)

Independent expert: O.E.M.G. Schijns, M.D., PhD

A.2 Contents

A.3   Summary

A.3.1   Rationale

The subthalamic nucleus (STN) is anatomically a small region in the diencephalic-mesencephalic junction and functionally plays an important role in the pathophysiology of Parkinson's disease (PD). The neuronal activity of the STN is shifting from single-spike activity in the normal condition to burst firing mode in PD. This burst activity is held responsible for some of the cardinal symptoms in PD such as akinesia, rigidity and tremor. Deep brain stimulation (DBS), a treatment involving the stereotactic implantation of electrodes in deeply situated regions, of the STN is an effective treatment in PD and is thought to counteract with the pathological burst activity. Short- and long-term results show that DBS of the STN substantially improves the quality of life of PD patients. However, there are two major drawbacks. The first is the induction of psychiatric side-effects such as impulsivity, depression and (hypo)mania, which can be a major burden for the patient and family. We argue that this is due to the stimulation of the non-motor territories of the STN. (Temel et al., 2005, Temel et al., 2007). It is not possible with the conventional imaging techniques at standard clinical magnetic field strengths (1.5 and 3 Tesla) to identify the motor and non-motor territories of the STN. If this would be possible, then we could implant the electrode selectively in the motor part and potentially prevent the occurrence of psychiatric side-effects. The second drawback is the duration of the surgery. The duration can vary from 6 to 8 hours, usually being exhaustive for the patient. This is related to the fact that we cannot detect the STN precisely on the conventional images and therefore need to test the patient extensively intraoperatively to find the right spot. Therefore, we propose a set of experiments to test the hypothesis that with ultra-high field structural, functional and diffusion MRI we will be able to identify the STN and its functional subterritories in PD patients and age- and sex-matched control subjects.

A.3.2 Objective

The primary objective is to assess the structural and functional segregation of the STN into its motor and non-motor regions in PD patients and healthy controls.

A.3.3 Study design

For this study ten pre-operative PD patients scheduled for DBS surgery and ten healthy controls will be scanned on a 7 T MRI scanner. The functional and structural connectivities of the STNs in these subjects will be investigated and compared.

A.3.4 Study population

Ten patients scheduled for STN DBS surgery and ten healthy gender and age matched controls will be recruited.

A.3.5 Main study parameters

The main study parameter will be the structural and functional partition of the STN into its motor and non-motor regions in PD patients and healthy controls.

A.3.6 Nature and extent of the burden and risks associated with participation, benefit and group relatedness

The burden for the patients rests with drug withdrawal extended for 90 minutes more than required for the standard medical procedures, which are performed regardless of the patient's participation in this study. When attention is paid to the contra-indications for MRI, 7 T MRI is harmless.

A.4   Introduction and rationale

Parkinson disease (PD) is a common neurodegenerative disorder, characterized by motor symptoms such as tremor, rigidity and bradykinesia, and also non-motor symptoms such as depression and cognitive dysfunction. Patients are initially treated successfully with drugs (e.g. levodopa). However, prolonged drug use is limited due to dyskinesias, motor fluctuations and debilitating side-effects, like hallucinations.

In these advanced stages of PD, neurosurgical treatment is the next therapeutic option. In 1993 deep brain stimulation (DBS) (a treatment involving the stereotactic implantation of electrodes in deeply situated regions) of the subthalamic nucleus (STN) was introduced. The STN is anatomically a small region in the diencephalic-mesencephalic junction and functionally plays an important role in the pathophysiology of Parkinson's disease. The neuronal activity of the STN is shifting from single-spike activity in the normal condition to burst firing mode in PD. This burst activity is held responsible for some of the cardinal symptoms in PD. DBS of the STN is an effective treatment in PD and is thought to counteract with the pathological burst activity.

Multiple long-term follow-up studies have demonstrated long lasting beneficial effects on the motor function of PD patients due to STN DBS. However, there are two major drawbacks.

The first is the induction of psychiatric side-effects such as impulsivity, depression and (hypo)mania, which can be a major burden for the patient and family. Previous studies revealed a total of 41% of all operated patients to present with these problems (Temel et al., 2006). We think that these induced side-effects are due to the stimulation of the non-motor territories of the STN (Temel et al., 2005, Temel et al., 2007a). It is not possible with the conventional imaging techniques to identify these motor and non-motor territories. If this would be possible, then we could implant the electrode selectively in the motor part and potentially prevent the occurrence of psychiatric side-effects.

The second drawback is the duration of the surgery, which can vary from 6 to 8 hours, usually being exhaustive for the patient. This is also related to the fact that we cannot detect the STN precisely on the conventional images and

therefore need to test the patient extensively intraoperatively to find the right spot.

So in order to decrease side-effects and shorten the duration of the surgery, accurate imaging of the STN and its subregions is required. Although the STN cannot be clearly identified with the conventional imaging techniques, it is expected that at 7 T, the contrast and anatomic delineation of the STN improve greatly. Furthermore, with the use of functional and diffusion MRI sequences, connections between cortical regions and deep brain structures can be investigated. Inspection of the connections between the motor and limbic cortical areas and the STN is expected to reveal information on the segregation of the STN in its motor and non-motor parts, which can serve to improve targeting during DBS.

Therefore, we propose a set of experiments to test the hypothesis that with ultra high field structural, functional and diffusion MRI we will be able to identify the STN and its functional subterritories in PD patients and age- and sex-matched control subjects.

A.5   Objectives

A.5.1   *Primary objective*

The primary objective is to assess the structural and functional segregation of the STN into its motor and non-motor regions in PD patients and healthy controls.

A.5.2   *Secondary objectives*

The secondary objectives are:

1.   To compare the strength of the functional and structural connectivity between the STN and the motor and non-motor cortical areas between PD patients and controls. Due to the high bursting activity in the STN of PD patients, this connectivity is expected to be stronger in this population.

2.   To compare the brain areas structurally and functionally connected to the STN with the brain areas structurally and functionally connected to the stimulation electrode implanted in PD patients. This will provide insight into the brain areas that are target for stimulation compared to the brain areas that are actually stimulated.

3.   To investigate the brain activation pattern during the task-based fMRI and assess the differences between PD patients and healthy controls.

A.6   Study design

The study will be an observational study that investigates and compares the structural and functional connectivity of the subthalamic nucleus in 10 PD patients and 10 healthy controls. The experiment consists of a one hour 7 T MRI scan that each subject will undergo and the rating of affective pictures.

A.7   Study population

A.7.1   Population (base)

The subjects consist of ten PD patients and ten controls. These subjects are drawn from two populations:

1.   PD patients scheduled for DBS surgery

These patients will be recruited from the academic hospital Maastricht (azM) and University Hospital Aachen (UHA) (German name: Universitätsklinikum Aachen, UKA). An average of 25 PD patients is submitted to STN DBS surgery in the azM per year and another 25 PD patients is submitted to STN DBS surgery at UHA. Assuming that half of the eligible patients consent to participate in the research, the likelihood for the planned number of 10 patients to be recruited is estimated to be achievable. Patients with tremor dominant PD will be excluded from participation of the study due to potential movement artifacts during scanning. The UHA will only be involved with recruitment of patients. The research itself will be performed in Maastricht.

Over the period November 1999 to June 2005, the age of the PD patients scheduled for DBS surgery was 61.9 +- 10.0 (Temel et al., 2007b). This is expected to be a good indication of the age of patients included in the proposed study.

2.   Age and gender matched controls

These healthy controls will be drawn from the same age and gender population as the PD patients. Since these subjects are volunteers not suffering from neurological diseases, the source population is large, and recruiting 10 healthy subjects is expected to be no problem.

A.7.1.1   Inclusion criteria

For both groups:
1.   Subjects must be mentally competent (wilsbekwaam)

For the PD patients only:
1.   PD patients scheduled for DBS surgery

For the healthy controls only:

1. The age and gender of the group of healthy controls should not differ significantly from the age of the group of patients.

A.7.1.2 Exclusion criteria

For both groups:

1. Head injury
2. Stroke
3. Other neurological diseases other than PD
4. Metallic prostheses or pacemaker in the subject's body or other contra indications for MRI. Prior to scanning, subjects will fill out a screening form (see attachment A.16.1). This form will be sent along with the information letter to inform subjects about the full list of contra-indications. The form will only be filled in on the day of the scan.

For the PD patients only:

1. Inability to abstain from dopaminergic drug use
2. Any neurological or psychiatric disease other than PD

For the controls only:

1. Any neurological or psychiatric disease
2. Use of medication affecting the central nervous system

A.7.2   Sample size calculation

To determine the minimal group sizes for this study, data from a study by Baudrexel et al. (Baudrexel et al., 2011) was used. They compared the functional connectivity of the STN acquired with a 3T MRI scanner between 31 PD patients (N_{p1} = 31) and 44 healthy controls (N_{h1} = 44). They found a significantly increased connectivity of the STN to the supplementary motor cortex with t_1 = 3.3. Based on these findings, we computed the minimal sample sizes of our two groups expecting to result in a significance level of at least 0.05 which corresponds to a t-value of t_1 = 1.6659. Knowing the t-value and population sizes of the study by Baudrexel et al., the minimal population size corresponding to t_2 = 1.6659 can be computed as follows.

In general, the t-value can be computed with:

$$t = \frac{\overline{X_1} - \overline{X_2}}{\sigma_{X1X2}\sqrt{\frac{1}{N_1} + \frac{1}{N_2}}}$$

where $\overline{X_1}$ and $\overline{X_2}$ are the sample mean estimates, σ_{X1X2} is an estimator of the common standard deviation of the two samples and N_1 and N_2 are the two sample sizes.

This can be simplified to:

$$t = \frac{q}{\sqrt{\frac{1}{N_1} + \frac{1}{N_2}}}$$

with:

$$q = \frac{\overline{X_1} - \overline{X_2}}{\sigma_{X1X2}}$$

Assuming that the two groups described in the literature and used in the current study will have the same means and standard deviations, the value of q is equal as well, leading to the following equality:

$$t_1\sqrt{\frac{1}{N_{p1}} + \frac{1}{N_{h1}}} = t_2\sqrt{\frac{1}{N_{p2}} + \frac{1}{N_{h2}}}$$

If we also strive for equal sample sizes in our study ($N_{p2} = N_{h2}$), substituting $t_1 = 3.3$, $N_{p1} = 31$, $N_{h1} = 44$ and $t_2 = 1.6659$ leads to:

$$N_{p2} = N_{h2} = 9.3$$

So if we want to reach a significant difference in functional connectivity with $p < 0.05$ our two groups should have at least ten subjects each.

For the structural connectivity, the difference between the groups is expected to be similar to the functional connectivity. Therefore there is no reason to assume different minimal group sizes for the structural connectivity analysis.

A.8   Treatment of subjects

Subjects will undergo six consecutive 7 T MRI scans with a consecutive scan time of one hour. During this scan, subjects will be kindly asked to move as little as possible. During one of the scans, subjects will view affective pictures, which they will rate after the scanning session. If fatigue is playing up, then we will give the subjects a period of break between one or more of the six scans.

Prior to surgery, patients will always be scored on the Unified Parkinson's Disease Rating Scale (UPDRS), for which they need to be off medication. This test is performed as part of the standard clinical procedure and therefore applies to all patients, independent of their participation in this study. However, because patients need to be off medication for the MRI scan as well, this scan will be performed right before or after their regular clinical UPDRS screening.

A.9   Methods

A.9.1   *Main study parameters/end points*

The main study endpoint will be the structural and functional partition of the STN into its motor and non-motor regions in PD patients and healthy controls.

A.9.2   *Secondary study parameters/endpoints*

The secondary study parameters are:

1. The strength and directionality of the functional and structural connectivity between the STN and the motor and non-motor cortical areas in PD patients and controls.

2. Brain areas that show a significantly stronger or weaker functional or structural connectivity from the STN to the motor or limbic cortical areas or vice versa in PD patients than in controls.

3. The brain areas structurally and functionally connected to the stimulation zone of the optimal electrode (only in patients).

4. Brain areas that show an activation related to the fMRI task.

5. Brain areas that show significantly more or significantly less activation during the task fMRI in PD patients than in healthy subjects.

A.9.2.1   Other study parameters

Other study parameters are:

1. Age

2. Gender

3. UPDRS score (patients only)

A.9.3   *Study procedures*

Ten pre-operative PD patients scheduled for DBS surgery and ten age and gender matched controls will be scanned on a 7 T MRI scanner located at Brains Unlimited Maastricht. Scanning at 7 T is expected to greatly enhance

structural and functional connectivity analysis compared to scanning at 1.5T or 3T due to improvements in contrast to noise ratio (CNR) and signal to noise ratio (SNR).

A.9.3.1 Preparation (only for patients)

Part of the standard clinical procedure for DBS surgery for PD is a UPDRS screening of the patients for which they need to be off-medication for 8 hours. All patients must undergo this screening, regardless of their participation in this study. To ease the burden on the patients, these screenings are performed in the morning. Because dopaminergic drugs greatly influence the fMRI scans (Haslinger et al., 2001, Mattay et al., 2002), in this study patients will be scanned during drug-off state as well. To ease the burden on the patients, the scan is performed right before or after their regular UPDRS screening. Because the disease stage is expected to influence the measurements, the clinically acquired UPDRS will be used for data analysis as well.

A.9.3.2 Data acquisition

The following scans will be performed:

1. One T2*-weighted and susceptibility weighted image (SWI) to visualize veins and the STN. This will provide information on more accurate structural delineation of the STN (Abosch2010).

2. One T1-weighted magnetization-prepared rapid acquisition with gradient echo (MP-RAGE) image with excellent white/grey matter contrast, which can be used for registration of the images due to its relatively minimal distortions.

3. Two diffusion weighted images (DWI) acquired with different protocols to investigate the structural connectivity of the STN to the limbic and motor cortical areas. The first protocol will be a high resolution (1.5mm isotropic or better), b-value=1000s/mm2, 60 directions acquisition for diffusion tensor imaging (DTI) modelling. The second protocol will aim at higher b-value acquisition with more directions (HARDI: High Angular Resolution Diffusion Imaging (Peeters et al., 2009, Prckovska et al., 2009)) at slightly lower resolution to better support 'crossing-fibre' modelling that goes beyond DTI, such

as constrained spherical deconvolution (Tournier2007) and enhanced with contextual (Prckovska et al., 2010) and tensorial methods (Florack et al., 2010).

4. Two blood oxygenation level-dependent (BOLD) contrast sensitive functional MRI (fMRI) scans with a gradient-echo echo-planar-imaging (GE-EPI) acquisition. At 7T, it is possible to acquire at high resolution of 1.2mm isotropic or better for the whole brain. These scans will provide information on the functional connectivity between the STN and the limbic and motor cortical areas and on the time delay between different targets. They consist of:

    a. One resting state (rs) fMRI scan.

    b. One visual task related fMRI scan. During this task subjects will view series of pictures selected from the International Affective Pictures System (IAPS) (Lang et al., 2008). These pictures will vary in valence and arousal. This task is expected to reveal the part of the STN and other brain regions that are involved in limbic processes. After the scanning session is over, subjects will be asked to rate these pictures on valence and arousal.

5. One time of flight (TOF) scan will be performed, for visualization of the arteries. Together with the venogram from the T2*/SWI scan, this will also provide unprecedented delineation of brain vessels that need to be avoided during surgery, an important secondary benefit.

An overview of the performed scans is shown in Table A.1.

Table A.1: Scan protocol.

Scan type	Scan sequence	Scan time (min)
Anatomical	SWI	5
Anatomical	MP-RAGE	6
Diffusion	DWI	2 x 10
Functional	rs fMRI	10
Functional	task fMRI	10
Anatomical	TOF	7
Total		58

The following scan will be performed on patients only as part of the standard clinical procedure. After DBS surgery, the patients will be scanned again on a 1.5 T MRI scanner, to visualise the location of the electrodes. This

scan is the standard procedure for DBS surgeries and will therefore be performed not in context of this study. However, combining these scans with the required 7 T scans will provide interesting information on the position of the optimal stimulation electrode.

A.9.3.3   Data analysis

Both functional and structural connectivity analysis will be performed on these data. The functional connectivity will be assessed with a general linear model, which correlates the average BOLD signal in the region of interest (ROI) to the BOLD signal of the remaining voxels of the brain, while also taking into account possible confounds. To assess the structural connectivity, tractography initiated in the ROI will be performed, which computes estimates of the trajectories of white matter axonal bundles. The structural connectivity measures will be derived from the relative number of streamlines passing through the remaining voxels of the brain and from the fractional anisotropy (FA) along the tracts.

The ROIs include the STN, the motor and limbic cortical areas and in patients also the area that is stimulated by the optimal electrode (stimulation zone) (see Figure A.1). The motor and limbic cortical areas will be used as ROIs to find their connectivity distribution on the STN. The part of the STN that shows the largest connectivity to the motor cortical area is thought to correspond to the somatomotor part of the STN, which needs to be stimulated. The part that shows the largest connectivity to the limbic cortical area is thought to correspond to the limbic part of the STN and should be avoided. Furthermore, the STN will be used as ROI to find all structural and functional connections of the STN. Finally, because the stimulation zone is expected to not exactly coincide with the STN, using this zone as ROI as well, will provide information on the brain structures that are connected to the area that is actually stimulated.

In the end, this will result in three structural and functional connectivity analyses for the healthy subjects and four for the PD patients. Comparison of these connectivity patterns between PD patients and healthy controls will help gain insight into the underlying mechanism of PD.
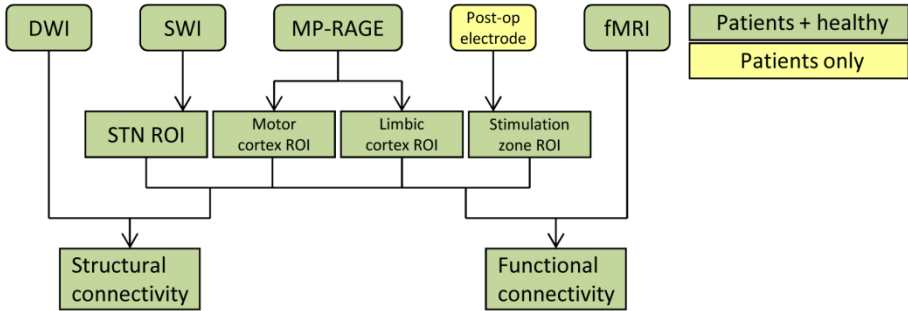
Figure A.1: Overview data analysis

Apart from these connectivity analyses, the task related fMRI data will be investigated as well. The brain areas that show activity correlated to the valence or arousal of the shown pictures are thought to be involved in limbic processing, which is especially interesting when it concerns the partition of the STN.

A.9.4   *Withdrawal of individual subjects*

Subjects can leave the study at any time for any reason if they wish to do so without any consequences. The investigator can decide to withdraw a subject from the study for urgent medical reasons.

A.9.5   *Replacement of individual subjects after withdrawal*

If subjects are withdrawn before the MRI scan has been performed, new subjects will be included. For financial reasons, new subjects cannot be included if the MRI scan has already been performed.

A.10   Safety reporting

A.10.1   Section 10 WMO event

In accordance to section 10, subsection 1, of the WMO, the investigator will inform the subjects and the reviewing accredited METC if anything occurs, on the basis of which it appears that the disadvantages of participation may be significantly greater than was foreseen in the research proposal. The study will be suspended pending further review by the accredited METC, except insofar as suspension would jeopardise the subjects' health. The investigator will take care that all subjects are kept informed.

A.10.2   AEs and SAEs

A.10.2.1   Adverse events (AEs)

Adverse events are defined as any undesirable experience occurring to a subject during the study, whether or not considered related to the experimental intervention. All adverse events reported spontaneously by the subject or observed by the investigator or his staff will be recorded.

A.10.2.2   Serious adverse events (SAEs)

A serious adverse event is any untoward medical occurrence or effect that at any dose:

- results in death;
- is life threatening (at the time of the event);
- requires hospitalisation or prolongation of existing inpatients' hospitalisation;
- results in persistent or significant disability or incapacity;
- is a congenital anomaly or birth defect;
- Any other important medical event that may not result in death, be life threatening, or require hospitalization, may be considered a serious adverse experience when, based upon appropriate medical judgement, the event may jeopardize the subject or may require an intervention to prevent one of the outcomes listed above.

Serious adverse events reported spontaneously by the subject or observed by the investigator or his staff will be recorded.

The sponsor will report the SAEs through the web portal *ToetsingOnline* to the accredited METC that approved the protocol, within 15 days after the sponsor has first knowledge of the serious adverse reactions.

SAEs that result in death or are life threatening should be reported expedited. The expedited reporting will occur not later than 7 days after the responsible investigator has first knowledge of the adverse reaction. This is for a preliminary report with another 8 days for completion of the report.

All patients involved in this study are scheduled for DBS surgery. Hospitalisation due to DBS surgery will therefore not be reported.

A.10.2.3 Follow-up of adverse events

All AEs will be followed until they have abated, or until a stable situation has been reached. Depending on the event, follow up may require additional tests or medical procedures as indicated, and/or referral to the general physician or a medical specialist. SAEs need to be reported till end of study within the Netherlands, as defined in the protocol.

A.11 Data analysis

A.11.1 Data calculation

The acquired data will be preprocessed with the aid of the FMRIB Software Library (FSL) (Jenkinson et al., 2012). For computation of the structural connectivity, fiber tracking will be performed with the camino (Cook et al., 2006) software package. Functional connectivity analysis will be performed with the Statistical Parameter Mapping (SPM) software package. Two-sampled t-tests will be used to assess the differences in functional and structural connectivity patterns between healthy subjects and controls. Finally, visual representation of the data will be conducted with the program vIST/e developed at Eindhoven University of Technology (TU/e).

A.11.2 Data representation

The parameters will be presented both quantitatively as well as qualitatively.

A.11.2.1 Qualitative representation

The regions of the STN that are functionally and structurally connected to the motor and limbic cortical areas will be represented visually for the two groups. The brain areas involved in other structural or functional connectivities to the STN will be visualized separately as well. Furthermore the tracts of the fibers resulting from the structural connectivity analysis will be visualized. Finally the brain areas that show a significantly stronger or weaker functional or structural connectivity to from the STN to the motor or limbic cortical areas or vice versa in PD patients than in controls will be inspected visually.

A.11.2.2 Quantitative representation

The strength of the structural and functional connections can be measured as described in paragraph A.9.3.3. These connections and their strengths will be summarized in a table. Furthermore areas with a significantly different connectivity between the two groups will be specified in this table as well (along with the statistical values).

A.12 Ethical considerations

A.12.1 Regulation statement

The study will be conducted according to the principles of the Declaration of Helsinki and in accordance with the Medical Research Involving Human Subjects Act (WMO).

A.12.2 Recruitment and consent

The recruitment of patients and healthy controls differs.

A.12.2.1 Patients

When a patient is referred for a DBS procedure and a consultation takes place with a neurosurgeon or neurologist, then the patient will be informed about the research. He will be kindly asked whether he is interested in participating in this study and will be given at least a week to consider.

A.12.2.2 Controls

Controls will be recruited through paper advertisements (see attachment A.16.2). Advertisements will be hanged on general notice boards in Maastricht University (UM), TU/e and the azM and in the waiting room of the neurology and neurosurgery policlinic of the azM. When interested subjects receive the information letter they will be given at least a week to consider.

A.12.2.3 Patients and controls

All subjects will be informed verbally and on paper about the goal of the research, the procedures, the risks, etc. Questions can be addressed to the involved researchers or an independent expert (Dr. O.E.M.G. Schijns). Subjects will be given at least a week to consider their decision. If subjects are willing to participate, both subject and researcher will sign an informed consent form of which a copy is handed out to the subject (enclosed in information letter). Prior to the experiment the subjects will be asked to fill out a form for metal screening (see attachment A.16.1). Subjects have the

right to withdraw themselves from the study without any explanation at all times.

A.12.3   Benefits and risks assessment, group relatedness

A.12.3.1   Ultra-high field MRI

Although 1.5T and 3T MRI scanners are widely used in clinical environments, 7T scanners are emerging more and more in research. Worldwide there are more than 50 7T MRI scanners in use for human research, of which 4 in The Netherlands. A static magnetic field of up to 14 T or more does not harm biological tissue, but the radiofrequency and MR gradient applied can influence the human body via heating (specific absorption rate (SAR)) or peripheral stimulation. Just as with 1.5 T and 3 T MRI scanners the limits of the radiofrequency (RF) and magnetic resonance (MR) gradient are encoded in the 7 T scanner. Therefore certified users will always stay below these limits making 7 T scanning harmless. Furthermore, just as with 1.5 T and 3 T MRI scanners, metallic objects cannot be inserted into the scanner area of the 7 T MRI scanner. Therefore, subjects with metallic prostheses, pacemakers, neurostimulators, metal clips on blood vessels, metal parts in the eye, an intrauterine device, metal braces and other metal objects will be excluded from the study. Prior to scanning all subjects will fill out a form to screen for these metallic objects. Although 7 T MRI is harmless if contra-indications are taken heed of and if operated by certified users, a small amount of people (5%) may experience vertigo or nausea while entering the scanner (Theysohn et al., 2008). However, these symptoms will be minimised by slowing the subject's entry and exit time into the magnetic field (Chakeres et al., 2003). Also a smaller amount of people may experience a metallic taste in their mouth during the scan.

The advantage of scanning at 7 T over 1.5 T and 3 T is increase in the SNR, CNR, resolution and/or a decrease in scanning time. But most importantly, due to the high iron content of the STN, it is expected to be clearly visible at ultra-high field whereas at 3 T it is not. Since a clear delineation of the STN is important for reliable conclusions of this study, the benefit of scanning at 7 T is believed to outweigh the small risk of nausea while entering the bore (not during the actual scan itself).

A.12.3.2   Medication

For both groups of subjects, the main burden comprises an investment of 90 minutes of their time. This is justified given the importance of prevention of cognitive side-effects of deep brain stimulation.

Furthermore, because dopaminergic drugs greatly influence the fMRI scans (Haslinger et al., 2001, Mattay et al., 2002), patients need to be off medication while being scanned. During the standard clinical UPDRS screening performed as a preparation for DBS surgery, patients need to be off-medication for 8 hours as well. In order to ease the burden of being off-medication during this study, patients will be scanned right before or after this regular UPDRS screening and this will be performed in the morning. Because now they only have to be off-medication for 90 minutes more (30 minutes preparation + 60 minutes scan) than they would have to be if they did not participate, the burden of not using medication is expected to be minimised. Furthermore if fatigue starts to play a role during the MRI scan, patients will be given a break between two different scans.

A.12.3.3   Incidental observations

Even though no neurological diseases (other than PD) are known to the subjects included in this study, it might be possible that images contain anatomical brain features that appear out of the normal range. Therefore, each subject must consent with the anatomical images acquired in this study to be investigated by a radiologist if necessary. If medical follow-up is required, the subject will be informed. Subjects who do not consent will be excluded from the study.

A.12.4   Compensation for injury

The sponsor/investigator has a liability insurance which is in accordance with article 7, subsection 6 of the WMO.

The sponsor (also) has an insurance which is in accordance with the legal requirements in the Netherlands (Article 7 WMO and the Measure regarding Compulsory Insurance for Clinical Research in Humans of 23th June 2003). This insurance provides cover for damage to research subjects through injury or death caused by the study.

1. € 450.000,-- (i.e. four hundred and fifty thousand Euro) maximum for each subject who participates in the research;

2. € 3.500.000,-- (i.e. three million five hundred thousand Euro) maximally for all subjects who participate in the research;

3. € 5.000.000,-- (i.e. five million Euro) for the total damage incurred in all research of the same sponsor.

The insurance applies to the damage that becomes apparent during the study or within 4 years after the end of the study.

A.12.5   *Incentives*

Healthy subjects will receive travel expenses.

After participation, subjects will also receive a paper print of their brain.

A.13   Administrative aspects, monitoring and publication

A.13.1   Handling and storage of data and documents

The subjects' privacy will be protected. Non-authorised people and/or employees of the UM and azM, will not have access to the subjects' data. Image data will be anonymized and encoded. Every subject will be assigned a unique serial number, consisting of a unique number referring to the performed study plus a unique number for this subject. Only the researcher and project leader will have access to the key of this encoding. Data will be kept for fifteen years after the end of the study.

A.13.2   Amendments

Amendments are changes made to the research after a favourable opinion by the accredited METC has been given. All amendments will be notified to the METC that gave a favourable opinion.

A.13.3   Annual progress report

The sponsor/investigator will submit a summary of the progress of the trial to the accredited METC once a year. Information will be provided on the date of inclusion of the first subject, numbers of subjects included and numbers of subjects that have completed the trial, serious adverse events/serious adverse reactions, other problems, and amendments.

A.13.4   End of study report

The investigator will notify the accredited METC of the end of the study within a period of 8 weeks. The end of the study is defined as the last subject's visit.

In case the study is ended prematurely, the investigator will notify the accredited METC within 15 days, including the reasons for the premature termination.

Within one year after the end of the study, the investigator/sponsor will submit a final study report with the results of the study, including any publications/abstracts of the study, to the accredited METC and the Competent Authority.

A.13.5   Public disclosure and publication policy

All results of this study, both positive and negative will be published.

A.14   References

Baudrexel S, Witte T, Seifried C, von Wegner F, Beissner F, Klein JC, Steinmetz H, Deichmann R, Roeper J, Hilker R (2011) Resting state fMRI reveals increased subthalamic nucleus-motor cortex connectivity in Parkinson's disease. Neuroimage 55:1728-1738.

Chakeres DW, Kangarlu A, Boudoulas H, Young DC (2003) Effect of static magnetic field exposure of up to 8 Tesla on sequential human vital sign measurements. J Magn Reson Imaging 18:346-352.

Cook PA, Bai Y, Nedjati-Gilani S, Seunarine KK, Hall MG, Parker GJ, Alexander DC (2006) Camino: Open-Source Diffusion-MRI Reconstruction and Processing. In: 14th Scientific Meeting of the International Society for Magnetic Resonance in Medicine, p 2759 Seattle, WA, USA.

Florack L, Balmashnova E, Astola L, Brunenberg E (2010) A New Tensorial Framework for Single-Shell High Angular Resolution Diffusion Imaging. Journal of Mathematical Imaging and Vision 38:171-181.

Haslinger B, Erhard P, Kämpfe N, Boecker H, Rummeny E, Schwaiger M, Conrad B, Ceballos-Baumann AO (2001) Event-related functional magnetic resonance imaging in Parkinson's disease before and after levodopa. Brain 124:558-570.

Jenkinson M, Beckmann CF, Behrens TE, Woolrich MW, Smith SM (2012) FSL. Neuroimage 62:782-790.

Lang PJ, Bradley MM, Cuthbert BN (2008) International affective picture system (IAPS): Affective ratings of pictures and instruction manual. Technical Report A-8. University of Florida, Gainesville, FL.

Mattay VS, Tessitore A, Callicott JH, Bertolino A, Goldberg TE, Chase TN, Hyde TM, Weinberger DR (2002) Dopaminergic modulation of cortical function in patients with Parkinson's disease. Ann Neurol 51:156-164.

Peeters THJM, Prckovska V, Almsick MAv, Vilanova A, Haar Romenij BMt (2009) Fast and sleek glyph rendering for interactive HARDI data exploration. In: IEEE Pacific Visualization Symposium (PacificVIS '09) pp 153-160 Beijing, China.

Prckovska V, Rodrigues PR, Duits R, Haar Romenij BMt, Vilanova A (2010) Extrapolating fiber crossings from DTI data: can we infer similar fiber

crossings as in HARDI? Workshop on Computational Diffusion MRI. In: MICCAI, pp 1-12 Beijing China.

Prckovska V, Roebroeck AF, Pullens WLPM, Vilanova A, Haar Romenij BMt (2009) The effect of the acquisition parameters for high angular resolution diffusion imaging. In: the 17th Scientific meeting & exhibition of the International Society for Magnetic Resonance in Medicine (ISMRM 17), p 3546 Honolulu, Hawai'i, USA.

Temel Y, Blokland A, Steinbusch HWM, Visser-Vandewalle V (2005) The functional role of the subthalamic nucleus in cognitive and limbic circuits. Prog Neurobiol 76:393-413.

Temel Y, Boothman LJ, Blokland A, Magill PJ, Steinbusch HWM, Visser-Vandewalle V, Sharp T (2007a) Inhibition of 5-HT neuron activity and induction of depressive-like behavior by high-frequency stimulation of the subthalamic nucleus. Proc Natl Acad Sci U S A 104:17087-17092.

Temel Y, Kessels A, Tan S, Topdag A, Boon P, Visser-Vandewalle V (2006) Behavioural changes after bilateral subthalamic stimulation in advanced Parkinson disease: a systematic review. Parkinsonism Relat Disord 12:265-272.

Temel Y, Wilbrink P, Duits A, Boon P, Tromp S, Ackermans L, van Kranen-Mastenbroek V, Weber W, Visser-Vandewalle V (2007b) Single electrode and multiple electrode guided electrical stimulation of the subthalamic nucleus in advanced Parkinson's disease. Neurosurgery 61:346-355; discussion 355-347.

Theysohn JM, Maderwald S, Kraff O, Moenninghoff C, Ladd ME, Ladd SC (2008) Subjective acceptance of 7 Tesla MRI for human imaging. MAGMA 21:63-72.

A.15 List of abbreviations

azM	academic hospital Maastricht (academisch ziekenhuis Maastricht)
BOLD	Blood Oxygenation Level-Dependent
CNR	Contrast to Noise Ratio
DBS	Deep Brain Stimulation
DTI	Diffusion Tensor Imaging
DWI	Diffusion Weighted Imaging
FA	Fractional Anisotropy
fMRI	functional MRI
FSL	FMRIB Software Library
GE-EPI	Gradient-Echo Echo-Planar-Imaging
HARDI	High Angular Resolution Diffusion Imaging
IAPS	International Affective Pictures System
METC	Medical research ethics committee (Medisch Ethische Toetsings Commissie)
MHeNS	School for Mental Health and NeuroScience
MP-RAGE	Magnetization-Prepared Rapid Acquisition with Gradient Echo
MR	Magnetic Resonance
MRI	Magnetic Resonance Imaging
NWO	Netherlands Organisation for Scientific Research (Nederlandse organisatie voor Wetenschappelijk Onderzoek)
PD	Parkinson's Disease
RF	Radio Frequency
ROI	Region Of Interest
rs	resting state
(S)AE	(Serious) Adverse Event
SAR	Specific Absorption Rate
SNR	Signal to Noise Ratio
SPM	Statistical Parameter Mapping
STN	Subthalamic nucleus
SWI	Susceptibility Weighted Imaging
T	tesla, unit of magnetic flux density
TOF	Time Of Flight
TU/e	Eindhoven University of Technology
UHA	University Hospital Aachen
UM	Maastricht University (Universiteit Maastricht)

UPDRS   Unified Parkinson's Disease Rating Scale

WMO   Medical Research Involving Human Subjects Act (Wet Medisch-wetenschappelijk Onderzoek met Mensen)

A.16 Attachments

A.16.1 MRI screening form

Brains Unlimited B.V.

TOESTEMMINGSVERKLARING MRI *

Ik heb de volgende vragen begrepen en eerlijk beantwoord:

- Heeft u een pacemaker? ☐ *Ja* ☐ *Nee*

- Bevinden er zich, behalve eventuele tandvullingen
  en kronen, in uw lichaam metalen delen? ☐ *Ja* ☐ *Nee*
- Te beoordelen door de onderzoeker
  Tatoeages, piercings, metalen draadje achter tanden, Mirena spiraaltje met ☐ *Ja* ☐ *Nee*
  bevestiging van de huisarts (aangehecht).
  Ik ben bekend met de risico's → **Handtekening**
- Niet toegestaan!!:
  Prothesen, clips op bloedvaten, metalen deeltjes in het oog, ☐ *Ja* ☐ *Nee*
  spiraaltje(m.u.v. Mirena), metalen beugels, andere metalen voorwerpen.
  Uw participatie in dit onderzoek is NIET toegestaan. ◄

- Bent u aan hoofd of hersenen geopereerd? ☐ *Ja* ☒ *Nee*

- Zijn bij u hartritmestoornissen bekend? ☐ *Ja* ☐ *Nee*

- Heeft u last van epilepsie? ☐ *Ja* ☐ *Nee*

- Heeft u last van claustrofobie? ☐ *Ja* ☐ *Nee*

- Bent u zwanger of denkt u dat te zijn? ☐ *Ja* ☐ *Nee*

- Heeft u diabetes? ☐ *Ja* ☐ *Nee*

- Heeft u last van hart- en vaatziekten? ☐ *Ja* ☐ *Nee*

- Kunnen er veranderingen zijn opgetreden in o.a. gezichtsvermogen of ☐ *Ja* ☐ *Nee*
handdominantie nadat u de eerste keer het screeningsformulier heeft
ingevuld?

Ik ben naar tevredenheid over het onderzoek geïnformeerd. Ik heb de schriftelijke informatie goed gelezen. Ik ben in de gelegenheid gesteld om vragen over het onderzoek te stellen. Mijn vragen zijn naar tevredenheid beantwoord. Ik heb goed over deelname aan het onderzoek kunnen nadenken. Ik heb het recht mijn toestemming op ieder moment weer in te trekken zonder dat ik daarvoor een reden behoef op te geven.
Ik stem toe met deelname aan het onderzoek:
Naam: Gewicht (Kg):
Geboortedatum(d/M/yyyy):   Datum (d/M/yyyy):   *12/12/2012*

Handtekening:

In te vullen door onderzoeker

Naam: Projectnummer:

Ondergetekende verklaart dat de hierboven genoemde persoon zowel schriftelijk als mondeling over het bovenvermelde onderzoek geïnformeerd is. Hij/zij verklaart tevens dat een voortijdige beëindiging van de deelname door bovengenoemde persoon, van geen enkele invloed zal zijn op de zorg die hem of haar toekomt.

Functie:

Handtekening: Datum:

---

* Dit formulier is bestemd voor onderzoek met personen van 18 jaar en ouder die wils bekwaam zijn.
  Bij dit soort onderzoek moet door de betrokkenen zelf toestemming worden verleend.
Versie 1.0

A.16.2 Advertisement for recruitment of healthy controls

List of abbreviations and symbols

3D-dwEPI	3D diffusion-weighted Echo Planar Imaging
CNR	Contrast-to-Noise Ratio
CSD	Constrained Spherical Deconvolution
CT	Computed Tomography
DBS	Deep Brain Stimulation
DWI	Diffusion-Weighted Imaging
FA	Fractional Anisotropy
FLASH	Fast Low Angle Shot
fMRI	functional Magnetic Resonance Imaging
FOD	Fiber Orientation Distribution
GE	Gradient Echo
GP	Globus Pallidus
GPe	external Globus Pallidus
GPi	internal Globus Pallidus
GRASE	GRadient And Spin Echo
GRE	Gradient Recalled Echo
MD	Mean Diffusivity
MIP	Minimum Intensity Projections
MNI	Montreal Neurological Institute
MPRAGE	Magnetization-Prepared Rapid Acquisition of Gradient Echo
MR	Magnetic Resonance
MRI	Magnetic Resonance Imaging
OCD	Obsessive Compulsive Disorder
ODF	Orientation Density Function
PBS	Phosphate Buffered Saline
PD	Parkinson's Disease
RN	Red Nucleus
SN	Substantia Nigra
SNc	Substantia Nigra pars compacta
SNr	Substantia Nigra pars reticulata
SNR	Signal-to-Noise Ratio
SPACE	Sampling Perfection with Application of optimized Contrasts using different flip angle Evolutions
STN	Subthalamic Nucleus
SW	Susceptibility-Weighted
SWI	Susceptibility-Weighted Imaging
T	Tesla
TE	Echo Time
TSE	Turbo Spin Echo
UPDRS	Unified Parkinson's Disease Rating Scale
Vim	Ventral intermediate nucleus
ZI	Zona Incerta
$\mathbf{v}$	eigenvector
λ	eigenvalue
χ	Magnetic susceptibility

Acknowledgements

Just like regular life itself, science thrives on group efforts where everyone contributes their unique expertise and skills. Luckily I've been in the position to receive lots of support from the people around me. My colleagues and other professionals from the field of neuro-MRI, friends, and family have all (whether they know it or not) contributed to the generation of this thesis and they all deserve a special thanks.

Om te beginnen, mijn promotoren prof. Bart ter Haar Romenij en prof. Yasin Temel. Bart, bedankt dat je initiatiefnemer bent van dit project en de basis hebt gelegd voor het te vervolgen onderzoek. Yasin, bedankt voor het vertrouwen en de kansen die je me gegeven hebt in Maastricht, voor je volhardende wetenschappelijke enthousiasme en voor alle neurowetenschappelijke en klinische expertise die je hebt toegevoegd.

I would also like to thank the other co-authors of my papers. Alard, thank you for providing the essential diffusion MRI input. Kâmil, thank you for all the scientific discussions, the support, and for the opportunities you've given me. Dimo and Valentin, thank you for your technical input, but also for your practical (last-minute) scan support. Mark, thank you for your clinical perspectives and for your commitment to the recruitment of subjects.

An essential part of the work described in this thesis was performed at the University of Minnesota in Minneapolis. Therefore I would like to thank prof. Noam Harel for the warm welcome, for the fruitful collaboration and discussions, and for the promising results that we achieved. Of course these thanks also go out to Yuval and Rémi. In addition to good science you have all made me feel very welcome. For the latter I should also send special thanks to Gosia and Michelle who engaged me in all the fun activities. Michelle, even before I arrived you already helped me feel at home in a new place. We had a good time together and you helped me make new friends very quickly, making me cherish my memories to my time in Minneapolis.

Having two offices, one in Eindhoven and one in Maastricht, also gives me the advantage of having many kind and fun roommates and other coworkers. During the past four years, we have not only shared our research, but also our personal lives. I want to thank my colleagues from Eindhoven, Jiong, Renata, Samaneh, Neda, Marcel, Josien, Roy, Erik, Behdad, Mitko, Fan, and Maxime for their listening ears. During a large part

of this project I lived in Maastricht allowing me to not only learn from my fellow PhD-students, but also to enjoy their delicious dinners, birthday cakes, house warmings, weddings, sport activities, and other social events. Special thanks go to Maartje, João, and Jasper, my 'first generation' buddies and to Gusta and Anne for being my always interested coworkers and paranymphs. Together with Özlem, Remco, Fred, Milaine, Sarah, Lianci, Paul, Beth, Mélanie, Céline, Ali, Govert, Lisa, Sandra, and Majed, you make a good team and always create a 'gezellige' working atmosphere.

Additionally I would like to thank our collaborators at the Chinese Academy of Sciences in Beijing, especially prof. Tianzi Jiang and Yu Zhang.

Een groot deel van het onderzoek beschreven in dit proefschrift is uitgevoerd met behulp van gezonde proefpersonen en parkinsonpatiënten; uiteraard komt mijn dank ook hun toe. En dat had ook niet gekund zonder de hulp van Nicole, dus ook daarvoor mijn dank.

Maar niet alleen de vakmensen hebben bijgedragen aan de totstandkoming van dit manuscript. Ook mijn lieve vrienden hebben mij met hun bewondering, vertrouwen en ontspanning gesteund bij het uitvoeren van mijn werk. Jolanda, met jou is het altijd gezellig en hoef ik even lekker niet aan werk te denken. Ook de Gouwe Ouwe, Mirte, Denise, Sanneke en Maartje, wil ik bedanken, want jullie staan natuurlijk altijd voor me klaar. En natuurlijk ook Mai, die altijd zei hoe trots ze was. Simone, ook met jou kan ik alles bespreken en even lekker ontspannen van het werk. En tenslotte natuurlijk iedereen van UB, deels voor het delen van ervaringen maar vooral gewoon voor de gezelligheid op de borrels, tijdens de lunch, en natuurlijk daarbuiten.

Naast mijn vrienden speelt ook mijn familie natuurlijk een belangrijke rol. Pap en mam, jullie hebben me altijd gestimuleerd en alle voorwaarden gecreëerd om het beste uit mezelf te halen. Bedankt dat jullie er altijd voor me zijn. En Nienke ook jij staat altijd voor me klaar en kent de perikelen van het promotietraject zelf ook.

En ten slotte lieve René, wil ik jou bedanken. Op de lange terugweg van een dag werken in Maastricht zingt Domiens jingle altijd "(met de radio) ben je al bij hem of haar", een warme herinnering aan dat ik lekker thuis mag komen bij jou. Met jouw liefde, humor, bescheidenheid, aansporing en ontnuchterende kalmte heb je mij de steun gegeven om dit proefschrift te kunnen schrijven, waardoor ik nu – net als jij – kan zeggen: het is volbracht!

Curriculum vitae

Birgit Plantinga was born on September 7th, 1986 in Eindhoven. After completing secondary school (Eckart College, Eindhoven) with great appreciation, she started studying Biomedical Engineering at the Eindhoven University of Technology. She combined her studies with the organization of student activities for study association Protagoras and with teaching mathematics and physics at a secondary school (Luzac College, 's Hertogenbosch). During the master of Biomedical Engineering Birgit focused on medical image analysis techniques. During an externship at University College London she worked on the development of a computer aided diagnosis algorithm for the detection of prostate cancer. In 2012 she graduated with great appreciation on the automatic detection of coronary vessels from X-ray cardiograms in collaboration with the company Pie Medical Imaging located in Maastricht.

After moving to Maastricht, Birgit continued her scientific career as a PhD candidate in the department of Medical Image Analysis at the Eindhoven University of Technology supervised by Prof. B.M. ter Haar Romeny in close collaboration with the department of Neuroscience at the Maastricht University, under supervision of Prof. Y. Temel. During four years of research, of which she spent six fruitful months at the Center for Magnetic Resonance Research of the University of Minnesota, she focused on 7 T MRI in patients with Parkinson's disease. This lead to various conference contributions including oral presentations at the International Conference on Deep Brain Stimulation (Düsseldorf, 2016) and the European Society for Stereotactic and Functional Neurosurgery Meeting (Maastricht, 2014). More importantly, this resulted in a number of publications, which form the basis of this thesis.

List of publications

First author

1. **B.R. Plantinga**, Y. Temel, Y. Duchin, K. Uludağ, R. Patriat, A. Roebroeck, M. Kuijf, A. Jahanshahi, B.M. ter Haar Romenij, J. Vitek, N. Harel. *Patient-specific parcellation of the human subthalamic nucleus in Parkinson's Disease with ultra-high field MR imaging.* NeuroImage (2016) In press. doi: 10.1016/j.neuroimage.2016.09.023

2. **B.R. Plantinga**, A. Roebroeck, V.G. Kemper, K. Uludağ, M. Melse, J. Mai, M.L. Kuijf, A. Herrler, A. Jahanshahi, B.M. ter Haar Romeny, Y. Temel. *Ultra-high field MRI post mortem structural connectivity of the human subthalamic nucleus, substantia nigra, and globus pallidus.* Frontiers in Neuroanatomy (2016).
Vol. 10, pp 1-10. doi: 10.3389/fnana.2016.00066

3. **B.R. Plantinga**, Y. Temel, A. Roebroeck, K. Uludağ, D. Ivanov, M.L. Kuijf, B.M. ter Haar Romenij. *Ultra-high field magnetic resonance imaging of the basal ganglia and related structures.* Frontiers in Human Neuroscience (2014).
Vol. 8, nr. 876, pp 1-22. doi: 10.3389/fnhum.2014.00876

4. **B.R. Plantinga**, Y. Temel, D. Ivanov, E. Altunsoy, B.M. ter Haar Romeny, M. Kuijf, K. Uludağ. *Quantitative 7T MRI of the basal ganglia in Parkinson's disease: alterations in T1, T2* and mean diffusivity.* Under review.

Co-authorships

5. A.Y. Smeets, A.A. Duits, **B.R. Plantinga**, A.F Leentjens, M. Oosterloo, V. Visser-Vandewalle, Y. Temel, L. Ackermans. *Deep Brain Stimulation of the internal globus pallidus in refractory Tourette Syndrome.* Clinical Neurology and Neurosurgery (2016).
Vol. 142, pp 54-59. doi: 10.1016/j.clineuro.2016.01.020

6.   A. Fuster. T. Dela Haije, A. Tristán-Vega, **B.R. Plantinga**, C.-F. Westin, L.M.J Florack. *Adjugate diffusion tensors for geodesic tractography in white matter.* Journal of Mathematical Imaging and Vision (2015).
      Vol. 6, nr. 13, pp 1-14. doi: 10.1007/s10851-015-0586-8

7.   J.V. Smit, **B.R. Plantinga**, M. Janssen, L. Ackermans, M. Oosterloo, A. Duits, A.F.G. Leentjens, V. van Kranen-Mastenbroek, J.J. van Overbeeke, Y. Temel, *Diepe hersenstimulatie: de stand van zaken.* Tijdschrift voor Neurologie & Neurochirurgie (2014).
      Vol. 115, nr. 1, pp 20-25b.

8.   Y. Temel, **B.R. Plantinga**, M. Kuijf. *Anatomie van de gebruikte targets bij diepe hersenstimulatie.* In Y. Temel, A.F.G. Leentjens, R.M.A de Bie (eds.), *Handboek diepe hersenstimulatie bij neurologische en psychiatrische aandoeningen* (2016). In press.
      pp 11-17. doi: 10.1007/978-90-368-0959-7

9.   A.E.P. Mulders, **B.R. Plantinga**, K. Schruers, A. Duits, M.L.F. Janssen, L. Ackermans, A.F.G. Leentjens, A. Jahanshahi Y. Temel. *Deep brain stimulation of the subthalamic nucleus in obsessive-compulsive disorder: neuroanatomical and pathophysiological considerations.* Under review.

10.   A.E.P. Mulders, A.F.G. Leentjens, **B.R. Plantinga**, K. Schruers, A. Duits, L. Ackermans, and Y. Temel. *Choreatic side effects of deep brain stimulation of the subthalamic nucleus for treatment-resistant obsessive-compulsive disorder: a case report.* Submitted.

Conference contributions

1.   **B.R. Plantinga**, Y. Temel, Y. Duchin, K. Uludağ, A. Roebroeck, M. Kuijf, A. Jahanshahi, B.M. ter Haar Romenij, J. Vitek, N. Harel. *Patient-Specific Parcellation of the Subthalamic Nucleus in Parkinson's Disease.* 22nd Annual Meeting of the Organization for Human Brain Mapping OHBM. 26-30 June 2016, Geneva, Switzerland.

2.   **B.R. Plantinga**, Y. Temel, Y. Duchin, K. Uludağ, A. Roebroeck, M. Kuijf, A. Jahanshahi, B.M. ter Haar Romenij, N. Harel. *Individualized identification of the motor part of the sub-thalamic nucleus in Parkinson's disease.* International Conference on Deep Brain Stimulation, 15-16 March 2016, Düsseldorf, Germany.

3. **B.R. Plantinga**, A. Roebroeck, M. Bastiani, V.G. Kemper, K. Uludağ, Y. Temel, B.M. ter Haar Romenij. *High resolution imaging of the human subthalamic nucleus network*. Second Belgian Neuroinformatics Congress, 4 December 2015, Leuven, Belgium.
doi: 10.3389/conf.fninf.2015.19.00012

4. **B.R. Plantinga**, K. Uludağ, A. Roebroeck, M. Bastiani, V. Kemper, B.M. ter Haar Romenij, Y. Temel. *High resolution imaging of the human subthalamic nucleus network*. Brain states. 11-13 November 2015, Cologne, Germany.

5. **B.R. Plantinga**, A. Roebroeck, K. Uludağ, D. Ivanov, M. Melse, M. Mentink, M. Kuijf, B.M. ter Haar Romenij, Y. Temel. *High resolution in vivo connectivity mapping of the subthalamic nucleus with ultra-high field MRI.* 21st Annual Meeting of the Organization for Human Brain Mapping OHBM. 14-18 June 2015, Honolulu, USA.

6. **B.R. Plantinga**, A. Roebroeck, M. Bastiani, V.G. Kemper, M. Melse, K. Uludağ, M. Kuijf, A. Jahanshahi, B.M. ter Haar Romenij, Y. Temel. *Structural connectivity mapping and parcellation of the human subthalamic nucleus using ultra-high field diffusion MRI.* 23rd Annual Meeting & Exhibition of the International Society for Magnetic Resonance Imaging ISMRM. 30 May-5 June 2015, Toronto, Canada.

7. **B.R. Plantinga**, A. Roebroeck. M. Bastiani, V.G. Kemper, M. Melse, K. Uludağ, M. Kuijf, A. Jahanshahi, B.M. ter Haar Romenij, Y. Temel. *Structural connectivity mapping and parcellation of the human subthalamic nucleus using ultra-high field diffusion MRI.* ISMRM Benelux Chapter Meeting. 16 January 2015, Gent, Belgium.

8. **B.R. Plantinga**, A. Roebroeck, M. Bastiani, V.G. Kemper, M. Kuijf, K. Uludağ, B.M. ter Haar Romenij, Y. Temel. *Ultra-high resolution ex vivo connectivity and parcellation of the human subthalamic nucleus.* XXIst Congress of the European Society for Stereotactic and Functional Neurosurgery ESSFN. 18 September 2014, Maastricht, Netherlands.

9.   **B.R. Plantinga**, A. Roebroeck, D. Ivanov, K. Uludağ, M. Kuijf, B.M. ter Haar Romenij, Y. Temel. *In vivo ultra-high field tractography and subdivision of the human subthalamic nucleus to improve deep brain stimulation.* XXIst Congress of the European Society for Stereotactic and Functional Neurosurgery ESSFN. 18 September 2014, Maastricht, Netherlands.

10.   **B.R. Plantinga**, Y. Temel, A. Roebroeck, D. Ivanov, M. Kuijf, B.M. ter Haar Romenij. *Ultra-high field tractography and functional mapping of the subthalamic nucleus.* Neuroinformatics. 25-27 August 2014, Leiden, Netherlands.
       doi: 10.3389/conf.fninf.2014.18.00085.

11.   **B.R. Plantinga**, K. Uludağ, A. Herrler, A. Roebroeck, B.M. ter Haar Romenij, Y. Temel. *Ultra-high field imaging of the pallido-subthalamic network.* International Conference on Deep Brain Stimulation. 30-31 May 2013, Düsseldorf, Germany.